SENSORS & TRANSDUCERS

ISSN 1726-5479

vol. 255

1/22

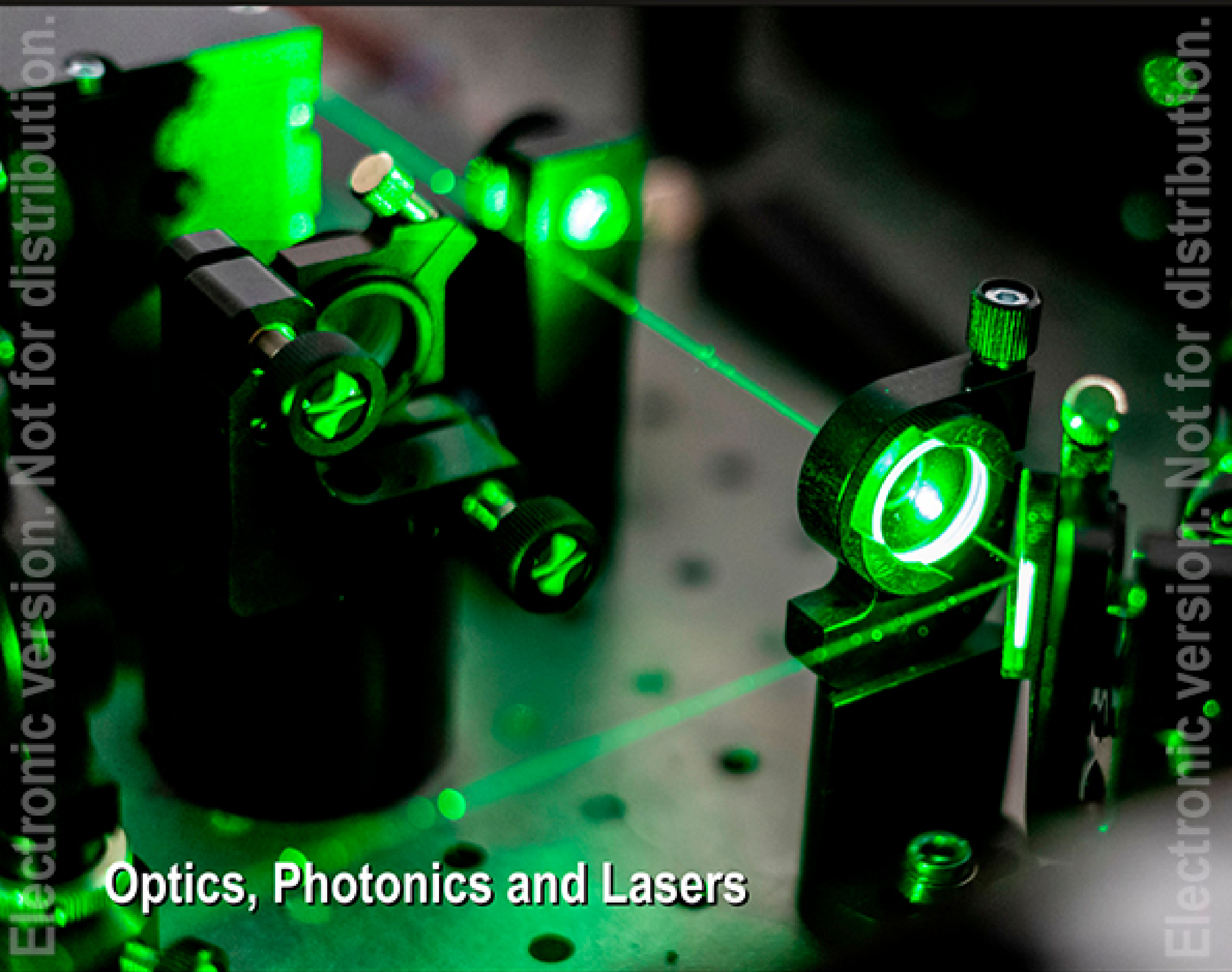

International Frequency Sensor Association Publishing

IFSA

Sensors & Transducers

International Official Open Access Journal of the International Frequency Sensor Association (IFSA) Devoted to Research and Development of Sensors and Transducers

Volume 255, Issue 1, January 2022

Editor-in-Chief
Prof., Dr. Sergey Y. YURISH

IFSA Publishing: Barcelona • Toronto

Published by International Frequency Sensor Association (IFSA) Publishing. Printed in the USA.

Sensors & Transducers

Volume 255, Issue 1
January 2022

www.sensorsportal.com

e-ISSN 1726-5479
ISSN 2306-8515

Sensors & Transducers journal is an open access, peer review international journal published monthly by International Frequency Sensor Association (IFSA).
Available in both: print and electronic (printable pdf) formats.

Sensors & Transducers Journal

Contents

Volume 255
Issue 1
January 2022

www.sensorsportal.com

ISSN 2306-8515
e-ISSN 1726-5479

Research Articles

International Frequency Sensor Association (IFSA).

Sensors & Transducers, Vol. 255, Issue 1, January 2022, pp. 1-9

Sensors & Transducers
Published by IFSA Publishing, S. L., 2022
http://www.sensorsportal.com

Polarization State Sensor Based on Polarization-Holographic Diffraction Element

Barbara KILOSANIDZE and George KAKAURIDZE
Georgian Technical University, Institute of Cybernetics,
Laboratory of Holographic Recording and Processing of Information,
5 Z. Anjaparidze Str., 1086 Tbilisi, Georgia
Tel.: + 995593306693
E-mail: b.kilosanidze@gtu.ge

Received: 4 December 2021 /Accepted: 10 January 2022 /Published: 31 January 2022

Abstract: An innovative polarization state sensor is presented for the determination of the distribution of polarization state of light reflected from the different objects. Such a sensor based on only one integral polarization-holographic diffraction element developed by us is used for real-time analysis of the polarization state of light. The simultaneous measurement of the intensities of four beams diffracted on the element and the appropriate software enable the complete polarization state of an analyzable light (the four Stokes parameters) to be obtained in real-time. The polarization state of light reflected from the object enables to obtain the physical-chemical characteristics of the object's surface. An application of the sensor in the tasks of remote sensing and in studying a stressed state in different constructions are presented. Such sensor has many advantages compared to conventional devices of polarization optics: operation in real time; a wide spectral range; they differ by compactness, universality, simplicity, light weight and comparative cheapness.

Keywords: Polarization state sensor, Diffraction and gratings, Polarization-holographic element, Polarimetry, Stokes parameters.

1. Introduction

The information capacity of the methods of determining the characteristics of the object essentially increases when together with other characteristics of light reflected from an object the polarization state is taken into account. In this case, the additional parameters of information processing are introduced (ellipticity, the azimuth, the direction of rotation, and the degree of polarization).

Information on the polarization state of light scattered or radiated by different objects plays an increasing role in remote sensing, ellipsometry, astropolarimetry, object recognition and others. Therefore, the development of simple, precision and real-time sensor for determining the polarization state and also the distribution of polarization state on the images of different objects without any scanning, taken into account also a dispersion of this distribution, is rather urgent.

The method of recording and reconstructing of the vector character of the fields of electromagnetic wave – polarization holography - was first proposed by Prof. Sh Kakichashvili in 1972 [1, 2].

One of the most promising applications of polarization holography is the creation of polarization-holographic gratings with different anisotropic-gyrotropic profile. Such gratings could be applied in various fields of science and engineering, where the analysis and transformation of light are necessary [3].

The polarization-holographic method gives the possibility to create polarization-holographic diffraction elements (PHE) which enables carrying out a complete analysis of the state and degree of polarization in real-time and working in a wide spectral range including near infra-red [3, 4]. We suggest an innovative sensor of the polarization state based on such an integral polarization-holographic element. Let us note that currently used sensors and polarimeters are complex and expensive devices and most of them contain mechanically rotating or electronically tunable optical elements [5, 6].

In this paper, the description and characteristics of the suggested polarization state sensor and the examples of its application in the tasks of remote sensing and in studying a stressed state in different constructions are presented.

2. Polarization-Holographic Diffraction Element

We suggest carrying out a complete real time analysis of the polarization state of light (also the distribution of the polarization state) by only one Integral Polarization-Holographic Diffraction Element. Such an element was created by means of polarization-holographic method, when some polarization-holographic gratings with different profile of the anisotropy and gyrotropy in the band are recorded on one and the same area of polarization-sensitive material, so that the beams diffracted on each hologram have been spatially separated [4, 7].

In [4] the general case of the recording of polarization-holographic gratings by two coherent beams of arbitrary elliptic polarization was considered. We have developed the theoretical model to describe the functioning of the sensor.

The Jones vectors [8] of the two recording beams are

$$\hat{\psi} = \begin{pmatrix} \psi_x \exp ia_x \\ \psi_y \exp ia_y \end{pmatrix} \exp i\omega t, \quad \hat{\xi} = \begin{pmatrix} \xi_x \exp ib_x \\ \xi_y \exp ib_y \end{pmatrix} \exp i(\omega t + \delta), \tag{1}$$

where $\hat{\psi}_x = \psi_x \exp ia_x$ and $\hat{\psi}_y = \psi_y \exp ia_y$, $\hat{\xi}_x = \xi_x \exp ib_x$ and $\hat{\xi}_y = \xi_y \exp ib_y$ are the x and y components of the complex amplitude of the two recording beams; ω is the frequency; and δ is the phase shift that occurs at a certain angle between the beams during recording.

We use polarization-sensitive materials for recording polarization-holographic gratings and elements on their basis. In such materials a photoanisotropy and photogyrotropy of optical parameters are induced under the action of polarized light. The side-chain polymers, the materials based on azodyes in polymer matrices and azodyes-colored liquid crystalline polymers are mostly used materials for polarization-holographic recording. The recording materials used by us are stable and due to this fact information recording on such materials is kept for a long time (some years and more) [9, 10].

The regularity of the connection of anisotropy and gyrotropy induced by polarized light with the polarization characteristics of the inducing light were obtained [11, 12]. This regularity is of universal character irrespective of the mechanism of anisotropy and gyrotropy induction. The complex coefficients of the photoinduced linear and circular birefringence appear in this regularity and functions of the scalar (isotropic) reaction $\hat{s}$ on the acting intensity of light and two vector reactions – the anisotropic reaction $\hat{v}_L$ on linearly polarized light and the gyrotropic reaction $\hat{v}_G$ on circularly polarized light are introduced to describe the photoresponse of the polarization-sensitive medium

$$\hat{n}_{1,2}^2 = \hat{n}_0^2 + \hat{s}(I_1 + I_2) \pm \sqrt{[\hat{v}_L(I_1 - I_2)]^2 + [\hat{v}_G(I^+ - I^-)]^2}, \tag{2}$$

where $\hat{n}_1$ and $\hat{n}_2$ are the complex coefficients of elliptical birefringence of the medium; $\hat{n}_0$ is the complex refractive index of the medium in the initial unirradiated state; a complex refractive index is given in the form of $\hat{n} = n - in\tau$ (n is the real refractive index and τ is the extinction coefficient); $I_1 + I_2$ is the first Stokes parameter, $I_1 - I_2$ is the second Stokes parameter, and $I^+ - I^-$ is the fourth Stokes parameter of the inducing light.

Under the action of the joint field of two recording beams (1), the corresponding complex birefringence is induced in the recording material, which is described by the Jones matrix [8]. In this case the following expressions were obtained for Jones matrix

$$M = M_0 + M_{-1} + M_{+1}, \tag{3}$$

where

$$M_0 \approx \exp(-2i\kappa d\hat{n}_0) \begin{pmatrix} 1 & 0 \\ 0 & 1 \end{pmatrix}, \tag{4}$$

$$M_{-1} \approx -\frac{i\kappa d}{2\hat{n}_o} \exp(-2i\kappa d\hat{n}_0) \exp(i\delta) \times \begin{pmatrix} (\hat{s} + \hat{v}_L)\hat{\psi}_x^* \hat{\xi}_x + (\hat{s} - \hat{v}_L)\hat{\psi}_y^* \hat{\xi}_y & (\hat{v}_L + \hat{v}_G)\hat{\psi}_x^* \hat{\xi}_y + (\hat{v}_L - \hat{v}_G)\hat{\psi}_y^* \hat{\xi}_x \\ (\hat{v}_L - \hat{v}_G)\hat{\psi}_x^* \hat{\xi}_y + (\hat{v}_L + \hat{v}_G)\hat{\psi}_y^* \hat{\xi}_x & (\hat{s} - \hat{v}_L)\hat{\psi}_x^* \hat{\xi}_x + (\hat{s} + \hat{v}_L)\hat{\psi}_y^* \hat{\xi}_y \end{pmatrix}, \tag{5}$$

$$M_{+1} \approx -\frac{i\kappa d}{2\hat{n}_o}\exp(-2i\kappa d\hat{n}_0)\exp(-i\delta) \times \begin{pmatrix} (\hat{s}+\hat{v}_L)\hat{\psi}_x\hat{\xi}_x^* + (\hat{s}-\hat{v}_L)\hat{\psi}_y\hat{\xi}_y^* & (\hat{v}_L+\hat{v}_G)\hat{\psi}_y\hat{\xi}_x^* + (\hat{v}_L-\hat{v}_G)\hat{\psi}_x\hat{\xi}_y^* \\ (\hat{v}_L-\hat{v}_G)\hat{\psi}_y\hat{\xi}_x^* + (\hat{v}_L+\hat{v}_G)\hat{\psi}_x\hat{\xi}_y^* & (\hat{s}-\hat{v}_L)\hat{\psi}_x\hat{\xi}_x^* + (\hat{s}+\hat{v}_L)\hat{\psi}_y\hat{\xi}_y^* \end{pmatrix} \quad (6)$$

Here $\kappa = 2\pi/\lambda$; λ is the wavelength, and d is the thickness of the medium. Matrix M_0 in (4) is responsible for forming the nondiffracted order, matrices M_{-1} and M_{+1} are, respectively, responsible for forming orders -1 and +1.

With (5) and (6) it is easy to obtain Jones matrices of gratings for different combinations of the polarization state of recording beams. Substituting into (5) and (6) the concrete values of the components of the Jones vectors of the recording beams and the characteristics of the recording medium, we can obtain matrices M_{-1} and M_{+1} for different type of polarization-holographic gratings using recording media with different characteristics.

Currently, we use three polarization-holographic gratings for creation the polarization-holographic element: grating recorded by orthogonal circularly polarized beams (grating *C*); grating recorded by two parallel vertically linearly polarized beams (grating L_{90}) and grating recorded by two parallel linearly polarized beams with an azimuth of linear polarization of 45^0 (grating L_{45}). At present we use +1 and -1 orders from grating C and +1 orders from gratings L_{90} and L_{45}. This configuration enables to completely circumvent the distortions of the polarization state caused by the imperfection of the recording material [3].

It follows from (5) and (6) that the Jones matrices responsible for formation diffraction orders by each grating are written in the form [4]:

$$\begin{aligned} M_{\mp1,C} &\approx A\frac{\psi_C^2}{2}\exp[\mp i(a_x-b_x)]\exp(\pm i\delta)\begin{pmatrix} 1 & \mp i \\ \mp i & -1 \end{pmatrix} \\ M_{\mp1,C} &\approx A\frac{\psi_C^2}{2}\exp[\mp i(a_x-b_x)]\exp(\pm i\delta)\begin{pmatrix} 1 & \mp i \\ \mp i & -1 \end{pmatrix} \\ M_{\mp1,90} &\approx A\frac{\psi_{90}^2}{2}\exp[\mp i(a_y-b_y)]\exp(\pm i\delta)\begin{pmatrix} 0 & 0 \\ 0 & 1 \end{pmatrix} \\ M_{\mp1,45} &\approx A\frac{\psi_{45}^2}{2}\exp[\mp i(a_x-b_x)]\exp(\pm i\delta)\begin{pmatrix} 1 & 1 \\ 1 & 1 \end{pmatrix} \end{aligned} \quad (7)$$

where $A = -\dfrac{i\kappa d\hat{v}_L}{2\hat{n}_o}\exp(-2i\kappa d\hat{n}_0)$.

Let us a beam with the Jones vector $\begin{pmatrix} E_x \exp i\varepsilon_x \\ E_y \exp i\varepsilon_y \end{pmatrix}$ incomes on the element and diffracts on them.

The Jones vectors of diffracted orders are derived from multiplication of the Jones matrices responsible for the formation of appropriate diffraction order by the Jones vector of the incoming wave. As a result, we have obtained the Jones vectors of the beams diffracted on the element and the corresponding intensities of the diffracted orders have the following form

$$\begin{aligned} I_{-1,C} &\approx \frac{1}{2}A^2\psi_C^4[E_x^2+E_y^2-2E_xE_y\sin(\varepsilon_y-\varepsilon_x)] \\ I_{+1,C} &\approx \frac{1}{2}A^2\psi_C^4[E_x^2+E_y^2+2E_xE_y\sin(\varepsilon_y-\varepsilon_x)] \\ I_{-1,L_{90,45}} &\approx A^2\psi_L^4[E_x^2+E_y^2+2E_xE_y\cos(\varepsilon_y-\varepsilon_x)] \\ I_{+1,L_{90,45}} &\approx \frac{1}{2}A^2\psi_L^4E_y^2, \end{aligned} \quad (8)$$

where $A^2 = \left(\dfrac{\kappa d}{2n_0}\right)^2$ and $\kappa = \dfrac{2\pi}{\lambda}$, λ - element recording wavelength, d- thickness of the light-sensitive layer, n_0 - refractive index of the recording material, ψ_C^2, ψ_L^2 - recording beams intensities; E_x, E_y - amplitudes and ε_x, ε_y - the phases of the incoming beam along the *x* and *y* axes, respectively.

The light beam incomes onto the polarization-holographic element, diffracts on them and the simultaneous measurement of the intensities of four diffracted beams enables all the four Stokes parameters to be determined.

We have obtained formulas for the Stokes parameters depending on the intensities of the beams diffracted on the element in each point (x, y) of the images of an object taking into account also the dispersion of the polarization state due to the angular dispersion of an element.

The relationship between the Stokes parameters and the diffraction orders intensities was obtained in the form [4]

$$\begin{aligned} S_{0,\lambda_i} &= k_{C,\lambda_i}(I_{+C}+I_{-C}) \\ S_{1,\lambda_i} &= k_{C,\lambda_i}(I_{+C}-I_{-C}) - 2k_{90,\lambda_i}I_{90} \\ S_{2,\lambda_i} &= 2k_{45,\lambda_i}I_{45} - k_{C,\lambda_i}(I_{+C}-I_{-C}) \\ S_{3,\lambda_i} &= k_{C,\lambda_i}(I_{+C}-I_{-C}) \end{aligned} \quad (9)$$

Here I_{+C} and I_{-C} are intensities of +1st and -1st orders from grating C; I_{90} and I_{45} are intensities of +1st order from gratings L_{90} and L_{45}, accordingly. Coefficients $k_{90,\lambda i}$, $k_{45,\lambda i}$, $k_{C,\lambda i}$ are connected with absorption of light in an element, the diffraction efficiency of an element, wavelength and the optoelectronic transformations by a photodetector. The values of these coefficients are determined experimentally during calibration of the sensor.

Fig. 1 shows schematic picture of diffraction on the element.

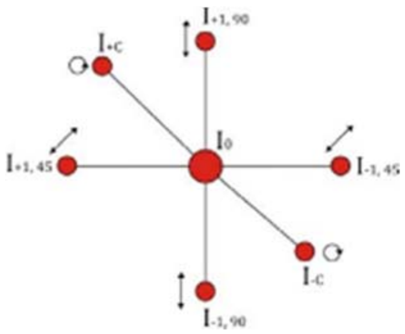

Fig. 1. Schematic picture of diffraction on the element.

We can determine all the four Stokes parameters by simultaneous measurement of the intensities of diffracted orders by using photometric scheme.

The corresponding parameters of the polarization ellipse can be determined:

the ellipticity, $\varepsilon = \dfrac{S_3}{1+\sqrt{S_1{}^2 + S_2{}^2}}$;

the azimuth of light $\alpha = \dfrac{1}{2} arctg \dfrac{S_2}{S_1}$ and

the degree of polarization $DOP = \dfrac{\sqrt{S_1^2 + S_2^2 + S_3^2}}{S_0}$.

The polarization-holographic diffraction element gives the possibility for real-time determination of the point-by-point distribution of the polarization state in the image of an object by using the appropriate software. We can take into account also the dispersion of the polarization state due to the angular dispersion of an element, which provides additional information.

To measure the intensity distribution in the diffracted orders, a photodetector matrix (such as CCD) is used, the sensitivity and dynamic range of which are selected in accordance with a specific task.

On Fig. 2 an optical scheme of the polarization state sensor is shown.

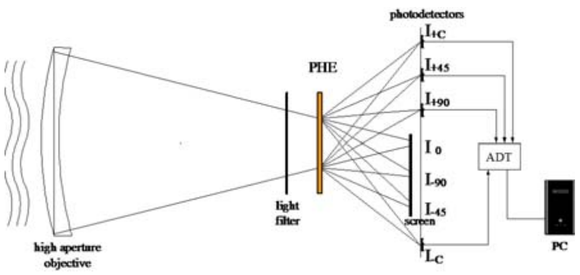

Fig. 2. Optical scheme of the polarization state sensor.

In Fig. 2, the objective forms an object image in the plane of the CCD matrix. In front of the focal plane of the objective, a polarization-holographic element is placed, which forms the diffraction orders. Each diffraction order contains an image of the object under study. Special software has been developed for point-to-point comparison of the intensities of images in diffracted beams, which enables to obtain the polarization state distribution over the object surface without any scanning.

The objective, polarization-holographic element. CCD camera and software represent *the polarization state sensor* [13].

This sensor connected to the computer with the software is a quasi-real time imaging Stokes spectropolarimeter. The sensor speed depends on the exposure of the CCD camera and on the computer processing time. For most sensor applications, the time of obtaining the polarization state distribution over an object image is units or tens of milliseconds.

Besides when narrow-band filters are used, these allow to obtain the dispersion of the distribution of the polarization state in the images of the objects for any wavelengths from a working range of the element 500 – 1600 nm.

Since the optical system consists an objective and the polarization-holographic element, there is practically no internal reflections of light, which significantly reduces the distortion of the polarization state of light under investigation and thereby reduces instrumental error.

Fig. 3 shows experimental and theoretical value variations of all Stokes parameters obtained by means of monochromatic source of linearly polarized light with change in azimuth with step of 5 degrees over the range of 0-360 degrees. These curves were obtained for light beam of a He-Ne laser (632.8 nm, power 3 mW). We see good agreement between the experimental and theoretical curves for all four Stokes parameters. Similar curves were obtained for a wavelength of 532 nm using different powers from 1 to 20 mW, as well as for infrared radiation of 1.15 μm. According to our estimate, the accuracy of the single experimental determination of the Stokes parameters is about 0.1 %. The sensitivity of the sensor depends on the sensitivity of the CCD camera, and at high exposures for very dim objects (for example, in astropolarimetry), the speed is greatly reduced and ranges from a few to tens of seconds.

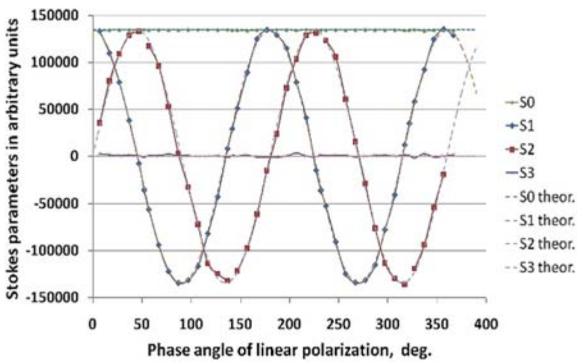

Fig. 3. Experimental and theoretical value variations of all 4 Stokes parameters.

We have obtained integral polarization-holographic elements with working spectral range from 500 nm to 1600 nm, a working aperture can be from 0.5 cm up to 5 cm in diameter and with a total diffraction efficiency of the element at wavelength of 532 nm close to 75 %, 635 nm close to 60 %, 1150 nm close to 20 %, and 1550 nm close to 8 %.

For recording the element, a polarization-sensitive material was used on the basis of azo dye Pure Mordant Yellow (PMY) modified by us and a gelatin matrix which was specially processed to increase the stability of the polarization-holographic element. The optical density of the material was approximately 2.2 at the wavelength of recording (473 nm), and the thickness of the emulsion layer was about 20 microns. Energy exposure was about 50 J/cm^2 for recording each grating.

Calibration is necessary to determine the coefficients for each element and photodetectors. As experiments have shown, it is most convenient to carry out this calibration by non-polarized quasi-monochromatic light from a point source of unpolarized light, giving a homogeneous intensity distribution in a large solid angle (a so-called "artificial star"). We used narrow-band interference filters for wavelengths of 532 nm and 635 nm with transmission band of 10 nm.

To determine the coefficients in (9), we must measure the values of intensities $I_{+1,C}$, $I_{-1,C}$, $I_{+1,90}$, $I_{+1,45}$ in the plane of localization of the diffraction orders. Than we select the order with the highest intensity, for example, $I_{+1,C}$. Coefficients k_λ are determined for the given wavelength as follows

$$k_{-1,C} = \frac{I_{+1,C}}{I_{-1,C}}, \quad k_{+1,45} = \frac{I_{+1,C}}{I_{+1,45}}, \quad k_{+1,90} = \frac{I_{+1,C}}{I_{+1,90}} \qquad (10)$$

Validation of the element was carried out by laser beams of wavelength 532 nm and 635 nm with test polarizations: left circularly polarized, linearly polarized with azimuths from -20 degrees up to +200 degrees with steps of 5 degrees and the polarization degree close to 100 %. By taking into account the obtained coefficients k_λ the photometric scheme must give us the Stokes parameters corresponding to the used polarization state when the polarization degree is close to 100 %.

The experiments showed that measurements error for intensities of the diffracted orders is 0.1 % with a single measurement and this corresponds to 0.2 % in determining the Stokes parameters. However, the software provides for the averaging of 50 single measurements, which are carried out for 0.5 s, and the relative measurement error of the intensities is about 0.002 %, and for the Stokes parameters - 0.004 %. The measurement accuracy of the degree of polarization is of about 0.15 %, and an accuracy of an azimuth of linear polarization of about 40 angular minutes.

For one of the element and photodetector matrix from camera Canon EOS 5D with CCD of 36 × 25 mm the following values of the coefficients was obtained by using the described method: for wavelength of 635 nm $k_{+1,90} = 1$, $k_{+1,45} = 1{,}346$, $k_{-1,C} = 8{,}553$, $k_{+1,C} = 7{,}916$ and for 532 nm $k_{+1,90} = 1$, $k_{+1,45} = 1{,}287$, $k_{-1,C} = 8{,}135$, $k_{+1,C} = 7{,}625$.

3. Polarization State Sensor Applications

We tested this sensor in the tasks of astropolarimetry, remote sensing, pattern recognition, for determining the stress state distribution in various constructions [14, 15].

3.1. Application in Remote Sensing

Natural light is more or less polarized while reflected from the surface of objects. The state and degree of polarization of reflected and scattered light depend on the physicochemical properties of the surface from which light is reflected, also on the angle of incident light. Information about the state of polarization can make a considerable contribution to the classification of materials and identification of objects and, together with the existing methods of recognition can significantly raise the accuracy of identification during remote sensing [16].

Current models of determining information by using the function BRDF are well enough developed, and the approximate models are used for determining distribution of the polarization state. However these approaches are difficult [17, 18].

We have developed a spectro-polarimetric method by means of the analysis of the distribution of state and degree of polarization of light reflected from a recognizable object, in which the polarization state sensor is used for a full analysis of the polarization state. The polarization state of light reflected from the object enables to obtain the physical-chemical characteristics of the object surface [19].

According to the theoretical model developed by us it is possible to determine optical characteristics of the material of the surface of an object by the values of the Stokes parameters in the images of objects using the Jones matrix of the anisotropic surface and one angle of observation and incidence [19].

Experimentally the possibility of obtaining the distribution of values of the Stokes parameters on the image of objects was shown for objects from different materials and of a different geometric form.

Software has been developed for the point-by-point definition of the Stokes parameters in the images of objects, as well as it giving the possibility to obtain average values of the Stokes parameters on the images in a solid angle close to the direction of specular reflection. As an example, Fig. 4 shows the program interfaces for objects of a round form made from copper and organic glass for the red spectral region (spectral maximum 630 nm).

Investigation of the dispersion of the Stokes parameters was carried out on the same objects. The experiments showed a significant difference both in the point-by-point distribution of the values of the Stokes parameters and in their average values, also in values of dispersion of the average Stokes parameters for green and red spectral region. The value of average dispersion $\nu = S_{i,G} - S_{i,R}$, where $S_{i,G}$ and $S_{i,R}$ are the averaged Stokes parameters for green (530 nm) and red spectral region (630 nm), respectively: for copper ν_{S1} = 0.468759, ν_{S2} = -0.041721, ν_{S3} = 0.067166; for organic glass ν_{S1} = 0.224136, ν_{S2} = 1,068955, ν_{S3} = 0.038019.

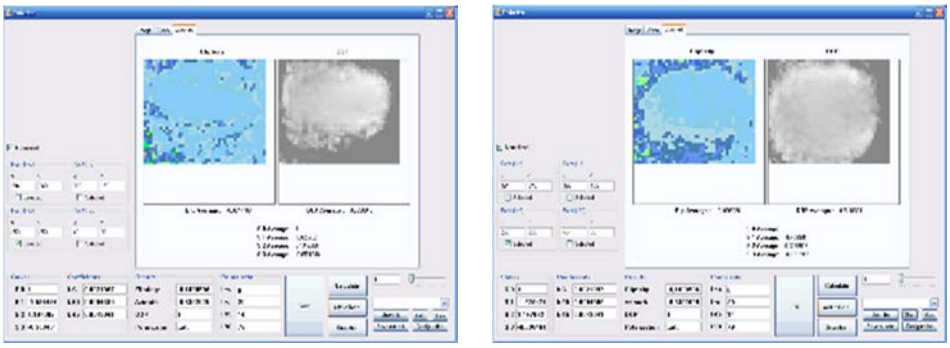

Fig. 4. Program interfaces for objects from copper (on left) and organic glass (on right) for the red spectral region and for the angle of illumination of 40^0 and angle of observation of 50^0.

This method significantly improves the recognition of various objects. The method works both in natural lighting of the object and in the case of artificial lighting.

We have developed a spectro-polarimetric method by means of the analysis of the distribution of state and degree of polarization of light reflected from a recognizable object, in which the polarization state sensor is used for a full analysis of the polarization state [19].

3.2. Stress-state Distribution in Different Constructions

The problem of quantitative determining the stress distribution in different detailes and constructions is solved by various methods: tensometry, the X-ray method, the magnetic methods, the method of acoustoelasticity, *et al.*

The method of holographic interferometry allows a picture of stress distribution to be obtained on the surface of a construction, but it is very critical to the conditions of carrying out an experiment and the interpretation of the obtained interference pattern is quite complicated. In addition, this method does not allow the results to be obtained in real time. Although the modern digital methods of holographic interferometry are more convenient and fast, they however require a comparison of a stressed state with a stress-free one, the illumination by coherent light and are also critical to the conditions of an experiment [20, 21].

In general, these methods do not work in real time, are rather time-consuming and have limitations on the materials and type of loads.

The polarization-optical method of stress analysis (a method of photoelasticity) enables the stress distribution in various constructions and details to be obtained, but it involves making the transparent models of these constructions from the materials having photoelasticity or gluing the plates from these materials on the construction under investigation, which limits the application field and reduces the measurement accuracy [22].

Despite the variety of the currently available various methods for the determination of stresses, the development of a non-destructive, technological, sensitive, convenient, all-purpose and real-time method for determining the distribution of the stress states over a wide area is extremely urgent.

It is known that mechanical stress in solids causes change in the permittivity tensor, and this change leads to the occurrence of optical anisotropy, in particular, to the occurrence of birefringence. The polarization state of the light reflected from the surface of the object or transmitted through it is the most sensitive to changes of optical properties and the determination of changes in the polarization state in the presence of stresses in solids will enable a quantitative relationship between the magnitudes of the stresses and changes in the polarization state to be established. The known stress-optic law gives the ratio between the change in the refractive index and stresses. The values of the Stokes parameters enables the value of stress to be determined at each point of the object surface. The theoretical model is presented in [23].

We have developed a real time polarimetric method for stress measurement by means of the analysis of the distribution of the state and degree of polarization of light reflected from a stressed object by use the polarization state sensor [24]. We have developed and created an appropriate laboratory model of the set-up which consists the unit for creating the dosated stresses in samples of various materials and the optical scheme based on the polarization state sensor.

There was the possibility of creating the uniaxial stresses in the sample from 0 to 125 MPa in increments of 12.5 MPa. A device with a controlled force was constructed on the basis of hydraulic jacks to create the uniaxial and biaxial dosated stresses in sample No. 5. The maximum stress in the sample were 4.9×10^8 N/m^2 in the vertical direction and 2.94×10^8 N/m^2 in the horizontal direction. In this device the possibility exists for the installation of the samples of different sizes: from 5×4 cm to 15×12 cm.

Light from the illuminator is incident on an object and reflected from it. As an illuminator, projectors based on halogen or xenon lamps, and also laser sources with wavelengths of 635 nm and 532 nm can be used. In the case of using white light, narrowband interference filters are installed in the scheme before the polarization holographic element to eliminate the influence of the angular dispersion of the element, distorting the images in the diffracted orders. The object was illuminated at an angle close to 45 degrees to the normal to the sample surface, and the observation was carried out in the direction of maximum indicatrix of the scattering from the object surface at an angle close to –45 degrees. By means of the specially developed software, we get an image of distribution of the polarization state and also of the stressed state of a source material.

We investigated samples of 8 × 10 × 5 cm of the following materials: untempered steel 45, grade of concrete 400, red brick, technical aluminum, duralumin D16. The surface of the samples was ground by fine sandpaper and surface roughness was almost the same for all samples. The samples were illuminated sequentially by a laser beam with a wavelength of 635 nm and 532 nm, with the right circularly and linearly polarized radiation with an azimuth of 0 degree. For experimental determination of the stress state distribution for different dosated load for a given material of the object we have determined the distribution of the values of the Stokes parameters and the corresponding values of the degree of polarization and ellipticity of the polarization ellipse of the light reflected from the sample surface.

As an example, Fig. 5 shows the dependence of the degree of polarization on the stress in three samples: steel 45, concrete grade 400 and aluminum in case of illuminating the sample with a laser beam of 635 nm.

As follows from these curves there is a significant difference for the samples from different materials. So, for a sample of steel the degree of polarization increases monotonically with increasing the stress (there is a small plateau due to the start of yielding flow of the material at 50 - 80 MPa), and then the rise is observed again. In case of concrete the increase in the degree of polarization is observed under certain loads (at 20-50 MPa). With the further increase of stresses, the degree of polarization increases and then the recession of the values of the degree of polarization begins at 90-110 MPa, which obviously is due to the formation of microcracks. For aluminum, there is almost a constant value of the degree of polarization for all loads, due to its high plasticity.

By means of the laboratory model, we have investigated the possibility of determining the distribution of stressed state on the surface of the object, including diffuse reflecting objects. As an example, Fig. 6 demonstrates screenshots showing the change in the polarization state of light reflected from the object surface (steel ingot by the size of 7×5×5 cm) with application of load perpendicular to the length.

The screenshots show a picture without a load, and with a load of 20 kN and 40 kN. On the right of each screenshots, the color scales are shown in which each color corresponds to the definite load values. The figures show that the picture changes significantly when the load is applied.

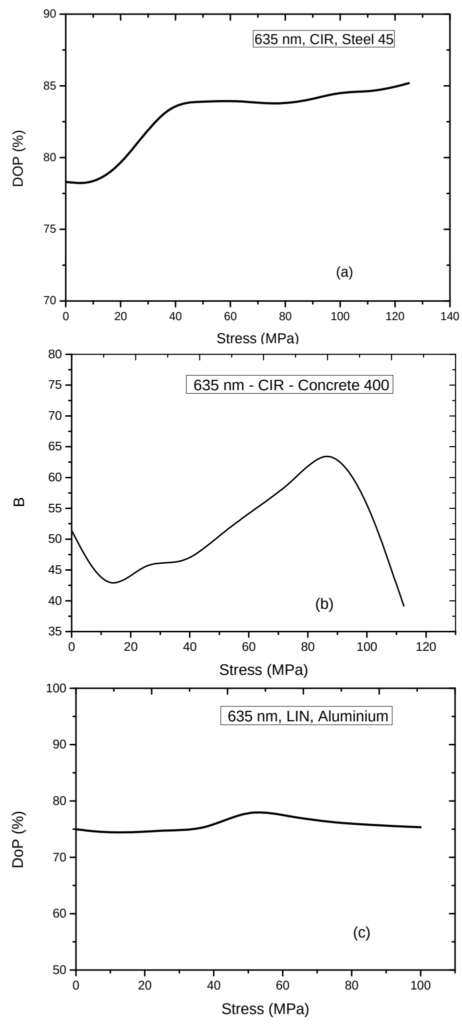

Fig. 5. The dependence of the degree of polarization on the stress in three samples of: (a) steel 45; (b) concrete grade 400; (c) aluminum. Illuminating by laser beam of 635 nm.

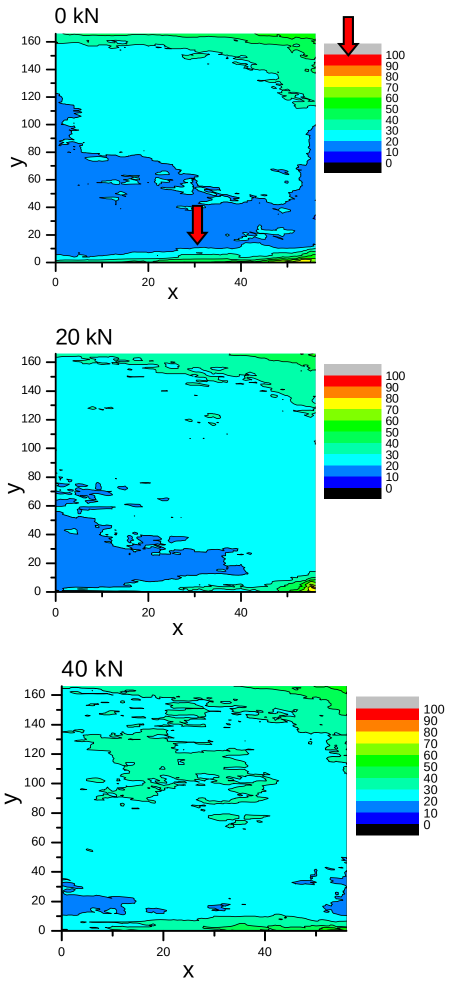

Fig. 6. The distribution of the stress states in the sample of steel 45 in case of different loads: 0, 20, 40 kN.

This approach seems very promising because, unlike the existing methods, it does not require the creation of transparent models of objects or sticking plates from transparent photoelastic materials on an object and also it does not require double-exposure holographic registration of an object and it is extremely sensitive. The method is nondestructive, i.e. there is no need to drill holes or openings in the product to determine the residual stresses. This method will enable the monitoring and diagnosis of already existing constructions to be carried out.

4. Conclusions

The real time complete analysis of polarization state of light is suggested by means of polarization state sensor based on the polarization-holographic elements. Such a polarization state sensor has many advantages compared to conventional devices of polarization optics: it enables to carry out the polarization analysis and transformation of light in real time; operate in a wide spectral range and do not require making mechanical moving and rotations or tuning of electronic units in working process. It differ by compactness, universality, simplicity, light weight, high speed and comparative cheapness.

Besides, the use of a polarization state sensor allows the distortion of the polarization state to be eliminated which inevitably appears when using sequentially several polarization-holographic gratings, and also in polarimeters of other types.

The polarization state sensor can also be applied to machine vision, for example, in autonomous cars and drones.

Acknowledgements

Authors gratefully acknowledge the Shota Rustaveli National Science Foundation of Georgia support by the grant № AR-19-1154.

References

[1]. Sh. Kakichashvili, On polarization recording of holograms, *Optics and Spectroscopy,* Vol. 33, Issue 2, 1972, pp. 324-327 (in Russian).

[2]. Sh. Kakichashvili, Polarization holography, *Nauka, Leningrad,* 1989 (in Russian).

[3]. B. Kilosanidze, G. Kakauridze, Polarization-holographic gratings for analysis and transformations of light: 1. The analysis of completely polarized light, *Applied Optics*, Vol. 46, 2007, pp. 1040-1049.

[4]. G. Kakauridze, B. Kilosanidze, Polarization-holographic diffraction element-based real-time Imaging Stokes spectropolarimetry, in *Proceedings SPIE of the Symposium Photonics West,* San Francisco, USA, Vol. 7957, 22-28 January 2011, pp. 22-28.

[5]. L. Kaiser, E. Frins, B. Hils, L. Beresnev, W. Dultz, H. Schmitzer, Polarization analyzer for all the states of polarization of light using a structured polarizer, *Journal of the Optical Society of America A,* Vol. 30, 2013, pp.1256-1260.

[6]. I. Moreno, J. A. Davis, K. Badham, *et al.,* Vector Beam Polarization State Spectrum Analyzer, *Scientific Reports*, Vol. 7, Issue 1, 2017, 2216.

[7]. B. Kilosanidze, G. Kakauridze, Polarization-holographic diffraction element for complete analysis of light, in *Proceedings SPIE of the Optics + Optoelectronics Symposium,* Prague, Czech Republic, Vol. 7358, 20-22 April 2009, pp. 7358A.

[8]. Jones R. C., A new calculus for the treatment of optical systems, *Journal of the Optical Society of America,* Vol. 31, 1941, pp. 488-493.

[9]. Sh. Kakichashvili, B. Kilosanidze, V. Shaverdova, Anisotropy and gyrotropy of dye mordant pure-yellow Induced by linear polarized light, *Optics and Spectroscopy*, Vol. 68, 1990, pp. 1309-1312 (in Russian).

[10]. I. Chaganava, G. Kakauridze. B. Kilosanidze, G. Datukishvili, Development of high- performance, stable and moisture-resistant polarization-sensitive materials, in *Proceedings SPIE of the Optical Engineering + Applications Symposium,* San Diego CA, USA, Vol. 8126, 21-25 Aug. 2011, pp. 1-10.

[11]. Sh. Kakichashvili, On the regularity in photoanisotropic phenomena, *Optics and Spectroscopy*, Vol. 52, 1982, pp. 317-322 (in Russian).

[12]. Sh. Kakichashvili, On the regularity in the phenomena of photoanisotropy and photogyrotropy, *Optics and Spectroscopy*, Vol. 63, 1987, pp. 911-917 (in Russian).

[13]. B. Kilosanidze, G. Kakauridze, Polarization state sensor, in *Proceedings of the 4th International Conference on Optics, Photonics and Lasers (OPAL' 2021),* Corfu, Greece, 13-15 October 2021, pp. 145-149.

[14]. G. Kakauridze, B. Kilosanidze, T. Kvernadze, G. Kurkhuli, Astropolarimetry with a Polarization-holographic Imaging Stokes Polarimeter, *Journal of Astronomical Telescopes, Instruments, and Systems JATIS*, Vol. 5, Issue 1, 2019, 015002.

[15]. B. Kilosanidze, G. Kakauridze, I. Kobulashvili, Pattern recognition system based on photoanisotropic copies, *Applied Optics*, Vol. 58, Issue 7, 2019, pp. 1778-1788.

[16]. S. R. Cloude, Polarization. Applications in remote sensing, *Oxford University Press Inc.*, New York, 2010.

[17]. J. Schott, Fundamentals of polarimetric remote sensing, *SPIE Press,* Bellingham, Washington, 2009.

[18]. J. S. Tyo, D. L. Goldstein, D. B. Chenault, J. A. Shaw, Review of passive imaging polarimetry for remote sensing applications, *Applied Optics*, Vol. 45, Issue 22, 2006, pp. 5453-5469.

[19]. B. Kilosanidze, G. Kakauridze, Determination of the characteristics of the surface of objects at optical remote sensing by the Polarization-Holographic Imaging Stokes Spectro-polarimeter, in *Proceedings of the SPIE Optical Metrology, Co-located with Laser World of Photonics,* Munich, Germany, Vol. 8082, 23-26 May 2011, pp. 8082-126.

[20]. R. Jones, C. Wykes, Holographic and Speckle Interferometry, *Cambridge University Press*, 1989.

[21]. G. Pedrini, P. Fröning, H. Fessler, H. J. Tiziani, In-line digital holographic interferometry, *Applied Optics*, Vol. 37, 1998, pp. 6262-6269.

[22]. J. Dijkstra, W. Broere, New method of full-field stress analysis and measurement using photoelasticity, *Geotechnical Testing Journal*, Vol. 33, Issue 6, 2010, pp. 6-20.

[23]. G. Kakauridze, B. Kilosanidze, T. Kvernadze, G. Kurkhuli, A new real-time polarimetric method for determining the distribution of stressed state in different constructions, *Proceedings Photonic Instrumentation Engineering II SPIE OPTO, S*an Francisco, USA, 22-28 January, Vol. 9369, 2015, pp. 9369OU1-10.

[24]. B. Kilosanidze, G. Kakauridze, T. Kvernadze, G. Kurkhuli, Sensor for real-time determining the polarization state distribution in the object images, in *SPIE Proceedings of the Symposium Optics and Photonics for Counterterrorism, Crime Fighting, and Defence XI,* Toulouse, France, Vol. 9652, 23-27 September 2015, p. 96520M1-10.

Sensors & Transducers
Published by IFSA Publishing, S. L., 2022
http://www.sensorsportal.com

3D Orientation of Single Gold Bipyramid Measured by Scattering Polarization Spectroscopy: Role of the Numerical Aperture

[1, *] Cam Nhung VU, [2] Zakarya OUZIT, [2] Clotilde LETHIEC, [2] Agnès MAITRE, [2] Laurent COOLEN, [3] Frédéric LEROUGE, [1] Michel PELLARIN [1] and Julien LAVERDANT
[1] Institut Lumière Matière, Université Claude Bernard Lyon 1, CNRS, Université de Lyon, F-69622 Villeurbanne, France
[2] Sorbonne Université, CNRS, Institut de NanoSciences de Paris, INSP, F-75005 Paris, France
[3] Univ Lyon, Ens de Lyon, CNRS, Université Lyon 1, Laboratoire de Chimie UMR 5182, F-69342, Lyon, France
[*] E-mail: nhungvu.phys@gmail.com

Received: 3 December 2021 /Accepted: 11 January 2022 /Published: 31 January 2022

Abstract: The 3D orientation of a single gold nano-bipyramid (AuBPs) on a glass substrate is successfully measured by polarimetric analysis of its scattering. The AuBPs are very attractive due to the presence of hot spots at their end tips resulting from a strong longitudinal localized surface plasmon resonance. In addition, this resonance can be modeled as a radiating dipole. To study the 3D orientation, we designed a specific spectroscopic dark-field microscope with a precise control of the collection angles of the scattering in the Fourier plane. The 3D angles are resolved by analyzing the polarization of the AuBP scattering. Simulations are used to extract the in-plane and out-of-plane angles with a very good accuracy of 3 %. In particular, the critical role of the numerical aperture collection was investigated experimentally by Fourier filtering of the scattering into the back focal plane of the objective. It reveals a physical insight into the contribution of the evanescence waves and provides a technical guideline for choosing the collection objective for polarimetric measurements.

Keywords: Localized surface plasmon, Gold bipyramids, Orientation, Polarization, Scattering.

1. Introduction

The determination of the orientation of nanoparticles at the single level is a key point for many applications in sensing [1, 2], coupling [3-5], and all interaction effects [6-10]. It comes from the fact that the optical response of a nano-object is sufficiently sensitive to its local environments, e.g. refractive index, that depends on the orientation of the particles. This dependence is especially significant in the situation of an elongated nanoparticle is in the vicinity of a substrate [38] where the inclination of the particles leads to several differences in scattering resonances since it decides how much the particle is exposed to the substrate index. Furthermore, the orientation is also a crucial parameter to optimize the coupling strength of an emitter inside plasmonic nanocavities. On these, a strong coupling may be achieved for emitters that are grafted following the direction of the local field inside the cavities [10, 11].

For these applications, the dye molecules, semiconductor nanocrystals, and plasmonic nanostructures have been widely used thanks to their excellent optical responses. Otherwise, plasmonic nanoparticles have a large scattering and absorption cross-section, and do not suffer from major drawbacks of the fluorescence emitters such as photoblinking [12, 13] or instability from biochemical environment [14, 15]. This comes from the ability to confine the field at the nanoscale of the noble metallic nanoparticles that emerges from a phenomenon which is known as localized surface plasmon resonance (LSPR) [16-19]. The LSPR effect becomes especially important for anisotropic plasmonic nanoparticles where gold bipyramids (AuBPs) stand as a promising candidate in recent years due to several desirable properties. The AuBPs have a high aspect ratio as common elongated plasmonic nanoparticles while own sharp curvature at the tip ends showing better local field confinement and enhancement [2]. Therefore, our work in this paper aims to determine 3D orientation of the AuBPs at the single particle level.

Various optical methods have been early developed such as radiation pattern or polarization analysis. Among the patterning methods, we can cite the defocused imaging [20, 21], and Fourier plane imaging [22-25] which offers the most convenient implementation. The orientation of the particles can be deduced from the projection of the radiation pattern on these planes. However, the angular resolved imaging usually demands highly sensitive detectors. In particular, the defocused imaging is also very sensitive to the alignment and aberrations of the experiment setup. Despite all of the strict requirements, these methods cannot be applied to all circumstances. For example, the orientation of quantum dots on an absorbing substrate is not resolved by the Fourier plane imaging [26]. On the other hand, the polarimetric analysis methods have shown good precision without rigorous requirements as the radiation pattern imaging methods [27-35]. One way is to split the optical response of nanoparticles into two orthogonal polarization directions to measure the optical anisotropy [30, 32]. However, the anisotropy measurement is only effective for the determination of the in-plane orientation.

In the presented work, we present a method to retrieve the 3D orientation of single nanoparticles based on resolved polarimetric scattering spectrum. The work goes further on investigating the role of the numerical aperture of the collection since the polarization states are not similar in different radiation directions. The developed method is then applied on gold bipyramid nanoparticles (AuBPs) that is an interesting model system for single-emitter light scattering. The AuBPs mainly support a strong longitudinal localized surface plasmon resonance owing to its very sharp end tips (other modes with very low scattering cross-sections can be neglected). This longitudinal resonance is easily tuned by playing with the aspect ratio of the particle [22, 23]. In terms of theoretical calculation, the longitudinal mode of the AuBPs can be modeled as a linear radiating dipole. In addition, the AuBPs allow access to out-of-plane angles without any surface treatment thanks to the geometry of the bipyramid.

2. 3D Orientation Measurement of a Single Gold Bipyramid

2.1. Theoretical Calculation of Polarization Analysis

Theoretical calculation is described in our previous work [26]. In this, the nanoparticle is modeled as a dipole radiating through an air-glass interface that is then collected by an objective. A polarizer with rotating angle α is placed on the detection pathway. The detected intensity oscillates between a maximum (I_{max}) and a minimum (I_{min}) values with the variation of the angle α, following the Malus's law:

$$\mathrm{I}(\alpha) = I_{min} + (I_{max} - I_{min})cos^2(\phi - \alpha) \qquad (1)$$

For the linear dipole (1D), the I_{max} is retrieved when the polarizer in the parallel direction to the dipole axis while for the orthogonal direction, the intensity is minimum. From the Eq. (1), the in – plane angle ϕ is directly retrieved.

It is important to note that the calculation has taken into account parameters of the local environment as well as the numerical aperture of the objective. At a fixed numerical aperture (NA) of a collection objective, the out – of – plane angle Θ is determined using the measured degree of polarization (DOP) δ, obtained as:

$$\delta_{\mathrm{NA}} = \frac{I_{max} - I_{min}}{I_{max} + I_{min}} \qquad (2)$$

2.2. Numerical Investigation of Scattering of Single Gold Bipyramid

The scattering spectrum of the AuBPs are investigated numerically by finite element methods (COMSOL, 5.2 software). The sizes of the AuBPs are 100 nm long and 30 nm in width (square base). The tips are slightly truncated with a square basis of 3 nm width. The geometry size of the AuBPs is deduced from the size distribution measured by scanning electron microscope (SEM). In the simulation, the AuBP is placed glass substrate with an angle of 15° and excited by a plane wave in normal incidence (Fig. 1). Under a plane wave excitation, the charges are mainly distributed at the two end tips of the AuBP results in a strong scattering resonance at 740 nm. Thus, this mode behaves like a linear radiating dipole. The two very weak modes at lower wavelength are respectively quadrupolar mode and transverse mode of the charge oscillation that are neglected in our measurement.

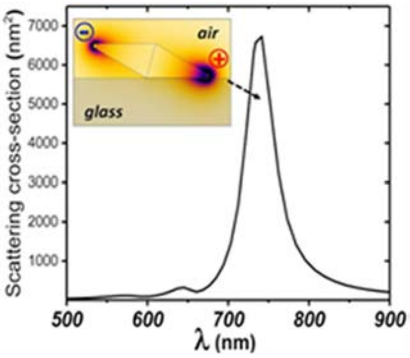

Fig. 1. Numerical simulations of the AuBP optical properties. Scattering spectrum together with, in insert, the charge distribution associated at the main resonance (740 nm).

The longitudinal surface plasmon mode of the AuBPs has dipolar nature that is spatially modified by the local environment [35], particularly in this case is the glass substrate. Therefore, we make a calculation of the scattering diagram of an AuBP in a vicinity of the glass substrate. In the calculation, the particle is modelled as a linear dipole. The far-field radiation of the dipole is collected in the semi-infinite medium of the glass (n = 1.5) by an oil matching index objective. Herein, the objective is approximately simulated as a reference sphere that converts the light into a collimated beam with a planar wave front. The emission diagram is presented as the angular distribution of the intensities radiating from the dipole $I(\theta,\varphi)$ on the Fourier plane of the objective. Due to the planar symmetry, the radiated electric field is presented in terms of p and s polarizations. The angular distribution of the radiating intensity $I(\theta,\varphi)$is express as [24]:

$$I(\theta,\varphi,\Theta,\Phi)\sim\frac{1}{cos\theta}.\left(E_s.E_s^* + E_p.E_p^*\right) \qquad (3)$$

In which, (1/cos θ) is the apodization factor which is the result of the sine condition and the energy conservation when a focused beam passing through an objective. The electric field components p and s are also functions of dipole orientation (Θ, Φ) and observation angles (θ, ϕ) (Fig. 2a), their expressions are given as:

$$E_s(\theta,\varphi) = a_1(\theta,\varphi).sin\Theta.sin(\varphi-\Phi),$$
$$E_p(\theta,\varphi) = E_p^{par}(\theta,\varphi) + E_p^{ver}(\theta,\varphi) \qquad (4)$$

with

$$E_p^{par}(\theta,\varphi) = a_2(\theta,\varphi).sin\Theta.cos(\varphi-\Phi),$$
$$E_p^{par}(\theta,\varphi) = a_3(\theta,\varphi).cos\Theta.\sin\theta$$

In which, the functions $a_1(\theta,\varphi)$, $a_2(\theta,\varphi)$, and $a_3(\theta,\varphi)$ related to the transmission coefficient of the air/glass interface. The expressions of these functions can be found in the reference [24].

The spatial distribution of intensity $I(\theta,\varphi)$on the Fourier plane of the objective is represented in terms of the wavevectors, denoted as $k_x = n.sin\theta.cos\varphi$ and $k_y = n.sin\theta.sin\varphi$. Fig. 2b shows an emission diagram on the Fourier plane $I(k_x,k_y)$ of a dipole inclined an angle of Θ = 15° to the glass substrate. As the numerical aperture of the objective $NA = n.sin\theta$, the radius of the emission diagram is limited by this parameter. In this case, the modelled objective has NA = 1.49. It is worth noting that since the dipole radiating through the air/glass interface, the solid angle corresponding to NA = 1 is the critical angle defined by refractive indices of these media. The emission diagram shows that the radiation is strongly modified by the presence of the interface toward the higher index medium (glass). Especially, the interface redistributed the radiation mainly into the evanescent regime corresponding to NA = [1, 1.49]. Besides, the influence of the out-of-plane orientation Θ = 15° is observed as the contrast of the intensities along the dipole axis.

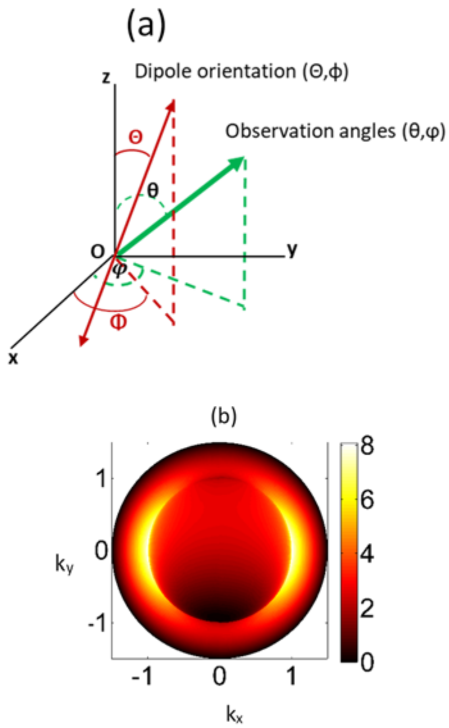

Fig. 2. (a) Schematic of the spherical coordinates defining the orientation of the dipole (Θ, Φ) and the direction of the observation (θ, ϕ); (b) Simulated emission diagram on the Fourier plane of the objective of a dipole inclined 15° to the substrate.

2.3. Experiment Set Up

Fig. 3 illustrates the experimental set up which combines dark-field imaging and Fourier filtering.

The AuBPs are deposited on a glass substrate and excited by a white lamp focused by a low numerical aperture (NA) objective and then both direct illumination and scattered light are collected by an oil objective with NA = 1.49. A beam blocker is placed at the Fourier-plane position (F'.P') to effectively block the overwhelming illumination and retain only the scattering. At the same time, a diaphragm is also set at this position to control the scattering collection NA. It is worth mentioning that the primary Fourier plane of the oil objective is usually inside or very near the objective pupil. Therefore, a conjugated lens system is used to displace the Fourier plane to a convenient position for collection manipulation. The polarization analysis of the scattered light is then conducted by combining a rotating half-wave plate (λ/2) and a fixed polarizer (P).

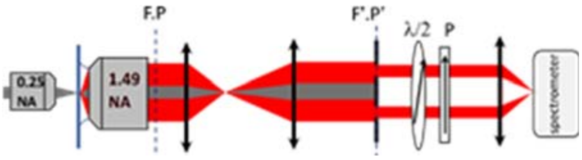

Fig. 3. Schematic of the experimental set up. F.P: the primary Fourier plane, F'.P': the image of the Fourier plane, λ/2: the rotating half-wave plate, and P: the fixed polarizer.

3. Results and Discussion

3.1. Dark-field Imaging

Fig. 4a shows a dark-field image of the AuBPs deposited on the glass substrate that was measured by the experiment setup in Fig. 3.

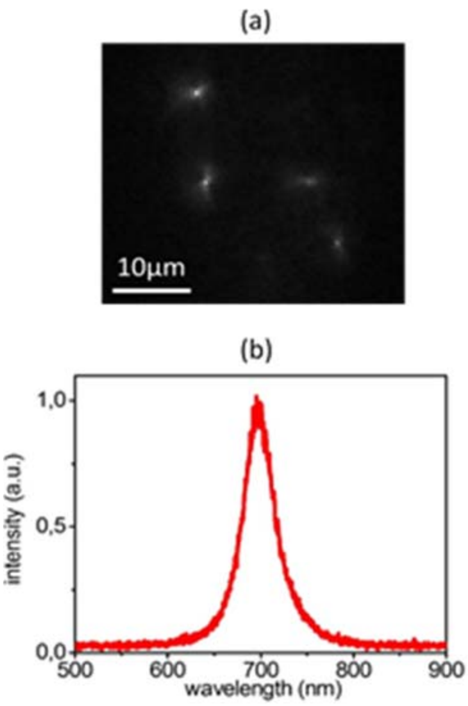

Fig. 4. (a) Dark-field image of the AuBPs deposited on the glass substrate; (b) Scattering spectrum of a single selected AuBP.

The bright spots come from the scattering of the nanoparticles while the dark background proves that the overwhelming illumination was sufficiently filtered out. Especially, the AuBPs are very well separated from each other allowing to measure scattering at the single level.

A scattering spectrum of a selected AuBP is presented in Fig. 4b where the resonance wavelength is located around 700 nm associated with the longitudinal mode. Besides, the width of the spectrum is narrow, around 50 nm, which is usually an optical response achieved from a single nano-object at the ambition condition.

3.2. 3D Orientation of the AuBPs

The polarimetric measurements are performed on the high quality AuBPs with average length of 100 nm and aspect ratio around 3.3 supporting a well – defined longitudinal resonance between 650 - 750 nm. The synthesis protocol can be found in [2]. Fig. 5 plots the obtained results of orientation measurement.

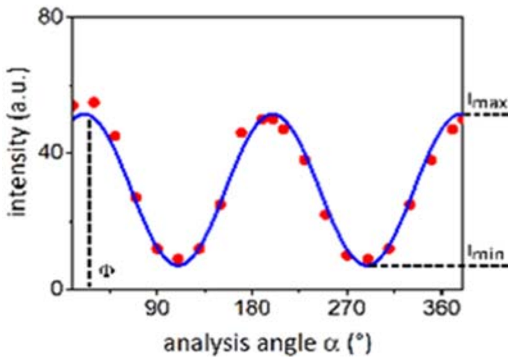

Fig. 5. Detected intensity (red dots) as a function of analysis angle α fit with the Eq. (1) (blue curve).

The evolution of the intensity as a function of the analysis angle α follows very well the Eq. (1). From the fit, three parameters are extracted: the in-plane angle Φ, the maximum, and the minimum intensities (I_{max} and I_{min}). In which, the in-plane angle is defined as analysis angle at the first maximum value of the detected intensity. We find for this AuBP, an in-plane angle Φ = 30° and a DOP δ = 0.72 with 3 % of precision. From the Eq. (2), we deduce out-of-plane angle Θ = 75°.

The degree of polarization and deduced out-of-plane angle measurement are then repeated for 30 other AuBPs (Fig. 6). We found that the AuBPs possess distributed out-of-plane angles between 60° and 90°, in which the 70-80° orientations are dominant. This distribution is consistent with the shape and the size of the AuBPs deduced from the electronic microscope measurement. There are considerable numbers of AuBPs paralleled with the substrate that might be induced from ligands surrounding the particle.

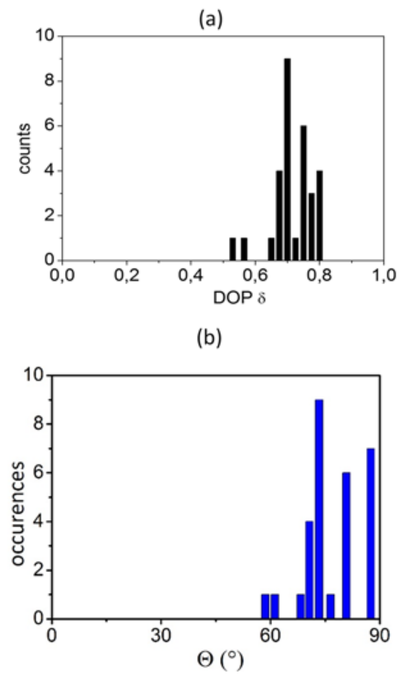

Fig. 6. Histogram of (a) degree of polarization and (b) out-of-plane orientation of 30 AuBPs measured by polarization analysis.

3.3. Role of Collection Numerical Aperture

The simulation indicates that the strong longitudinal surface plasmon resonance mode of the AuBPs behaves like a linear radiating dipole. When they are near an air/glass interface, the scattering is mainly radiated in the forbidden region above the critical angle [39]. Fig. 7 simulates the 3D radiation pattern of a dipole placed in air and near a glass substrate that is strongly redistributed toward the higher index medium.

The Fourier plane is the projection of the radiation pattern where each point on the Fourier plane corresponds to one direction of the radiation. Herein, the polarization states of different radiation directions have been presented (blue arrows). It is clear that the polarization states are not homogeneous on the entire Fourier plane. They become more complicated with the increase of numerical aperture, especially near the critical region around NA = 1. In other words, the polarization states are also strongly redistributed. Thus, in terms of the experiment, the collected NA of the objective plays an important role on the orientation measurements. In order to illustrate this dependence, we performed the polarization measurements with angular filtering. The results are displayed in Fig. 8.

Fig. 8 presents the DOP as a function of NA which is artificial changed from 0.45 – 1.49 by Fourier filtering (Fig. 3). We see that at low NA, δ nearly reaches unity but when the diaphragm is larger, it drops by 30 %, and more significantly around NA = 1. When the NA increases, the scattering is collected into different directions which possess specific polarization angles result in the decrease of the DOP. It is worth noting that the detected intensities also strongly depend on the NA collection, therefore, the choice of an optimal objective is a compromise between a fast variation of the δ(Θ) and an effective collection efficiency.

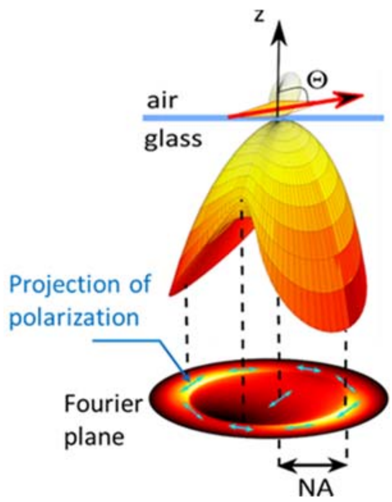

Fig. 7. Simulation of the 3D radiation pattern and the Fourier plane image of a dipole near air/glass interface. The projection of polarizations on the Fourier plane is showed as blue arrows.

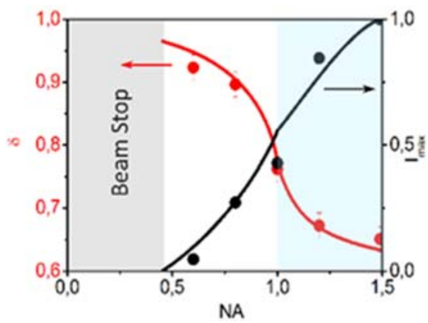

Fig. 8. DOP (red) and I_{max} (black) as functions of collection NA. Dots: experimental values. Curves: simulation.

3.4. Microscope Objective for the Polarimetric Measurement

As the DOP is strongly influenced by the collected NA, the choice of the objective for the polarimetric measurements is crucial. Fig. 9 shows the evolution of the degree of polarization (DOP) δ as the function of the out – of – plane orientation Θ with different collection: NA = 1.15 and NA = 1.49 represent for oil objectives, while NA = 0.5 and NA = 0.9 stand for air objectives.

The theoretical calculation on Fig. 9a has taken into account the experimental parameters with the presence of the beam stop 0.45NA. There is a minor difference compared to the case of collection in a full solid angle (Fig. 9b) because some polarization directions below the solid angle NAc =0.45 are cut – off by the beam stop. In the grey zones, the δ is nearly constant with collection in the large NA while its variation is bigger in the case of collection in the small NA. In the opposite, when the dipole is nearly in the plane of the substrate (Θ = 70 – 90°), it is difficult to measure variations of δ for objectives with small NA.

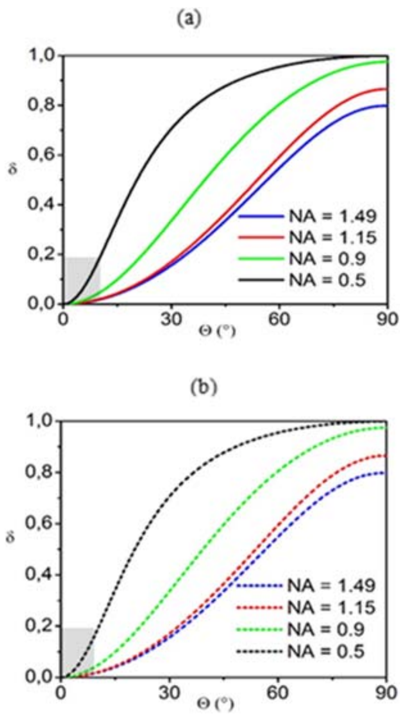

Fig. 9. Theoretical calculations of the DOP as a function of the dipole orientation Θ for two configurations of collection: (a) with the beam stop limiting NA = 0.45, and (b) for a full collection. Four different objective numerical apertures are evaluated for each configuration. The grey zones correspond to dipoles which are oriented nearly vertical (Θ = 0 – 10°).

4. Conclusions

In conclusion, we showed that the complete orientation of the AuBPs has been successfully resolved by the scattering polarimetry spectroscopy. Most of the particles exhibited the out-of-plane orientation on the substrate which is consistent with their geometry. The crucial role of the collection numerical aperture has been addressed, both experimentally and theoretically. We also show that depending on the orientation, the choice of the microscope objective NA is crucial. Our original method to obtain the direct dependence of the polarization on the objective NA may be applied for more complex systems with different radiation pattern.

Acknowledgements

We acknowledge the French Région Auvergne-Rhône-Alpes (SCUSI no 1700936601) that supported this work and the USTH French consortium.

References

[1]. T. Shegai, P. Johansson, C. Langhammer, M. Käll, Directional Scattering and Hydrogen Sensing by Bimetallic Pd–Au Nanoantennas, *Nano Letters*, Vol. 12, Issue 5, 2012, pp. 2464-2469.
[2]. J. Rye, C. Bonnet, F. Lerouge, M. Pellarin, J. Lermé, S. Parola, E. Cottancin, Single gold bipyramids on a silanized substrate as robust plasmonic sensors for liquid environments, *Nanoscale*, Vol. 10, Issue 34, 2018, pp. 16094-16101.
[3]. C. Tabor, D. Van Haute, M. El-Sayed, Effect of Orientation on Plasmonic Coupling between Gold Nanorods, *ACS Nano*, Vol. 3, Issue 11, 2009, pp. 3670-3678.
[4]. S. Kühn, U. Håkanson, L. Rogobete, V. Sandoghdar, Enhancement of Single-Molecule Fluorescence Using a Gold Nanoparticle as an Optical Nanoantenna, *Physical Review Letters*, Vol. 97, Issue 1, 2006.
[5]. P. Anger, P. Bharadwaj, L. Novotny, Enhancement and Quenching of Single-Molecule Fluorescence, *Physical Review Letters*, Vol. 96, Issue 11, 2006.
[6]. R. Chikkaraddy, B. de Nijs, F. Benz, S. Barrow, O. Scherman, E. Rosta, A. Demetriadou, P. Fox, O. Hess, J. Baumberg, Single-molecule strong coupling at room temperature in plasmonic nanocavities, *Nature*, Vol. 535, Issue 7610, 2016, pp. 127-130.
[7]. G. Akselrod, C. Argyropoulos, T. Hoang, C. Ciracì, C. Fang, J. Huang, D. Smith, M. Mikkelsen, Probing the mechanisms of large Purcell enhancement in plasmonic nanoantennas, *Nature Photonics*, Vol. 8, Issue 11, 2014, pp. 835-840.
[8]. J. Baumberg, J. Aizpurua, M. Mikkelsen, D. Smith, Extreme nanophotonics from ultrathin metallic gaps, *Nature Materials*, Vol. 18, Issue 7, 2019, pp. 668-678.
[9]. T. Hoang, G. Akselrod, C. Argyropoulos, J. Huang, D. Smith, M. Mikkelsen, Ultrafast spontaneous emission source using plasmonic nanoantennas, *Nature Communications*, Vol. 6, Issue 1, 2015.
[10]. T. Hoang, G. Akselrod, M. Mikkelsen, Ultrafast Room-Temperature Single Photon Emission from Quantum Dots Coupled to Plasmonic Nanocavities, *Nano Letters*, Vol. 16, Issue 1, 2015, pp. 270-275.
[11]. A. Dhawan, C. Belacel, J. Esparza-Villa, M. Nasilowski, Z. Wang, C. Schwob, J. Hugonin, L. Coolen, B. Dubertret, P. Senellart, A. Maître, Extreme multiexciton emission from deterministically assembled single-emitter subwavelength plasmonic patch antennas, *Light: Science & Applications*, Vol. 9, Issue 1, 2020.
[12]. F. Hu, Z. Cao, C. Zhang, X. Wang, M. Xiao, Defect-Induced Photoluminescence Blinking of Single Epitaxial InGaAs Quantum Dots, *Scientific Reports*, Vol. 5, Issue 1, 2015.
[13]. E. Riley, C. Hess, P. Reid, Photoluminescence Intermittency from Single Quantum Dots to Organic Molecules: Emerging Themes, *International Journal of Molecular Sciences*, Vol. 13, Issue 12, 2012, pp. 12487-12518.
[14]. C. Eggeling, J. Widengren, R. Rigler, C. Seidel, Photobleaching of Fluorescent Dyes under Conditions Used for Single-Molecule Detection: Evidence of Two-Step Photolysis, *Analytical Chemistry*, Vol. 70, Issue 13, 1998, pp. 2651-2659.
[15]. C. Eggeling, J. Widengren, R. Rigler, C. Seidel, Photobleaching of Fluorescent Dyes under Conditions Used for Single-Molecule Detection: Evidence of

Two-Step Photolysis, *Analytical Chemistry*, Vol. 70, Issue 13, 1998, pp. 2651-2659.

[16]. K. Mayer, J. Hafner, Localized Surface Plasmon Resonance Sensors, *Chemical Reviews*, Vol. 111, Issue 6, 2011, pp. 3828-3857.

[17]. H. Jeon, P. Tsalu, J. Ha, Shape Effect on the Refractive Index Sensitivity at Localized Surface Plasmon Resonance Inflection Points of Single Gold Nanocubes with Vertices, *Scientific Reports*, Vol. 9, Issue 1, 2019.

[18]. P. Zijlstra, P. Paulo, M. Orrit, Optical detection of single non-absorbing molecules using the surface plasmon resonance of a gold nanorod, *Nature Nanotechnology*, Vol. 7, Issue 6, 2012, pp. 379-382.

[19]. W. Shang, F. Xiao, W. Zhu, L. Han, T. Mei, J. Zhao, Characterizing localized surface plasmon resonances using focused radially polarized beam, *Applied Optics*, Vol. 58, Issue 21, 2019, pp. 5812-5816.

[20]. L. Xiao, Y. Qiao, Y. He, E. Yeung, Three Dimensional Orientational Imaging of Nanoparticles with Darkfield Microscopy, *Analytical Chemistry*, Vol. 82, Issue 12, 2010, pp. 5268-5274.

[21]. S. Lee, Y. Han, J. Hong, J. Ha, Single gold bipyramids with sharp tips as sensitive single particle orientation sensors in biological studies, *Nanoscale*, Vol. 9, Issue 33, 2017, pp. 12060-12067.

[22]. T. Zhang, H. Shen, G. Lu, J. Liu, Y. He, Y. Wang, Q. Gong, Single Bipyramid Plasmonic Antenna Orientation Determined by Direct Photoluminescence Pattern Imaging, *Advanced Optical Materials*, Vol. 1, Issue 4, 2013, pp. 335-342.

[23]. C. Huang, A. Bouhelier, G. Colas des Francs, A. Bruyant, A. Guenot, E. Finot, J. Weeber, A. Dereux, Gain, detuning, radiation patterns of nanoparticle optical antennas, *Physical Review B*, Vol. 78, Issue 15, 2008.

[24]. R. Chacon, A. Leray, J. Kim, K. Lahlil, S. Mathew, A. Bouhelier, J. Kim, T. Gacoin, G. Colas des Francs, Measuring the Magnetic Dipole Transition of Single Nanorods by Spectroscopy, Fourier Microscopy, *Physical Review Applied*, Vol. 14, Issue 5, 2020.

[25]. J. Liu, A. Maître, L. Coolen, Tailoring Experimental Configurations to Probe Transition Dipoles of Fluorescent Nanoemitters by Polarimetry or Fourier Imaging with Enhanced Sensitivity, *The Journal of Physical Chemistry A*, Vol. 125, Issue 34, 2021, pp. 7572-7580.

[26]. C. Lethiec, J. Laverdant, H. Vallon, C. Javaux, B. Dubertret, J. Frigerio, C. Schwob, L. Coolen, A. Maître, Measurement of Three-Dimensional Dipole Orientation of a Single Fluorescent Nanoemitter by Emission Polarization Analysis, *Physical Review X*, Vol. 4, Issue 2, 2014.

[27]. C. Lethiec, F. Pisanello, L. Carbone, A. Bramati, L. Coolen, A. Maître, Polarimetry-based analysis of dipolar transitions of single colloidal CdSe/CdS dot-in-rods, *New Journal of Physics*, Vol. 16, Issue 9, 2014, p. 093014.

[28]. T. Ha, T. Laurence, D. Chemla, S. Weiss, Polarization Spectroscopy of Single Fluorescent Molecules, *The Journal of Physical Chemistry B*, Vol. 103, Issue 33, 1999, pp. 6839-6850.

[29]. W. Chang, J. Ha, L. Slaughter, S. Link, Plasmonic nanorod absorbers as orientation sensors, *Proceedings of the National Academy of Sciences*, Vol. 107, Issue 7, 2010, pp. 2781-2786.

[30]. J. Lee, Z. Cheglakov, J. Yi, T. Cronin, K. Gibson, B. Tian, Y. Weizmann, Plasmonic Photothermal Gold Bipyramid Nanoreactors for Ultrafast Real-Time Bioassays, *Journal of the American Chemical Society*, Vol. 139, Issue 24, 2017, pp. 8054-8057.

[31]. F. Feng, L. Nguyen, M. Nasilowski, B. Nadal, B. Dubertret, A. Maître, L. Coolen, Probing the Fluorescence Dipoles of Single Cubic CdSe/CdS Nanoplatelets with Vertical or Horizontal Orientations, *ACS Photonics*, Vol. 5, Issue 5, 2018, pp. 1994-1999.

[32]. I. Chung, K. Shimizu, M. Bawendi, Room temperature measurements of the 3D orientation of single CdSe quantum dots using polarization microscopy, *Proceedings of the National Academy of Sciences of the United States of America*, Vol. 100, Issue 2, 2003, pp. 405-408.

[33]. J. Kim, R. Chacón, Z. Wang, E. Larquet, K. Lahlil, A. Leray, G. Colas-des-Francs, J. Kim, T. Gacoin, Measuring 3D orientation of nanocrystals via polarized luminescence of rare-earth dopants, *Nature Communications*, Vol. 12, Issue 1, 2021.

[34]. J. Liu, A. Maître, L. Coolen, Tailoring Experimental Configurations to Probe Transition Dipoles of Fluorescent Nanoemitters by Polarimetry or Fourier Imaging with Enhanced Sensitivity, *The Journal of Physical Chemistry A*, Vol. 125, Issue 34, 2021, pp. 7572-7580.

[35]. N. C. Vu, Z. Ouzit, A. Maitre, L. Coolen, F. Lerouge, J. Laverdant, Single Gold Bipyramid Orientation measured by Plasmon-Resonant Scattering Spectroscopy, in *Proceeding of 4th International Conference on Optics, Photonics, lasers (OPAL'2021)*, Corfu, Greece, 13-15 October 2021, pp. 36-38.

[36]. J. Navarro, D. Manchon, F. Lerouge, N. Blanchard, S. Marotte, Y. Leverrier, J. Marvel, F. Chaput, G. Micouin, A. Gabudean, A. Mosset, E. Cottancin, P. Baldeck, K. Kamada, S. Parola, Synthesis of PEGylated gold nanostars, bipyramids for intracellular uptake, *Nanotechnology*, Vol. 23, Issue 46, 2012, p. 465602.

[37]. J. Navarro, D. Manchon, F. Lerouge, E. Cottancin, J. Lermé, C. Bonnet, F. Chaput, A. Mosset, M. Pellarin, S. Parola, Synthesis, electron tomography, single-particle optical response of twisted gold nano-bipyramids, *Nanotechnology*, Vol. 23, Issue 14, 2012, p. 145707.

[38]. A. Lombardi, M. Loumaigne, A. Crut, P. Maioli, N. Del Fatti, F. Vallée, M. Spuch-Calvar, J. Burgin, J. Majimel, M. Tréguer-Delapierre, Surface Plasmon Resonance Properties of Single Elongated Nano-objects: Gold Nanobipyramids, Nanorods, *Langmuir*, Vol. 28, Issue 24, 2012, pp. 9027-9033.

[39]. Novotny L., Hecht B., Principle of Nano-Optics, *Cambridge University Press,* Cambridge, U.K., 2006.

Sensors & Transducers, Vol. 255, Issue 1, January 2022, pp. 17-23

Sensors & Transducers
Published by IFSA Publishing, S. L., 2022
http://www.sensorsportal.com

Laser Ranging and Nudging in Space Debris Traffic Management

[1, *] Claude Phipps and [2] Christophe Bonnal
[1] Photonic Associates, LLC, 200A Ojo de la Vaca Rd., Santa Fe NM 87501, USA
[2] CNES, 52 rue Jacques Hillairet 75612, Paris Cedex, France
[1] Tel.: +1-215-358-4360, fax: +1-505-466-3877
E-mail: crphipps@aol.com

Received: 13 December 2021 /Accepted: 17 January 2022 /Published: 31 January 2022

Abstract: The number of satellites in LEO is dramatically increasing, from single objects 60 years ago to a predicted 100,000 in 2030. U.S. companies have requested approval for 58,000 new satellites in the next decade, 42k from SpaceX alone. Each week, 3k LEO objects pass each other closer than 1km. In 2018, the European CAESAR conjunction assessment system handled 3M conjunction messages leading to only 17 effective maneuvers. The problem is the low precision with which we know the orbits of these objects. Improving that precision by a factor of 100 will reduce the annual number of false collision alarms to an acceptable level. Just-in-time Collision Avoidance (JCA) can prevent anticipated collisions, given improved ephemeris precision. In this paper we show how this can be done with a 100 ps laser ranging network and one or a few laser nudging stations in orbit. We will discuss the components of this system, as well as an eight-year plan for implementation.

Keywords: JCA, ps laser, Laser ranging, Laser nudging, Space debris traffic management.

1. Introduction

Fig. 1 shows the exponentially growing number of debris in low Earth orbit (LEO). Within the next decade an additional 60 k satellites are expected to be approved, most of which will belong to the SpaceX Starlink system [1] plus additional satellites from other similar planned systems. By 2050, 600 k objects larger than 1cm are predicted to populate LEO [2]. In 1978, Kessler [3] predicted that mutual debris collisions would soon become the largest source of new debris. This is now the case (Fig. 2), as a result of 35 years of bad space housekeeping, which has led to about 10,000 tons of LEO space debris. Space is a commons: trashing it is a disaster that can ultimately trap us on this planet.

In space, no fatalities have occurred yet, but there have been several incidents, including one in November, 2021, in which the International Space Station (ISS) astronauts were forced to abandon the Station and seek protection inside their attached re-entry vehicles. International cooperation is essential to solve the debris problem. In orbit, typical impact velocity is 12 km/s due to the variety of launch latitudes and inclinations. At this velocity, debris have several times the energy density of dynamite.

Despite the fact that SpaceX has designed its satellites to re-enter, the sheer number on orbit will surely lead to more collisions than we have seen in the past. Each week, 3k LEO objects pass each other closer than 1 km [4]. Just-in-time collision avoidance (JCA) [5] can prevent anticipated collisions, but anticipation depends on better orbit ephemeris precision. Laser ranging can improve the present precision by a factor of 100, which leads to a collision false alarm rate of about 100/year, to about 0.02/year [6].

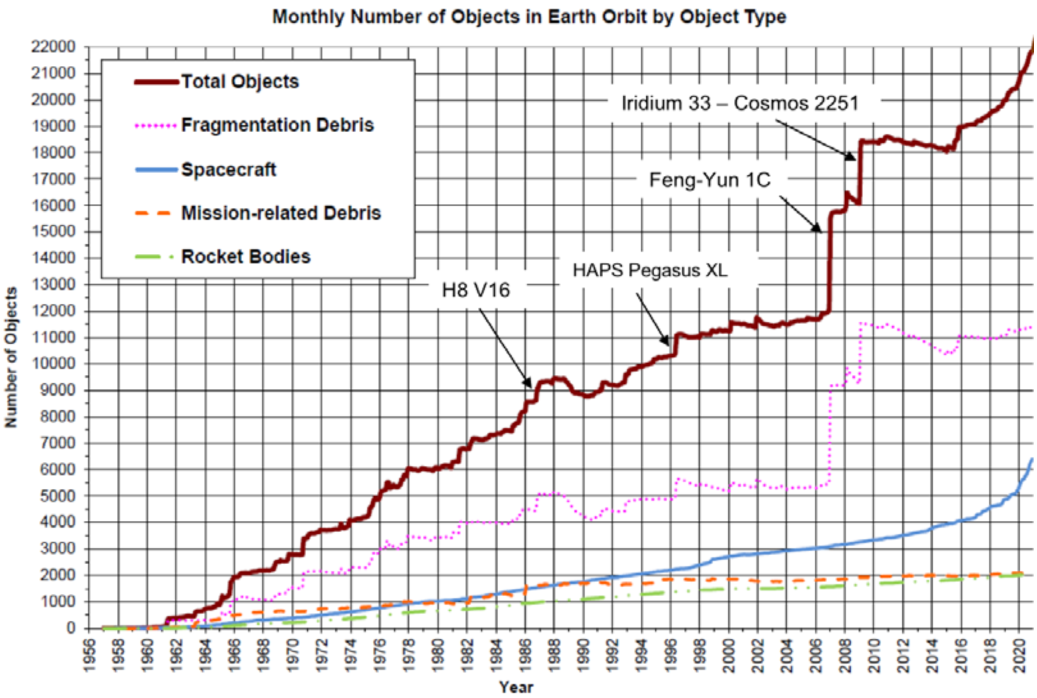

Fig. 1. Debris evolution over time. In early 2021, 36,000 orbital objects were present, of which 24k were catalogued, 94 % of these being debris. Even more are present since the recent experiments demonstrating satellite targeting from Earth [courtesy NASA Orbital Debris Program Office, 2020]. Shown are just the debris larger than 10 cm.

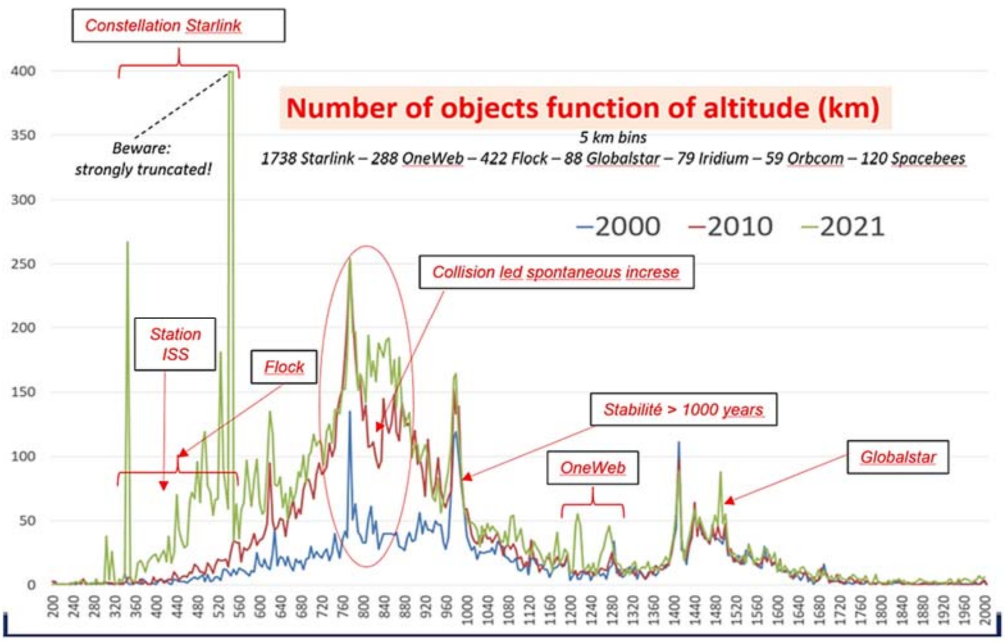

Fig. 2. Debris number in various altitude bins [Courtesy of C. Bonnal].

Then, we can use pulses from a high power laser on the same or a different spaceborne station to nudge one partner in a predicted collision via laser ablation a few days in advance and avoid the collision. Increased orbit precision resulting from laser ranging will permit collision avoidance by imparting a velocity of about 0.15 mm/s 7 days in advance to the selected partner, sufficient to miss the anticipated collision by 280 m.

Fig. 3 illustrates the severity of the debris problem. This figure is a computer-generated image of tracked objects larger than 10 cm in modern times, as viewed from an oblique vantage point in high earth orbit (HEO). 95 % of objects shown are debris, not functional satellites. The cloud is very dense in LEO, but the geosynchronous space (GEO) is also getting crowded. Note the number of objects that exist outside the GEO ring.

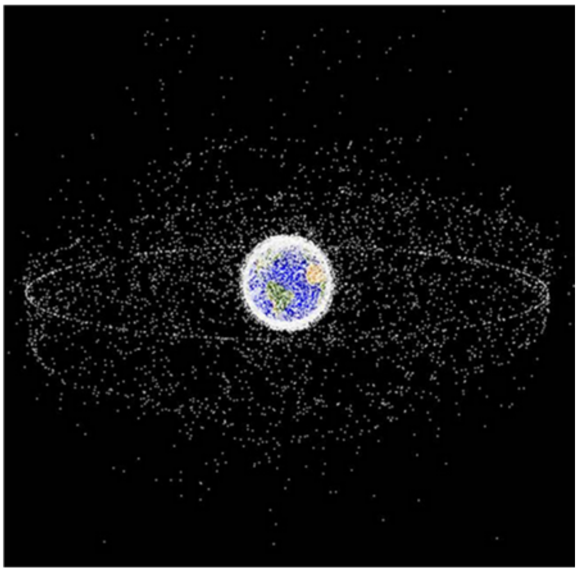

Fig. 3. Illustrating the debris problem (NASA Orbital Debris Program Office, 2020).

2. Precise Object Location

Fig. 4 shows the design of an orbiting telescope and high-efficiency detector system, designed to detect debris objects (>10 cm at 1000 km range, >1 cm at 200 km) under solar illumination.

After a debris is detected, 50 mJ, 100 ps laser pulses are trained on it to measure range to the object with 4 cm precision by timing reflections from tracked objects (Fig. 5). In active mode, it can see a 20 cm target at 1000 km and a 6cm target at 200 km.

Tables 1-3 summarize system performance. Several systems like that shown in Fig. 4 and Fig. 5, moving in equatorial and polar orbits at ~900 km altitude gather data on the debris surface from multiple passes of multiple stations per object. Then, a computer on a “mother ship” will determine the center of mass location of each object studied with 10 cm precision. In Table 1, we assume the minimum signal integration time (60 microseconds per pixel) and a 1ms refresh interval during which noise energy accrues. Table 1 shows system performance in passive target detection, in the solar illuminated mode illustrated in Fig. 4. At 1000 km range, a LEO object moving across the field of view will cross the 1-degree field of view in about 2 s. The 1.54 Gpixel array covers a 40 × 40 km field at 1000 km with 230 cm spot size [Fig. 5]. The pixels have 85 % photoelectric efficiency [7]. Dark current is adequate at 20C. A commercial laser which satisfies our requirements is the EKSPLA PL2231A, which cost about $135k in 2020 [8].

Background signal assumes we are in LEO above 300 km, sun behind us, and looking up or out, but not down at Earth. Background brightness is based on 1 μW/(m^{2}sterradian-μm) [9]. Tables 2 and 3 show ranging laser performance in active mode.

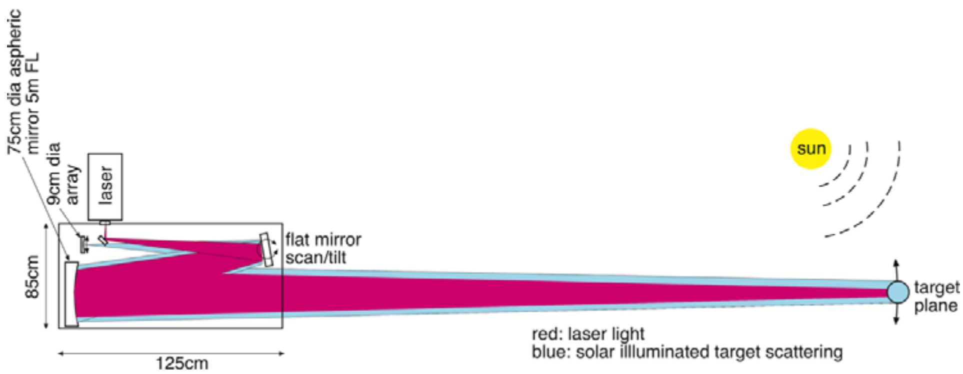

Fig. 4. Passive and active components of LEO ranging system to detect large debris using solar illumination followed by 100 ps “pinging.” Operation is illustrated at 100 km range, where laser spot size is smaller than large targets.

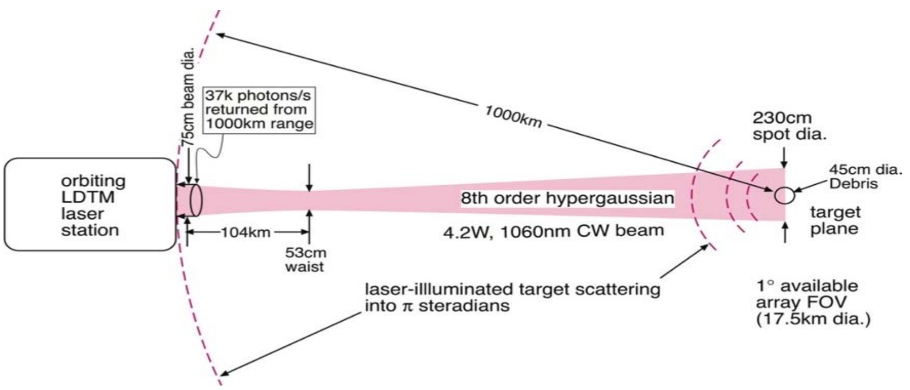

Fig 5. Active ranging subsystem comprising a 50 mJ, 100 ps laser and precision timer to determine range to debris with cτ=3 cm precision. Here, operation at 1000 km range is illustrated, with beamwaist at 104 km.

Table 1. Passive mode: sun-illuminated LEO target.

	Value	Dimension
Operating range	1000	km
Sun spectral brightness	1000	W/(m^{2}sterrad- μm)
Background spect. bright	1E-6	W/(m^{2}sterrad- μm)
Relativistic shift BW	0.025	nm
Target size assumed	10	cm
Range assumed	1000	km
Min. transit time/pixel	60	μs
Aperture diameter	85	cm
Target $R_{diffuse}$	0.25	-
Signal S	1.7E-17	W
Noise N	1.0E-16	W
Signal energy	3.0E-15	J
Background energy	5.8E-22	J
Array refresh interval	1	ms
Signal/Noise energy ratio	2.8E4	-
Photoelectrons/pixel	38	-

Table 2. Ranging laser parameters.

	Value	Dimension
Wavelength	532	nm
Pulse energy	50	mJ
Pulse duration	100	ps
Repetition rate	50	Hz
Laser avg. power	2.5	W
Laser beam quality M^2	2	-

Table 3. Ranging laser active detection system parameters.

	Value	Dimension
Center wavelength	532	nm
Aperture diameter D	85	cm
Target diameter d	20	cm
Target diffuse reflectivity R_d	25	%/sterrad
Beam dia. (0.9*D)	75	cm
Focal length	5	m
Field of view	1	deg
Search area	1600	km^2
N pixels	1.54E9	-
Pixel size	2.25	μm
Array diameter (concave)	8.7	cm
Detector efficiency	85	%
Received signal S	1.3E-17	J
Refresh time	1	ms
Background B (gated)	4.4E-23	J
Spot diameter at range	2.3	m
Target diffuse reflectivity	0.25	-
S/B	3.0E6	-
Target $v_\perp$ at range	7500	m/s
Min transit time/pixel	60	μs
Rec'd photo-electrons	30	-
Signal stability $1/N_{pe}^{0.5}$	18	%
Min target at 208 km	6.5	cm
Dark current at 20C	0.3	e/pulse/ms

3. Diffraction

Please refer to Fig. 5. For long range systems such as ours, the place to start is the beam diameter at the launch aperture. From Table 3, this is 75 cm. Next, the Rayleigh Range (the position at which intensity is doubled for a Gaussian beam) is determined, from

$$z_R = \frac{\pi w_o^2}{M^2 \lambda}, \quad (1)$$

which gives us the distance from the beamwaist to the aperture. W_o is the waist radius. Note that a beam with quality M^2 behaves just like a beam with wavelength $M^2\lambda$. Beyond the waist, as the beam expands at range $z' = z - z_R$ we can write without approximation:

$$w^2 = w_o^2[1+(z'/z_R^2)] \quad (2)$$

From this result, we know the beam area $A=\pi w^2$ on the target and can compute fluence $\Phi=W/A$ where W is pulse energy. To compute the return energy, we assume a pulse energy R_dW is returned into π sterradians. This approach is a worst case, because most objects have roughly flat surfaces that return light into a much narrower beam than we assumed in calculating he parameters in Fig. 5 and Table 3.

4. Nudging the Target

Fig. 6 illustrates nudging a target satellite. The Fig. 4 system is collinear with the Fig. 6 high power, single pulse high energy laser. This laser can apply its Δv from hundreds of km, providing intensity on target is sufficient to produce a plasma and initiate ablation. The requirements for that are a fluence value [10].

$$\Phi_{opt} \sim B\sqrt{\tau}\ \text{J/m}^2 \quad (3)$$

We take $B=4.0E8$ J/m^2 for robust coupling to most spacecraft materials at pulse duration τ, giving $\Phi_{opt}=4.0$ kJ/m^2 in a 100 ps pulse. §3 can be used to determine fluence at range. In Fig. 6, "L'ADROIT" refers to an orbiting debris removal station design [10].

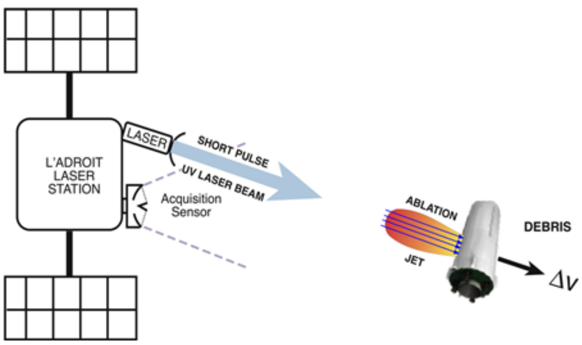

Fig. 6. Illustrating debris nudging.

4.1. Perturbing Orbits

Where $\mu = GM_{Earth}$, r is radius from the elliptical orbit focus (geocentric radius for small satellites) and a is the semi-major axis of the ellipse, total energy per unit mass ε for an unperturbed orbit is given by

$$\varepsilon = v_{orb}^2 / 2 - \mu / r = -\mu / 2a \tag{4}$$

The vis viva equation for velocity v in an unperturbed orbit is

$$v^2 = \mu(2/r - 1/a) \tag{5}$$

If we now perturb the orbit with a laser impulse with energy W which delivers an energy change $C_m W v_{orb}$ we can differentiate Eq. (5) to find for an object of mass m,

$$\Delta\varepsilon = \pm(\frac{\mu}{2a^2})\Delta a = C_m W v_{orb} / m \tag{6}$$

Considering that the orbital period is given by

$$T = 2\pi a^{3/2} / \mu^{1/2} \tag{7}$$

which can be differentiated to give

$$\Delta T = 3\pi(a/\mu)^{1/2}\Delta a$$

so that

$$\Delta T = 3\pi(a/\mu)^{1/2}(\frac{2a^2}{\mu}\Delta\varepsilon) = (3aT/\mu)\Delta\varepsilon$$

and that the change in period of the perturbed object is

$$\Delta T = \pm 6\pi W C_m (\frac{a^2}{\mu M}) \tag{8}$$

Eq. (8) works even for a CW signal if its duration is short compared to T. But W in Eq. (8) must always be used with the correpondng C_m.

Table 4 shows how we can apply all this. Please note that this high power pulse laser, is a separate device from the 50 mJ unit in Table 2, and makes only one shot to produce a 280 m miss in 7 days, giving it a lot of flexibility to address many targets. Its 800 km range addresses a large enough volume to find a particular debris quickly. Note that focal spot position dither means nothing for a 100 ps pulse focal spot fluence. No vibrations are that fast.

We suggest that the 3 m diameter focusing aperture can be a phase plate imprinted on a flat reflector simulating an off-axis paraboloid and assembled from segments in orbit. Secondary optics in the laser train feeding this optic adjust the focus location in real time within the indicated range. At shorter range, laser pulse energy is reduced. Coupling coefficient values in Table 4 were estimated from earlier measurements [11]. Pointing precision is referenced in [12].

Table 4. Target mechanical coupling parameters.

	Value	Dimension
Coupling coefficient C_m	30E-6	N-s/J
Wavelength	355	nm
Aperture diameter	3.0	m
Beam quality M^2	1.5	-
Focal spot dia. at range	40	cm
Range	800	km
Pointing precision	300	nrad
Corresponding focus dither	24	cm
Target mass	1000	kg
Nudging laser energy	5.0	kJ
Fluence on target	40	kJ/m²
Target Δv from one shot	150	μm/s
Target ΔT	3.9	ms/orbit
Pulse duration	100	ps
Semimajor axis change Δa	±29	cm
Miss distance v_{orb} ΔT	2.8	m/period
Miss distance v_{orb} ΔT	280	m/week

4.2. Design of a JCA Station

Fig. 7 shows a polar orbiting JCA station in action.

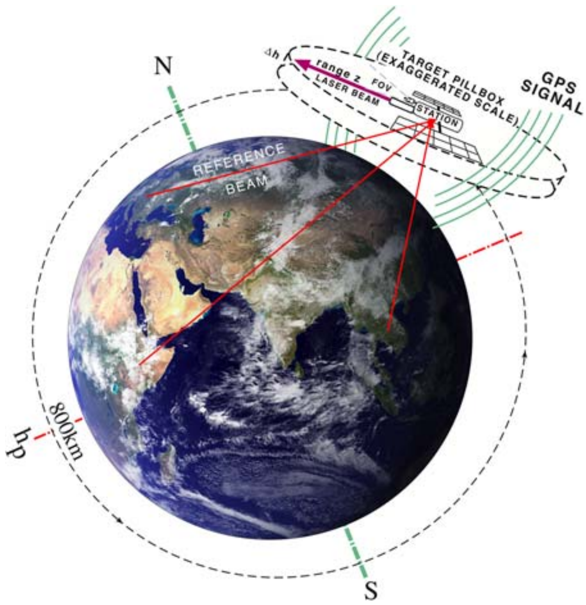

Fig. 7. Polar orbiting JCA Station.

In operation, this 100 ps laser ranging station (one of many) accurately locates a debris facet relative to the station. In turn, the station is located relative to Earth by onboard GPS and multiple Earth stations pinging a retroreflector on the station.

Using inputs from many stations, a computer on the "mother ship" combines the data to determine the center of mass location of a particular debris with 10 cm precision. In Table 5, we take 19,000 satellites to be surveyed by an individual JCA station, and 0.1 % of these to require special care because of their proximity to other assets. Ten stations in various equatorial or polar orbits can provide redundant measurements for those, getting center of mass location accurately.

Table 5. JCA system parameters.

	Value	Dimension
Altitude h	800±50	km
Orbit period T	101	min
Pillbox thickness	600	km
Pillbox volume V	1.88E9	km^3
Number satellites watched	19000	-
Satellite density	6.2E-8	km^{-3}
Target objects in pillbox	120	-
Watched sat detection rate	4700	hr^{-1}
Sats to nudge (0.1% /day)	1	day^{-1}
Time to find a particular sat	4	hrs

5. Alternative Designs

In this section, we will compare earth-based and space-based ranging systems in order to show the inherent advantages of the pulsed system we propose, and briefly discuss CW laser ranging with frequency modulation, the design approach used in automobile collision-avoidance lidar.

5.1. CW Laser Ranging?

Using the same geometry and procedures as generated Fig. 5 and Table 1, we can calculate that to obtain the same spectral brightness as the sun (Table 1) on target, a 532 nm CW laser with 100 nm bandwidth and 1.3 kW output would be required. This figure could be improved by shifting the frequency of the transmitted signal in a pseudorandom sequence that repeats every 3.3 ms (to match 1000 km range) and cross-correlating the return with the outgoing signal. However, there are other problems with CW.

In order to provide the 0.15N-s impulse necessary to nudge the target (see Table 4) using light pressure alone, for which C_m=6.7E-9N/W, assuming a target availability interval of 30 s, a laser power of 750 kW would be needed. At 25 % electrical efficiency for the laser, a power supply capable of 3MW is necessary. Over the 30 s availability interval, 90MJ stored electrical energy would be required. These parameters are not practical.

5.1. Ground-based Laser Ranging?

Problems are both physical and practical (Table 6). Clearly, it would take a lot of fixed Earth-based stations to equal the capability of one orbiting station.

Because sky background brightness is more than 100 times greater for an Earth-based station, small targets would be much more difficult to find.

Table 6. Earth-based laser ranging.

	Earth	Space
Search volume (±45°) km^3	1.4E9	1.9E9
Sky background brightness	7.5E-9	1E-6
Time to find one satellite	2 weeks*	4 hrs
Weather a problem?	Yes	No
Scintillation (adaptive optics)	Yes	No
Nonlinear refraction	Yes	No
Centimetric precision	No	Yes
Operating time (hrs)	12	24

Note: * depends critically on satellite orbit and station location – could be infinite.

6. Stepwise Approach

Because many nations' properties are involved in the space commons, an attempt to range, let alone nudge satellites requires careful planning and international consultation. To do this will require a multi-year program. We propose the following sequence:

1. Develop a small laser ranger for demonstration purposes.
2. At first, use this only on large known French debris such as Ariane 1-4 upper stages.
3. Compare results to the well-known ephemerii from the French COSMOS system based on the Graves radar [13].
4. When feasibility is proven, develop larger laser ranging station compatible in size with the European Vega launcher.
5. Develop a global legal agreement to allow laser ranging on catalogued debris. Gains from such operations on defunct objects should guarantee acceptance.
6. Because known ephemerii will control the initial operation, the risk of wrongly pinging active assets is negligible.
7. Develop the slightly larger JCA system couple with the ranging function to minimize the false alarm rate.
8. When feasibility of this is shown, use the JCA system to significantly modify orbits of large derelicts as previously proposed in the description of L'ADROIT [10, 14].

7. Conclusions

It has been the purpose of this paper to outline a practical solution to abating the problem of mutual collisions among satellites before we are trapped on this planet by a cloud of debris created by these collisions. The plan is to locate all objects in LEO sufficiently precisely to avoid false collision alarms and to predict actual collisions several days in advance. Armed with this knowledge, we can use a nudging laser system which, by imparting a tiny velocity change a week in advance, will eliminate collisions altogether.

Acknowledgements

We gratefully acknowledge the encouragement of Prof. Dr. Sergey Yurish of IFSA to produce this paper.

References

[1]. I. Klotz, Starlink Satellites Interfering with Astronomical Observations, *Aviation Week and Spase Technology,* 5 March 2020.

[2]. H. Klinkrad, Space Debris: Models and Risk Analysis, *Springer Praxis Books*, 2006.

[3]. D. J. Kessler, B. G. Cour-Palais, Collision Frequency of Artificial Satellites: The Creation of a Debris Belt, *J. Geophys. Res.*, Vol. 83, Issue A6, 1978, pp. 2637-2646.

[4]. C. Smith, Remote manoeuvre of space debris using photon pressure for active collision avoidance, in *Proceedings of the 5th European Workshop on Space Debris Modeling and Remediation,* 2018, Paper 7.2.

[5]. C. Bonnal, D. McKnight, C. Phipps, C. Dupont, S. Missonnier, L. Lequette, M. Merle, S. Rommelaere, Just in time collision avoidance – a review, *Acta Astronautica,* Vol. 170, 2020, pp. 637-651.

[6]. H. Krag, *et al*., Groundbased laser for tracking and remediation – an architectural view, paper IAC-18-A6.7.1, in *Proceedings of the* 69th *International Astronautical Congress (IAC'2018)*, Bremen, 2018.

[7]. Based on published specifications of Fairchild Imaging CCD456 (1 nA/cm^2)

[8]. S. Guthrie, Altos Photonics, *Private Communication*, 25 June 2019.

[9]. Ch. Leinert, *et al*., The 1997 reference of diffuse night sky brightness, *Astron. Astrophys. Suppl. Ser*., Vol. 127, 1998, pp. 1-99.

[10]. C. Phipps, L'ADROIT – A spaceborne ultraviolet laser system for space debris clearing, *Acta Astron.,* Vol. 104, 2014, pp. 243-255.

[11]. C. R. Phipps, M. Boustie, J.-M. Chevalier, S. Baton, E. Brambrink, L. Berthe, M. Schneider, L. Videau, S. A. E. Boyer, S. Scharring, Laser Impulse Coupling measurements at 400 fs and 80 ps using the LULI facility at 1057 nm wavelength, *J. Appl. Phys.*, Vol. 122, 2017, 193103.

[12]. M. Aguirre, J.-L. Bezy, ESA activities related to high resolution imaging from GEO, *ESRIN*, 15 April 2010, page 51.

[13]. IAA Situation Report on Space Debris, http://www.iaaweb.org/iaa/Scientific%20Activity/sg514finalreport.pdf

[14]. C. Phipps, C. Bonnal, A spaceborne, pulsed UV laser system for re-entering or nudging LEO debris, and re-orbiting GEO debris, *Acta Astronautica*, Vol. 118, 2016, pp. 224-236.

Sensors & Transducers, Vol. 255, Issue 1, January 2022, pp. 24-34

Sensors & Transducers
Published by IFSA Publishing, S. L., 2022
http://www.sensorsportal.com

High Performance InAs/InP Quantum Dash Frequency Comb Laser for High Capacity RoF Wireless Networks

[1, *] Youxin Mao, [1, 2] Khan Zeb, [1] Zhengou Lu, [1] Jiaren Liu, [1] Guocheng Liu, [1] Philip J. Poole, [1] Mohamed Rahim, [1] Grzegorz Pakulski, [1] Pedro Barrios, [1] Weihong Jiang and [2] John Zhang

[1] Advanced Elect. and Photonics Research Centre, National Research Council Canada, Ottawa, ON, Canada
[2] iPhotonics Labs, Dept. of Elect. and Computer Engineering, Concordia University, Montreal, QC, Canada
[*] Tel.: + 613-993-7331
E-mail: youxin.mao@nrc-cnrc.gc.ca

Received: 23 November 2021 /Accepted: 30 December 2021 /Published: 31 January 2022

Abstract: We demonstrate a high performance C-band semiconductor quantum dash (QD) mode-locked laser based optical frequency comb (OFC) with buried heterostructure (BH). Theory of timing jitter is presented including characterization methods from both the 1st homonic RF power spectral density and optical phase noise. Experimental results of relative intensity noise (RIN), phase noise, and timing jitter are compared from QD mode-locked optical frequency comb having BH structure to that with conventional surface ridge structure in the same repetition rate of 25 GHz. It is demonstrated that the laser with BH structure exhibits significantly reduced RIN, phase noise, and timing jitter compared to the surface ridge structure. The performance of BH QD OFC is also evaluated in broadband optical heterodyne based radio-over-fiber fronthaul wireless links at 5G New Radio of around 25 GHz with a total bit rate of 16-Gb/s.

Keywords: Semiconductor quantum dot or dash mode-locked laser, Optical frequency comb, Buried hetero-structure, Phase noise, Timing jitter, Radio-over-fiber, 5G new radio.

1. Introduction

To meet rapidly increased demand for wireless and internet worldwide and to overcome the global shortage of RF bandwidth, high-speed networks and the millimeter-wave (mm-wave) spectra are expected [1] to increase data capacity and the wireless frequency bandwidth. To keep symbol rates compliant with the electrical bandwidth of energy-efficient CMOS driver circuitry, a technical implementation of such networks requires higher-order modulation formats along with parallel transmission on multitude of wavelength channels [2]. In these circumstances, optical frequency combs (OFCs) become particularly attractive light sources to generate large numbers of well-defined carriers for wavelength-division multiplexing (WDM) in a single chip-scale device. Particularly one of the important advantages of CFCs is that the comb lines are inherently equidistance in frequency, hence, easing the requirements for inter-channel guard bands and avoiding frequency control of individual lines as needed in conventional used arrays of independent DFB lasers. These advantages do not only apply to the WDM transmitter but also to the receiver, where an array of discrete local oscillators (LO) may be replaced by a single CFC [3] and possibly with the same CFC as the transmitter light source.

OFCs generated by monolithic semiconductor mode-locked lasers (MLLs) have been demonstrated to be efficient for WDM based communication networks owing to compact size, low power consumption, wide optical bandwidth with a flat optical spectrum, and the ability for hybrid integration with silicon substrates. It has been demonstrated that using quantum dots or dashes as the active gain medium instead of bulk layers or quantum wells for semiconductor lasers a number of enhancements in device performance were found [4-5]. These include sharp increase in the density of states and reduction in the amount of amplified spontaneous emission rates, which leads to lower intrinsic noise, lower threshold current densities, lower sensitivity of the threshold current to temperature, reduced chirps, broader spectral gain bandwidths, narrower mode linewidth, and faster carrier dynamics. The QD single-section passively (SSP) MLLs or called passively MLLs are more promising OFCs for the next generation of high-speed networks [6-8]. Due to without a saturable absorber section, the SSP MLLs achieve mode-locking results in an increased average output power, simpler fabrication, able to make higher repetition rate [9, 10].

Significant reductions of phase noise and pulse jitter have been reported using active mode-locking [11], hybrid mode-locking [12, 13] and optical injection [14-16] methods in frequency comb QD lasers at 1300 nm wavelength. It is shown that the best suppressing level of time jitter could be down to sub-hundred femtosecond [14], but all these methods have the same disadvantage of requiring extra complex and expensive equipment, such as an extra light source, modulator and high-frequency electrical signal generator, etc. The feed-back locking methods of phase noise and timing jitter reduction have been investigated in passively MLLs [17-19] and in application in WDM transmission [20]. The results of 3dB RF linewidth reduction from 187 kHz to 1.9 kHz corresponding to a pulse-to-pulse jitter reduction to 23 fs have been obtained in a 40 GHz InAs/GaAs QD MLL [9, 21]. Although the method of optical external cavity self-injection feedback is a powerful technique for linewidth and pulse jitter reduction, this technology still need a precise alignment with external cavity and the performance sensitive to the external mode-locking conditions.

We have previously demonstrated InAs/InP QD MLLs with pulse repetition rates from 10 GHz to 437 GHz and a total output power up to 50 mW per facet at room temperature [22-31]. We have recently demonstrated femtosecond timing jitter in InAs/InP QD C-band SSP MLLs with surface ridge waveguide structure by both analysis of the Lorentzian linewidth of the first harmonic RF PSD [32] and optical linewidth [33]. In this paper, we carry out an investigation of various properties of 25 GHz C-band QD Febry-Perot (F-P) MLL based SSP OFC with buried heterostructure (BH) waveguide to extend the study in [34]. Firstly, we theoretically analyze timing jitter and its measured methods for a QD F-P MLL, which is a critically important parameter for high-speed network applications. Then we give a full description of laser fabrication and performance characterization. Furthermore, we compare the measured results of RIN, phase noise and timing jitters from QD F-P MLL with BH structure to a conventional ridge structure. The results show the performance is significantly improved by using BH structures as the laser gain waveguide. To our knowledge, this is the first time in the literatures for making these comparisons. Lastly, we report on application of the 25 GHz QD F-P MLL based OFC for fiber-wireless integrated 5G new radio fronthaul systems with 16-QAM modulated data formats and optical heterodyne detection using both signal modulated signal and LO reference from the same OFC. Those results postulate a complete perspective on these semiconductor QD MLLs as OFC sources for the purpose of being employed in mm-wave RoF transmission systems.

2. Theory of Timing Jitter

Generally, the noise effects in a semiconductor mode-locked laser are mainly from the amplitude, the central optical frequency, the pulse frequency spacing, and the optical phase, but the broadening of the mode lineshape in the passively MLL is dominated by the contributions of optical phase noise and pulse timing fluctuations [35, 36]. The phase and timing fluctuations in each mode are affected by amplified spontaneous emission noise going through a random walk process [37]. Therefore, the timing jitter exhibits a diffusion-like behavior. If $\Delta t_r(t)$ expresses the timing fluctuations in the mode position at time t, the timing jitter σ can be described by a Gaussian random process with mean = 0 and total variance $\sigma = <|\Delta t_r(t)|^2> = Dt$, where D is the timing jitter diffusion constant. Then phase fluctuation follows the behavior $\Delta\theta(t) = 2\pi f_0 \Delta t_r(t)$, where f_0 is the center frequency or repetition rate. From analyzing the complex electric field of a semiconductor passively MLL, considering only the effects of phase and timing fluctuations, the complex optical field is [36]

$$E(t) = \sum_{n=-\infty}^{\infty} A[t - n\Delta t(n)] e^{-j[2\pi f_0 (t - nT_0) + \Delta\theta(n) + \phi(n)]}, \quad (1)$$

where $A(n)$, $\Delta t(n)$, $f_0(n)$, $\Delta\theta(n)$ and $\phi(n)$ are respectively the mode envelope, timing fluctuations, the center frequency, phase noise, and static phase of the n_{th} longitudinal mode. T_0 is the repetition period and $f_0 = 1/T_0$. Following [38], the optical spectrum can be calculated by taking the electric field autocorrelation function and Fourier transform. A set of Lorentzian modes with frequencies f_n and the FWHM linewidths Δf_n compose the optical spectrum as

$$S(\upsilon) \sim \frac{\left|\hat{A}(f-f_0)\right|^2}{\pi} \sum_{n=-\infty}^{\infty} \frac{\Delta f_n}{(f-f_n)^2 + \Delta f_n{}^2}, \qquad (2)$$

where $\hat{A}$ is the Fourier transform of the mode envelope. The quantum limited optical phase noise and timing jitter random walk fluctuations induce the Lorentzian mode shape in all the longitudinal modes [35]. The FWHM optical mode linewidth is [39]

$$\Delta f_n = \Delta f_{min} + 2\pi f_0^2 D(n - n_{min})^2, \qquad (3)$$

where n_{min} is the mode number corresponding to the minimum linewidth Δf_{min}, Δf_{min} would be the linewidth for all the modes if there was no timing fluctuations.

In the same way, the spectrum of the laser intensity, or more commonly called the radiofrequency (RF) spectrum of beating note, can be calculated as a set of Lorentzians with the FWHM linewidth of m_{th} harmonic expressed by Δf_{RFm} [36]

$$S_{RF}(\upsilon) \sim \frac{1}{\pi} \sum_{n=-\infty}^{\infty} \frac{\Delta f_{RFm}}{(f - mf_0)^2 + \Delta f_{RFm}^2} \qquad (4)$$

It is found that the RF spectrum is consist of a sum of Lorentzian modes centered at mf_0 with each harmonics corresponds to the beating between a pair of modes separated by m-1 modes in the optical spectrum. At any given value of m, each harmonics will have integer m^2 proportional multiple to the 1st harmonic linewidth and related to D given by [39]

$$\Delta f_{RFm} = \Delta f_{RF1} m^2 = 2\pi f_0{}^2 D m^2 \qquad (5)$$

From the coefficients of Eq. (5), the relationship between the first harmonic RF spectrum linewidth and timing jitter diffusion constant D can be extracted and are given by

$$\Delta f_{RF1} = 2\pi f_0^2 D \qquad (6)$$

RF spectrum could be possibly perturbed by the amplitude noise as in the case of actively mode-locked laser [40]. Higher harmonics of the photocurrent could be used to distinguish between phase noise and amplitude noise. However, in passively MLL, the amplitude noise is dominated by the phase, consequently using any different order of the harmonics has no influence on the RF linewidth [41] as shown in Eq. (5).

From Eq. (3) and Eq. (6), for a passively MLL, the optical mode linewidth Δf_n and the 1st RF harmonic linewidth Δf_{RF1} are related by way of

$$\Delta f_n = \Delta f_{min} + \Delta f_{RF1}(n - n_{min})^2 \qquad (7)$$

Eq. (7) shows that the first harmonic RF linewidth Δf_{RF1} of the semiconductor passively MLL can be estimated from measuring the optical linewidth, i.e. optical phase noise, of each longitudinal mode and performing a parabolic fit as a function of mode number.

From the well-known method developed by von der Linde [40] for actively mode-locked lasers, phase noise spectrum $L(f)$ is equal to the normalized RF power spectral density (PSD) $P(f)$ as shown in Fig. 1 (a) in one Hz bandwidth, and is given by

$$L(f) = \frac{P(f - f_0)}{RBW * P_{tot}}, \qquad (8)$$

where f_0 and P_{tot} are the carrier peak frequency and total integrated power of the RF PSD, respectively, and RBW is the resolution bandwidth used in the RF spectrum analyzer. Drzewietzki, *et al.* [42] verified that this phase noise estimation method is only valid for passively MLLs at frequency offsets well above the carrier peak linewidth. Fig. 1 (b) shows a typical phase noise spectrum $L(f)$ for a passively MLLs, where f_1, f_2, f_3, and f_4 indicate the frequency boundaries of the different noise mechanisms with various slopes, such as flicker frequency modulation ($1/f^3$), white flicker frequency noise ($1/f^2$), flicker phase modulation ($1/f^1$), and white phase noise ($1/f^0$), respectively [43]. The A_{12}, A_{23}, A_{34} and A_{45} represent corresponding noise areas of the different noise mechanisms.

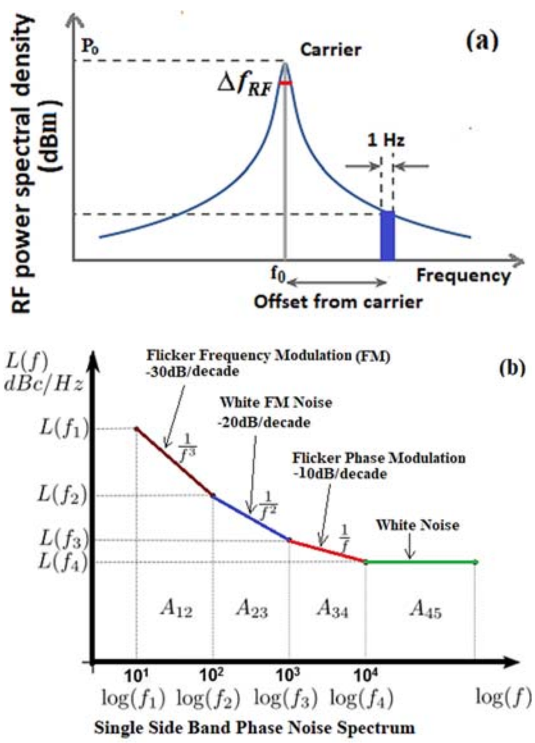

Fig. 1. (a) The 1st homonic RF power spectral density (PSD) with showing FWHM bandwidth and central frequency. (b) A single side band phase noise spectrum with showing the different noise mechanisms with frequency related various slopes.

For the case of an F-P, i.e. passively, mode-locked semiconductor laser, especially for the active region in a laser diode consists of quantum dot or dash (QD) structures is investigated in this work. It is shown that due to material nonlinearities and saturated absorber in the gain area, the phase correlation of the optical longitudinal modes can take place resulting in a four wave mixing process and in passively mode-locking [44]. The common integrated root-mean-square (RMS) time jitter, also called the pulse to clock timing jitter, can be obtained from integration of the single side band phase noise spectrum as shown in Eq. (9) and Fig. 1 (b) by

$$\sigma_{int} = \frac{1}{2\pi f_0}\sqrt{2\int_{f_{low}}^{f_{high}} L(f)df} = \frac{1}{2\pi f_0}\sqrt{2(A12 + A23 + A34 + A45)}, \quad (9)$$

where f_{high} and f_{low} are the upper and lower integration frequencies, respectively, in the interested range and A_{12}, A_{23}, A_{34}, A_{45} are corresponding to the areas of flicker frequency modulation, white flicker frequency noise, flicker phase modulation and white phase noise, respectively [43], as shown in Fig. 1 (b). As pointed out in [42], this phase noise estimation method is only valid for passively MLLs at frequency offsets well above the carrier peak linewidth.

A time jitter estimation method was proposed specifically for a semiconductor passively MLL [41]. The properties of intrinsic phase noise from relatively broadband spontaneous emission in the PML laser leads to a Lorenzian shaped PSD of photocurrent RF phase noise. Study of the linewidth of the first harmonic of photocurrent RF can provide a simple and appropriate way to characterize the timing jitter of a semiconductor PML laser. According to reference paper [41], for a high repetition rate passively MLL, as expressed in f_0, the pulse to pulse RMS timing jitter σ_{ptp} can be expressed as:

$$\sigma_{ptp} = \frac{1}{f_0}\sqrt{\frac{\Delta f_{RF}}{2\pi f_0}}, \quad (10)$$

where Δf_{RF} is the full width at half maximum (FWHM) Lorentzian linewidth of the first harmonic of RF power spectral density. By measuring the first harmonic of photocurrent RF PSD of a semiconductor PML laser and fitting the peak with a Lorentzian function, time jitters can be estimated. From Eq. (10), it is noticed that for a certain repetition rate f_0, the pulse to pulse timing jitters of a semiconductor PML laser are proportional to square root of the Lorentzian linewidth of the RF PSD of the laser. Therefore, the FWHM of the radio-frequency (RF) beat note from a semiconductor MLL determines the level of phase coherence between the modes of the optical frequency comb (OFC).

From Eq. (7), the first harmonic RF linewidth Δf_{RF1} can be estimated by measuring the optical phase noise of each longitudinal mode and performing a parabolic fit as a function of mode number. Therefore, the pulse to pulse jitter can be estimated from optical phase noise measurements by parabolic curve fitting as shown in Eq. (10). This method does not require a direct measurement of the RF PSD which for a high repetition rate laser necessitates the use of a high speed photodetector. Therefore, this method is not restricted to measuring lasers with repetition rates below ~100 GHz.

3. Material Grown and Decice Fabrication

InAs QD is grown initially with an InP buffer following by lattice matched InGaAsP (1.15Q), 1.15 μm PL peak at 300 K, by chemical beam epitaxy (CBE) on exactly (001) oriented n-type InP substrates, as shown in Fig. 2 (a). The laser active region consists of five stacked layers of InAs quantum dashes as shown a cross-sectional scanning electron microscopy (SEM) imaging in Fig. 2 (b). The five InAs dash layers were deposited followed by a 25 s growth interruption for each layer to allow the In to diffuse on the surface and form dashes. The average QD density in each active layer was around $3.5 \times 10^{10} cm^{-2}$.

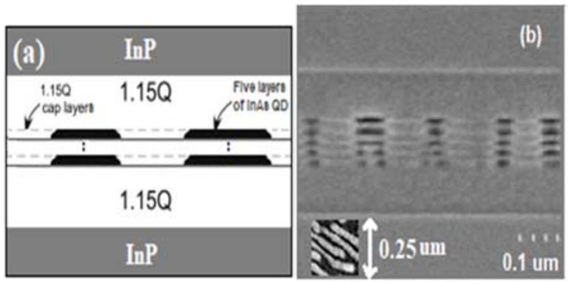

Fig. 2. (a) Schematic diagram of a InAs quantum dash (QD) grown structure; (b) SEM images of the front cross-sectional of the five quantum dashes layers. Inset: the top view of a QD layer in the active region for gain material of the QD MLL.

The each dash layers is then capped with 1.15Q barrier layer and finally capped with 1.15Q and InP. The waveduide core was surrounded by n- and p- type InP cladding layers. This core structure provides both carrier and optical confinement in the active region emitting in C-band wavelength range. Inset in Fig. 1 (b) shows SEM imaging of the top view of the QD layers. More detailed information of the QD material growth is contained in [44]. Two laser structures of buried hetero-structure (BH) and conventional surface ridge (SR) waveguides are fabricated with the same processing environment in this study.

The QD buried heterostructure (BH) MLL is an InP-based p-n blocked BH Fabry-Perot (FP) laser. Fig. 3 (a) shows a schematic of the cross-section of the laser.

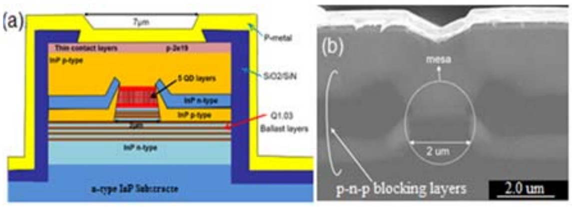

Fig. 3. (a) A schematic front cross-sectional diagram, and (b) SEM images of the fully processed F-P QD MLL with a buried BH waveguide structure.

The laser structure is comprised of a 170 nm thick InGaAsP waveguide core with 10 nm InGaAs P (1.15Q) barriers embedding five stacked layers of InAs QDs as the active gain region surrounded by n- and p- type InP cladding layers. After growing the laser core, a 2 μm wide waveguide mesa was created by etching through the 1.15Q waveguide core followed by the selective area epitaxy overgrowing of pnp blocking layer structure to confine current and light to the waveguide mesa. Then after removing the selective area dielectric mask, the final p-type InP cladding and contact layers were grown. Both facets of the laser were left uncoated. A SEM image of the front cross-section of a fully fabricated QD BH MLL laser is shown in Fig. 3 (b).

The cleaved laser chip with desired cavity length is mounted onto a commercially available Aluminum Nitride (AlN) chip-on-carrier (CoC) with two gold (Au) electroplated contacts to provide mechanical support and electrical connection to the laser chip, where the bottom contact provides a cathode connection through Eutectic Gold Tin (AuSn) and the top contact provides the corresponding anode connection through wire-bonding. For the experimental characterization of the QD MLL and to reduce the power driving noise and environment temperature frustration, the CoC is placed on a copper block with a thermoelectric cooler (TEC) underneath to maintain an operating temperature range of 16 – 20°C and an ultra-low-noise battery powered laser diode driver controller (LDC) (ILX Lightwave, Model LDC-3722) used to DC bias and the corresponding TEC. The laser output light is collected from its front facet using a collimated lensed polarization maintaining (PM) fiber attached to an isolator for reducing any back-reflections. The position of this fiber is adjustable in three dimensions for coupling the light optimally from the laser cavity.

4. Experimental Results and Discussions

Fig. 4 (a) shows a typical measured laser L-I characteristic curve of a 25 GHz QD F-P MLL with buried heterostructure structure at 19 °C. It can be seen that the laser threshold current is at around 50 mA and provides an average output power up to 50 mW at around 450 mA. By comparing the L-I curve of BH laser to that of ridge laser as shown in Fig. 4 (a), it is observed that differential efficiency of BH laser is higher than ridge laser, so the output power is higher for BH laser when the driving current larger than 250 mA. The laser output spectrum is characterized using an optical spectrum analyzer (Anritsu, Model AQ6317B) with a resolution of 0.01 nm at driving current of around 423 mA as shown in Fig. 4 (b). The laser operates in the shorter part of the C band with its central wavelength of around 1531 nm and 6-dB optical bandwidth of around 9 nm providing about 47 highly coherent optical channels.

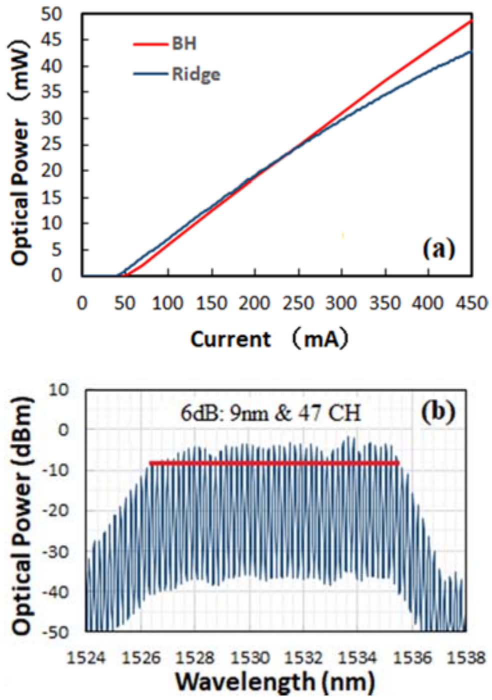

Fig. 4. Measured (a) L-I characteristics and (b) optical spectrum of a 25 GHz QD BH F-P MLL.

To verify the noise performance of the 25GHz QD BH MLL, typical RIN and frequency noise spectra from an individual comb line are charactrizated as shown in Fig. 5 (a) and (b), respectively. For comparison purpose, the noise performances from a 25 GHz QD MLL with surface ridge structure are measured in the same experimental conditions as shown in Fig. 5 as well. RIN is measured using Agilent N4371A measurement system. Although RIN does not usually play an important role in the coherent communications, since balanced receivers suppress the RIN influence of both the carrier and the LO. However, due to the comb modes constantly exchange energy amongst each other caused by mode partition noise [45], the RIN of the individual comb lines usually is high and cannot be neglected, especially in the application in an optical heterodyne based RoF fronthaul wireless network where a single optical receiver is used. From measured RIN spectra over the frequency range of 10 MHz to 10 GHz shown in Fig. 5 (a), we achieve an integrated average RIN value of -143.3 dB/Hz for the QD BH MLL, which is about 6 dB lower than that of the QD MLL with ridge structure. Such low RIN values are attributed to the characteristics of QD material inside the laser cavity with very low mode partition noise in the BH waveguide active region. Fig. 5 (b) shows measured frequency noise and it can be seen that the frequency noise is at least 10 times lower in the case of BH QD MLL in the high frequency range compared with ridge structure laser.

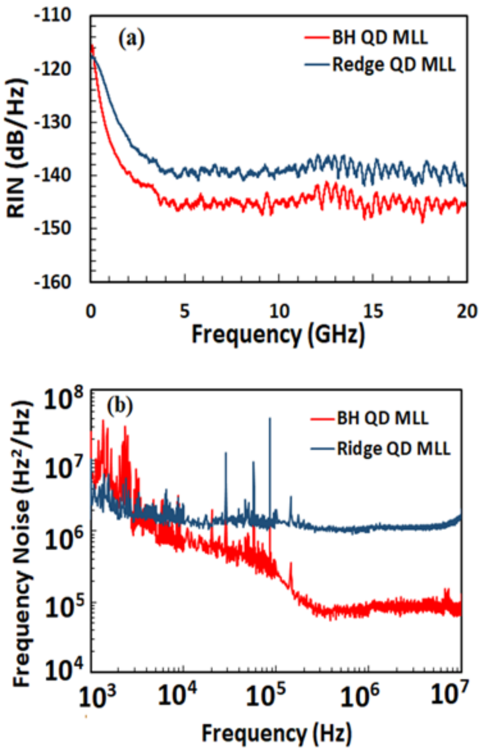

Fig. 5. Measured single channel RIN (a) and frequency noise spectra (b) from a 25 GHz QD BH F-P MLL in comparison to that obtained from a QD ridge F-P MLL with the same repetition rate in the same measured conditions.

To characterize the phase noise performance of the laser, selected individual optical channels covering the spectrum of the laser in the C-band are filtered out using an optical band pass filter. The optical spectral linewidth, i.e. phase noise, for some of the selected channels from 1526.4 nm to 1535.8 nm (covering 47 modes) is estimated from the measured optical frequency noise spectrum using an automated laser linewidth / phase noise measurement system (OEWaves Inc. OE4000) as shown in Fig. 6 (a). The performance is characterized for QD ridge MLL under the same measured conditions. It is indicated as shown in Fig. 6 (a) that the measured phase noise for the QD BH MLL is in between 0.13 MHz to 0.46 MHz, which is much lower than the measured phase noise from 0.97 MHz to 5.5 MHz for laser in SR structure.

For analysis of the timing jitter from optical phase noise, the measured curves of phase noise vs. mode channel number are parabolic fitted using Eq. (7). The fitting results of $\Delta\upsilon_{nim}$, n_{nim} and $\Delta\upsilon_{RF1}$ for both lasers are listed in Table 1 for comparison.

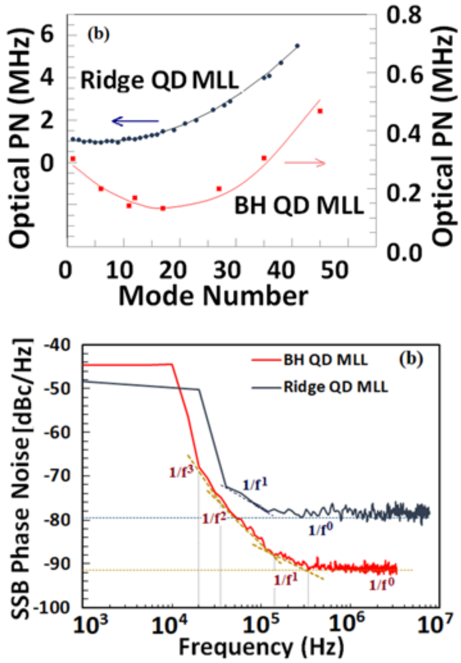

Fig. 6. Measured (a) optical phase noise vs. laser mode number, and (b) single side-band (SSB) phase noise spectrum obtained from a 25 GHz QD BH MLL in comparison with that from ridge QD MLL.

Table 1. Lists of Parabolic fitted results of the minimum optical linewidths.

Laser Structure	*Fit from Phase noise vs. Mode #*			*Pulsed Timing Jitter (fs)*	*Integrated Timing Jitter (ps)*
	$\Delta\upsilon_{nim}$ (MHz)	*n_{nim}*	*$\Delta\upsilon_{RF1}$ (kHz)*		
Ridge	0.968	5.6	3.57	6.03	1.90
BH	0.133	18.1	0.512	2.28	0.48

Lists of Parabolic fitted results of the minimum optical linewidths, i.e. minimum optical phase noise, $\Delta\upsilon_{nim}$, the minimum mode number n_{nim} and the first harmonic RF spectrum linewidth $\Delta\upsilon_{RF1}$ using Eq. (7) and estimated pulse-to pulse using Eq. (10) and integrated using Eq. (9) timing jitters for the 25 GHz QD F-P MLL with both buried heterostructure and surface ridge structures.

The minimum linewidths $\Delta\upsilon_{min}$ = 0.133 MHz and the first harmonic RF linewidths $\Delta\upsilon_{RF1}$ = 0.512 kHz are extracted for the lasers with BH structure, which are both about 7 times smaller than that obtained from the laser with surface ridge (SR) structure. The pulse to pulse timing jitter σ_{ptp} = 2.28 fs for the lasers with BH structure are estimated from $\Delta\upsilon_{RF1}$ using Eq. (10) as shown in Table 1, which is about 3 times lower than that of laser with SR structure. Furthermore, to investigate the integrated timing jitter performance, a SSB phase noise spectrum is calculated from measured RF PSD by Eq. (9) using a high speed IR photodetector and PXA signal analyzer (Keysight Technologies Model N9030A) at the settings of RBW = 10 kHz as shown in Fig. 6 (b) for the

25 GHz QD F-P MLLs in the both cases of BH and SR structures. The calculated integrated timing jitter of 1.90 and 0.48 ps are obtained for QD MLLs with SR and BH structures respectively. The integrated timing jitter is reduced about 4 times in the case of fabricated MLL with BH structure as compared with SR structure. From Fig. 6 (b), for the F-P QD MLL with BH structure, it is observed that the four typical noise types, flicker frequency modulation, white flicker frequency noise, flicker phase modulation and white phase noise, demonstrated predicted down tendency with slops of $1/f^3$, $1/f^2$, $1/f$ and $1/f^0$, respectively, as discussed in Section 2. However, for the F-P QD MLL with SR structure, the noise of flicker phase modulation is dominated and the flicker frequency modulation and white flicker frequency noises are covered by the white phase noise. The white phase noise of the F-P QD MLL with BH structure is 12 dB lower than that from the F-P QD MLL with SR structure. This is perhaps the reason that the performance of RIN, phase noise and timing jitter of laser with BH structure is much better than that with SR structure.

5. Application

There is a strong connection between the timing jitter of an OFC and the data bandwidth capability since the timing jitter is strongly related to the optical phase noise of each individual longitudinal mode. Both the modulation data rate and the number (N) of the higher-order data modulation format, i.e. PAM-N or N-QAM, are inversely proportional to the phase noise of each individual laser channel. If the phase noise or the timing jitter is smaller, a higher modulation data rate and a larger N can be achieved. The performance of InAs/InP QD F-P BH MLL is evaluated in system experiments by realizing photonics-assisted RoF wireless data transmission links in this study. The experimental setup comprised of central office (CO), remote ratio unit (RRU) and wireless receiver as shown in Fig. 7. More detailed information of the system setup is contained in [46]. In this experimental setup, a typical 5G fronthaul with centralized radio access network is emulated. Two optical channels (λ_1 and λ_2) from the OFC laser source are used, where λ_1 serves as a modulated data channel and λ_2 as an optical local oscillator (OLO) for remote heterodyne up-conversion. The remote optical heterodyne of the two optical channels up-converts the baseband data signal with Gigabit signal rate to the desired RF carrier signal in optical domain at the remote radio unit (RRU) without using any RF electrical LO.

In the CO, the C-band QD F-P MLL with BH structure is used as an optical source, which is biased at around 423 mA and maintained at 19 °C by using a high stable laser driving controller. The multi-wavelength output of QD BH MLL is connected to a 3 dB PM optical coupler (OC_1) through a two stage PM isolator, to avoid any back reflections caused by subsequent equipment, followed by two tunable optical band pass filters ($OBPF_1$ and $OBPF_2$) in each output of OC_1.

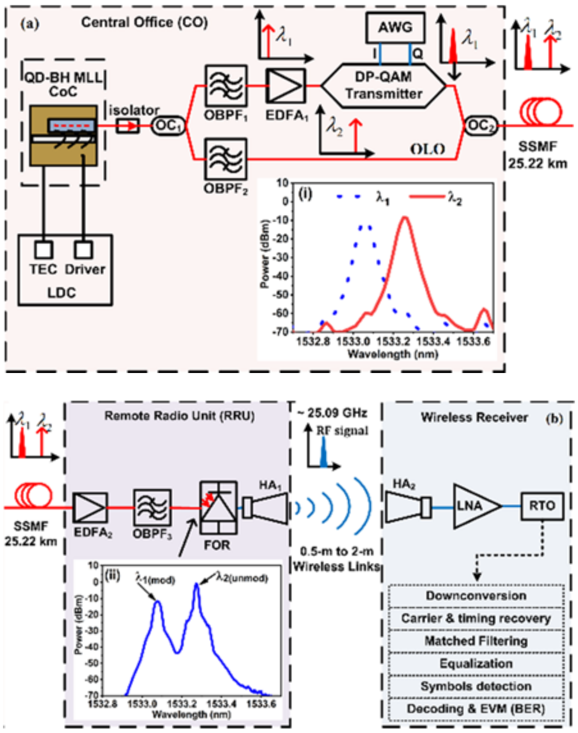

Fig. 7. Schematic of the experimental setups of Central Office (a) and Remote Radio Unit and Wireless Receiver (b) for photonics-assisted RoF RF signal generation, data transmission and detection using two optical channels (data channel λ_1 and optical LO λ_2) from an InAs/InP QD F-P MLL with BH structure. Where: OC = optical coupler; OBPF = optical band pass filter; EDFA = erbium-doped fiber amplifier; AWG = arbitrary waveform generator; OLO = optical local oscillator; FOR = fiber-optic receiver; HA = Horn antenna; LNA = low noise amplifier; RTO = real-time oscilloscope.

Two adjacent optical channels are select from the MLL by the two OBPFs; one for data transmission and another as an optical LO for photonic up-conversion at the RRU, spacing at the RF carrier frequency near to the center of the standard 3GPP 5G NR (a global standard for 5G wireless interface) frequency band n258 (24.25 to 27.5 GHz) of frequency range 2 (FR2). The wavelength of the two selected optical channels are at 1533.044 nm (λ_1) and 1533.240 nm (λ_2), respectively, which are filtered out from the free running optical comb spectrum obtained from the QD BH MLL cavity without using any controlled feedback locking mechanism. It is noteworthy that the QD MLL is a promising source since the selection of the optical channels is flexible and it can be used to generate RF signals in higher frequency bands of mm-wave spectrum including K-band, V-band, W-band and even THz range depending on the channels spacing selection. After boosting the power of optical data channel (λ_1) by an erbium-doped fiber amplifier

($EDFA_1$), it is modulated with 16-QAM digital baseband signals having a symbol rate of 4-GBaud by employing two channels of in-phase (I) and quadrature (Q) from a dual polarization (DP) QAM optical transmitter system (SHF 46215B DP-QAM). The two channels' baseband signals are generated electronically using an arbitrary waveform generator (AWG) (Keysight Technologies, Model M9502A) with a pseudo random binary sequence (PRBS) pattern of 2^{-11}-1 bits and a root raised cosine filter with roll-off factor of 0.35 is also applied for pulse shaping. The second optical channel (λ_2) is used as a supplementary channel to provide OLO for heterodyne RF carrier signal generation at the RRU. The modulated and unmodulated optical signals are then combined in a 3 dB OC_2 and transmitted over a 25 km SSMF to the RRU.

In the RRU, the received optical signal is amplified by $EDFA_2$ followed by $OBPF_3$ to filter out the effect of amplified spontaneous emission (ASE) noise and other optical components. These two optical signals are then beat together on a 38-GHz bandwidth fiber-optic receiver (FOR) (New Focus model 1474-A) to generate the 16 Gb/s (4-GBaud×16-QAM) modulated RF carrier signal at 25 GHz. The FOR is directly attached to a 17 dBi Horn antenna (WR-34) with a 20-33 GHz bandwidth that transmits the generated 4-GBaud RF data signal over 0.5 m to 2 m free-space indoor wireless distance. After wireless transmission, the RF signal is then received by another identical aligned Horn antenna and amplified by a low noise amplifier (LNA) before capturing into a real-time oscilloscope (RTO) for processing. The signal is captured and coherently detected in real-time by using a 33-GHz bandwidth and 100 GSa/s speed Tektronix DPO73304SX oscilloscope with vector signal analysis software (SignalVu). This process involves several digital signal processing (DSP) steps before the signal is demodulated, which include signal down conversion, carrier and symbol locking, RRC matched filtering to recover the baseband IQ data and to minimize inter-symbol interference (ISI), adaptive equalization to compensate for linear distortions, symbols detection and data decoding to calculate the error vector magnitude (EVM) and bit error rate (BER). Finally, the system performance is evaluated by analyzing EVM and BER of the received decoded 16-QAM 4-GBaud (16-Gb/s) data signals. The BER is calculated from the measured EVM values based on the EVM and BER relationship derived in [47].

The performance of EVM and BER is evaluated in a proof-of-concept end-to-end fiber-wireless integrated system experiment by generating, transmitting and detecting broadband RoF wireless signals in the downlink in real-time. The EVM and BER below the standard limit of 12.5 % [48] and FEC requirement of 3.8×10^{-3}, respectively, are successfully achieved in the photonics-assisted wireless system with remote frequency up-conversion and detection of 4-GBaud 16-QAM baseband data signals over 25 km SSMF and 0.5 m to 2 m free-space indoor wireless RF links. Fig. 8 (a) shows the calculated BER and measured EVM as a function of RF link distance at a fixed received optical power of around 2 dBm. It can be seen that for all the RoF wireless links, a BER of well below the standard FEC is achieved. Moreover, Fig. 8 (b) and Fig. 8 (c) shows the corresponding constellation and eye diagrams of the received 16-QAM data signals with the measured RMS EVM values of 6.62 %, 6.92 %, 7.72 % and 8.43 % for RF wireless link distance of 0.5 m, 1 m, 1.5 m and 2 m, respectively. In addition, Fig. 8 (c) shows the clear and open eye diagrams for the corresponding 4-Gbaud received signals for all of the RF wireless links. These results indicate that low noise monolithic integrated InAs/InP F-P QD BH MLL with broadband flat spectra having multiple highly coherent optical channels and ultra-low timing jitters described in this paper is a promising optical source for potential applications in high speed and high capacity 5G fiber-wireless integrated systems.

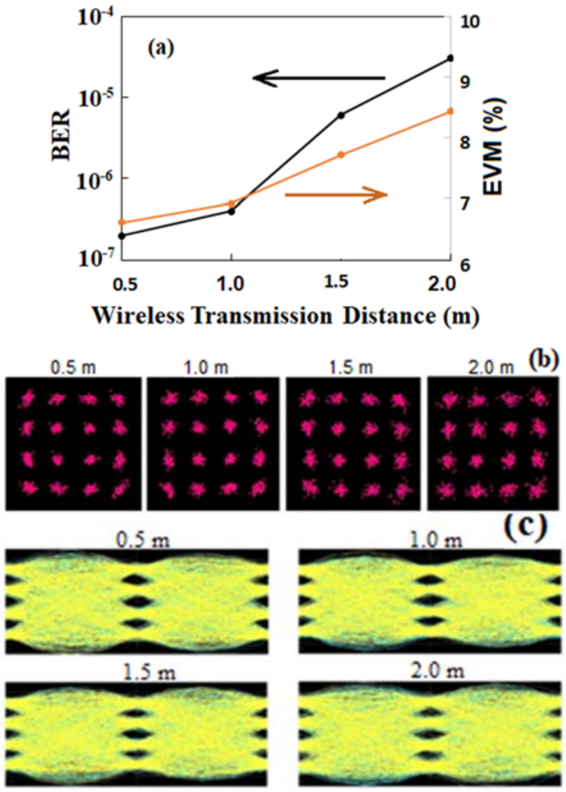

Fig. 8. Experimental transmission performance of the F-P QD BH MLL in photonics-assisted 16-Gb/s (4-Gbaud×16 QAM) wireless links at 25 GHz 5G NR over 0.5 m to 2 m RF link distance through 25 km SSMF (a) obtained BER (left axis) and EVM (right axis); (b) 16-QAM constellations and (c) corresponding eye diagrams observed for 4-Gbaud 16-QAM signals after 0.5 m, 1 m, 1.5 m and 2 m wireless links.

6. Conclusions

We have developed, experimentally characterized and demonstrated monolithically integrated 25 GHz C-band InAs/InP QD Febra-Perio mode-locked laser

(MLL) based optical frequency comb (OFC). Measured method of timing jitter is studied through a direct measurement of the first harmonic RF PSD using a fast photodiode and from optical phase noise measurements. The results from the two method are matched very well, while the optical method has an advantage of not limited by the speed of the photodetector and suitable for extremely high-speed OFC where a photodiode could be a limiting factor. Moreover, growth of InAs/InP QD gain materials and fabrications of F-P MLL with buried heterostructure (BH) waveguides are described. The laser performance is evaluated and compared with the laser with conventional ridge waveguide. An low integrated average RIN value (-143.3 dB/Hz) is achieved for a filtered individual channel of the QD BH MLL, which is about 6 dB lower than that of the QD MLL with ridge structure. Optical phase noise less than 466 kHz is achieved over the comb wavelength range and it is at least 10 times lower than the measured results of a QD MLL with ridge structure. Moreover, pulse to pulse timing jitter values of 2.28 fs is achieved for the QD BH MLL, which is about 3 times lower than that obtained for the laser with ridge structure. Furthermore, by investigating its integrated timing jitter performance from the single side band phase noise spectrum, the levels of flicker phase modulation noise and the white phase noise are all about 12 dB lower than that with surface ridge structure. This could be the possible reason that the performance of laser with BH structure are much better than that with surface ridge structure. In addition, by using the QDash BH MLL, we have successfully demonstrated 16-Gb/s (4-GBaud×16-QAM) RoF-based optical heterodyne RF wireless signal delivery at 25 GHz with a total of 25 km SSMF and up to 2 m wireless links achieving EVM and BER well below the standard requirements. The results indicate that monolithically integrated semiconductor InAs/InP QDash BH MLL with simple and compact design providing large number of highly correlated optical channels with low noise and high power performance can be a cost-efficient and promising solution for high capacity and high speed RoF-based fronthaul systems of 5G and beyond wireless networks.

Acknowledgements

The authors would like to acknowledge supports from National Challenge Program "High Throughput and Secure Networks (HTSN)" in National Research Council (NRC) Canada.

References

[1]. Y. Kim, H. Lee, P. Hwang, R. Patro, J. Lee, W. Roh, K. Cheun, Feasibility of Mobile Cellular Communications at Millimeter Wave Frequency, in *IEEE Journal of Selected Topics in Signal Processing*, Vol. 10, Issue 3, April 2016, pp. 589-599.

[2]. R. Proietti, *et al.*, Elastic optical networking by dynamic optical arbitrary waveform generation and measurement, *Journal of Optical Communications and Networking*, Vol. 8, Issue 7, July 2016, pp. A171-A179.

[3]. Juned N. Kemal, Joerg Pfeifle, Pablo Marin-Palomo, M. Deseada Gutierrez Pascual, Stefan Wolf, Frank Smyth, Wolfgang Freude, Christian Koos, Multi-wavelength coherent transmission using an optical frequency comb as a local oscillator, *Opt. Express*, Vol. 24, Issue 22, 2016, pp. 25432-25445.

[4]. Cosimo Calo, Quantum dot based mode locked lasers for optical frequency combs. Networking and Internet Architecture, *Institut National des Télécommunications*, 2014.

[5]. F. Lelarge, B. Dagens, J. Renaudier, R. Brenot, A. Accard, F. van Dijk, D. Make, O. Le Gouezigou, J. G. Provost, F. Poingt, J. Landreau, O. Drisse, E. Derouin, B. Rousseau, F. Pommereau, G. H. Duan, Recent advances on InAs/InP quantum dash based semiconductor lasers and optical amplifiers operating at 1.55 µm, *IEEE Journal of Selected Topics in Quantum Electronics*, Vol. 13, Issue 1, 2007, pp. 111–124.

[6]. R. Rosales, K. Merghem, C. Calo, G. Bouwmans, I. Krestnikov, A. Martinez, A. Ramdane, Optical pulse generation in single section InAs/GaAs quantum dot edge emitting lasers under continuous wave operation, *Applied Physics Letters*, Vol. 101, Issue 22, 2012, 221113.

[7]. P. Bardella, L. L. Columbo, M. Gioannini, Self-generation of optical frequency comb in single section quantum dot Fabry-Perot lasers: a theoretical study, *Opt. Express*, Vol. 25, Issue 21, 2017, pp. 26234-26252.

[8]. W. W. Chow, S. Liu, Z. Zhang, J. E. Bowers, M. Sargent III, Multimode description of self-mode locking in a single-section quantum-dot laser, *Opt. Express*, Vol. 28, Issue 4, 2020, pp. 5317-5330.

[9]. D. Arsenijevi´c, M. Kleinert, D. Bimberg, Breakthroughs in photonics 2013: Passive mode-locking of quantum-dot lasers, *IEEE Photon. J.,* Vol. 6, Issue 2, Apr. 2014, Art. No. 0700306.

[10]. K. Merghem, A. Akrout, A. Martinez, G. Aubin, A. Ramdane, F. Lelarge, G. Duan, Pulse generation at 346 GHz using a passively mode locked quantum-dash-based laser at 1.55 µm, *Appl. Phys. Lett.*, Vol. 94, Issue 2, 2009, 021107.

[11]. D. Eliyahu, R. A. Salvatore, A. Yariv, Noise characterization of a pulse train generated by actively mode-locked lasers, *J. Opt. Soc. Amer. B*, Vol. 13, Issue 7, 1996, pp. 1619-1626.

[12]. Fiol G., Arsenijević D., Bimberg D., Vladimirov A. G., Wolfrum M., Viktorov E. A., Mandel P., Hybrid mode-locking in a 40 GHz monolithic quantum dot laser, *Appl. Phy. Lett.*, Vol. 96, Issue 1, 2010, 011104.

[13]. Arkhipov R., Pimenov A., Radziunas M., Rachinskii D., Vladimirov A. G., Arsenijević D., Bimberg D., Hybrid mode locking in semiconductor lasers: simulations, analysis, and experiments, *IEEE J. Quantum Electron.*, Vol. 19, Issue 4, 2013, pp. 1100208-1100208.

[14]. Habruseva T., Arsenijević D., Kleinert M., Bimberg D., Huyet G., Hegarty S. P., Optimum phase noise reduction and repetition rate tuning in quantum-dot mode-locked lasers, *Appl. Phy. Lett.*, Vol. 104, Issue 2, 2014, 021112.

[15]. Arkhipov R. M., Habruseva T., Pimenov A., Radziunas M., Hegarty S. P., Huyet G., Vladimirov A.

G, Semiconductor mode-locked lasers with coherent dual-mode optical injection: simulations, analysis, and experiment, *JOSA B*, Vol. 33, Issue 3, 2016, pp. 351-359.

[16]. Fiol G., Kleinert M., Arsenijević D., Bimberg D., 1.3 µm range 40 GHz quantum-dot mode-locked laser under external continuous wave light injection or optical feedback, *Semicond. Sci. Technol.,* Vol. 26, 2011, 014006.

[17]. Otto C., Lüdge K., Vladimirov A. G., Wolfrum M., Schöll E., Delay-induced dynamics and jitter reduction of passively mode-locked semiconductor lasers subject to optical feedback, *New Journal of Physics,* Vol. 14, Issue 11, 2012, 113033.

[18]. Jaurigue L., Pimenov A., Rachinskii D., Schöll E., Lüdge K., Vladimirov A. G., Timing jitter of passively-mode-locked semiconductor lasers subject to optical feedback: A semi-analytic approach, *Physical Review A,* Vol. 92, Issue 5, 2015, 053807.

[19]. Nikiforov O., Jaurigue L., Drzewietzki L., Lüdge K., Breuer S., Experimental demonstration of change of dynamical properties of a passively mode-locked semiconductor laser subject to dual optical feedback by dual full delay-range tuning, *Optics Express,* Vol. 24, Issue 13, 2016, pp. 14301-14310.

[20]. Aubin G., Brenot R., Calo C., Freude W., Kemal J., Koos C., Lelarge F., Marin-Palomo P., Merghem K., Ramdane A., Randel S., 32QAM WDM transmission using a Quantum-Dash Passively Mode-Locked Laser with resonant feedback, *Optical Fiber Communication Conference Postdeadline Papers*, Th5C.3, 2017.

[21]. Arsenijević D., Kleinert M., Bimberg D., Phase noise and jitter reduction by optical feedback on passively mode-locked quantum-dot lasers, *Applied Physics Letters,* Vol. 103, Issue 23, 2013, 231101.

[22]. Z. G. Lu, J. R. Liu, S. Raymond, P. J. Poole, P. J. Barrios, D. Poitras, 312-fs pulse generation from a passive C-band InAs/InP quantum dot mode-locked laser, *Optics Express*, Vol. 16, 2008, pp. 10835-10840.

[23]. J. R. Liu, Z. G. Lu, S. Raymond, P. J. Poole, P. J. Barrios, G. Pakulski, D. Poitras, G. Z. Xiao, Z. Y. Zhang, Uniform 90-channel multiwavelength InAs/InGaAsP quantum dot laser, *Electron. Lett.*, Vol. 43, 2007, pp. 458-460.

[24]. J. R. Liu, Z. G. Lu, S. Raymond, P. J. Poole, P. J. Barrios, D. Poitras, Dual-wavelength 92.5 GHz self-mode-locked InP-based quantum dot laser, *Optics Letters*, Vol. 33, 2008, pp. 1702-1704.

[25]. Z. G. Lu, J. R. Liu, P. J. Poole, S. Raymond, P. J. Barrios, D. Poitras, G. Pakulski, P. Grant, D. Roy-Guay, An L-band monolithic InAs/InP quantum dot mode-locked laser with femtosecond pulses, *Optics Express*, Vol. 17, 2009, pp. 13609–13614.

[26]. Z. G. Lu, J. R. Liu, P. J. Poole, Z. J. Jiao, P. J. Barrios, D. Poitras, J. Caballero, X. P. Zhang, Ultra-high repetition rate InAs/InP quantum dot mode-locked lasers, *Optics Communications*, Vol. 284, 2011, pp. 2323-2326.

[27]. Z. J. Jiao, J. R. Liu, Z. G. Lu, X. P. Zhang, P. J. Poole, P. J. Barrios, D. Poitras, A C-Band InAs/InP Quantum Dot Semiconductor Mode-Locked Laser Emitting 403-GHz Repetition Rate Pulses, *IEEE Photonics Technol. Lett.*, Vol. 23, Issue 9, 2011, pp. 543-545.

[28]. Z. G. Lu, J. R. Liu, P. J. Poole, C. Y. Song, J. Weber, L. Mao, S. D. Chang, H. P. Ding, P. J. Barrios, D. Poitras S. Janz, Integrated InAs/InP quantum-dot coherence comb lasers, in *Proc. SPIE Photonics West*, San Francisco, CA, USA, 2017, pp. 10107-10118.

[29]. Z. G. Lu, J. R. Liu, C. Y. Song, J. Weber, Y. Mao, S. D. Chang, H. P. Ding, P. J. Poole, P. J. Barrios, D. Poitras, S. Janz, M. O'Sullivan, High performance InAs/InP quantum dot 34.462-GHz C-band coherent comb laser module, *Opt. Express*, Vol. 26, Issue 2, 2018, pp. 2160-2167.

[30]. Z. G. Lu, J. R. Liu, P. J. Poole, Y. Mao, J. Weber, G. C. Liu, P. Barrio, InAs/InP Quantum Dash Semiconductor Coherent Comb Lasers and their Applications in Optical Networks, *Journal of Lightwave Technology*, Vol. 39, Issue 12, 2021, pp. 3751-3760.

[31]. Lu Z. G., Liu J. R., Poole P. J., Song C. Y., Chang S. D., Ultra-narrow linewidth quantum dot coherent comb lasers with self-injection feedback locking, *Optics Express,* Vol. 26, Issue 9, 2018, pp. 11909-11914.

[32]. Y. Mao, J. Liu, Z. Lu, C. Song, P. J. Poole, Ultra-low Timing Jitter of Quantum Dash Semiconductor Comb Lasers with Self-injection Feedback Locking, *IEEE J. of Select. Topics in Quantum Electronics*, Vol. 25, Issue 6, Nov. 2019, 1900607.

[33]. Y. Mao, Z. G. Lu, J. R. Liu, P. J. Poole, G. C. Liu, Pulse Timing Jitter Estimated From Optical Phase Noise In Mode-lock Semiconductor Quantum Dash Lasers, *J. of Lightwave Technology*, Vol. 38, Issue 17, 2020, pp. 4787-4793.

[34]. Y. Mao, K. Zeb, Z. G. Lu, J. R. Liu, E. Liu, P. Poole, M. Rahim, G. Pakulski, P. Barrios, W. Jiang, X. Zhang, Study of Phase Noise and Timing Jitter in InAs/InP Quantum Dash Mode-locked Lasers for Application in 5G RoF Wireless Networks, in *Proc. of the 4th International Conference on Optics, Photonics and Lasers (OPAL'2021)*, Corfu, Greece, 13-15 October 2021, pp. 33-35.

[35]. Y. Takushima, H. Sotobayashi, M. E. Grein, E. P. Ippen, H. A. Haus, Linewidth of mode combs of passively and actively mode-locked semiconductor laser diodes, *Proc. of SPIE*, Vol. 5595, 2004, pp. 213–227.

[36]. T. Habruseva, S. O'Donoghue, N. Rebrova, F. Kéfélian, S. P. Hegarty, G. Huyet, Optical linewidth of a passively mode-locked semiconductor laser, *Opt. Lett.,* Vol. 34, Issue 21, 2009, pp. 3307-3309.

[37]. J. P. Tourrenc, A. Akrout, K. Merghem, A. Martinez, F. Lelarge, A. Shen, G. H. Duan, A. Ramdane, Experimental investigation of the timing jitter in self-pulsating quantum-dash lasers operating at 1.55 µm, *Opt. Express*, Vol. 16, Issue 22, 2008, pp. 17706–17713.

[38]. F. X. Kärtner, U. Morgner, T. Schibli, R. Ell, H. A. Haus, J. G. Fujimoto, E. P. Ippen, Few-cycle pulses directly from a laser, *Top. Appl. Phys*., Vol. 95, 2004, pp. 73-136.

[39]. R. Rosales, K. Merghem, A. Martinez, F. Lelarge, A.Accard, A. Ramdane, Timing jitter from the optical spectrum in semiconductor passively mode locked lasers, *Optics Express*, Vol. 20, Issue 8, 2012, pp. 9151-9160.

[40]. D. von der Linde, Characterization of the noise in continuously operating modelocked lasers, *Appl. Phys. B*, Vol. 39, Issue 4, 1986, pp. 201–217.

[41]. F. Kefelian, S. O'Donoghue, M. T. Todaro, J. G. McInerney, G. Huyet, RF linewidth in monolithic passively mode-locked semiconductor laser, *IEEE Photon. Technol. Lett.*, Vol. 20, Issue 16, 2008, pp. 1405–140.

[42]. L. Drzewietzki, S. Breuer, W. Elsaßer, Timing jitter reduction of passively mode-locked semiconductor

lasers by self- and external-injection: Numerical description and experiments, *Opt. Express*, Vol. 21, Issue 13, 2013, pp. 16142–1616.

[43]. S. Latkowski, Radio frequency and terahertz signals generated by passively modelocked semiconductor lasers, PhD Dissertation, *Dublin City University,* Dublin, Ireland, 2010.

[44]. P. J. Poole, K. Kaminska, P. Barrios, Z. G. Lu, J. R. Liu, Growth of InAs/InP-based quantum dots for 1.55 µm laser applications, *J. Cryst. Growth*, Vol. 311, Issue 6, 2009, pp. 1482-1486.

[45]. Y. Ben M'Sallem, *et al*., Quantum-Dash Mode-Locked Laser as a Source for 56-Gb/s DQPSK Modulation in WDM Multicast Applications, in *IEEE Photonics Technology Letters*, Vol. 23, Issue 7, 2011, pp. 453-455.

[46]. K. Zeb, Z. G. Lu, J. R. Liu, Y. Mao, G. C. Liu, P. J. Poole, M. Rahim, G. Pakulski, P. Barrios, W. Jiang, J. Zhang, InAs/InP quantum dash buried heterostructure mode-locked laser for High Capacity Fiber-wireless Integrated 5G New Radio Fronthaul Systems, *Optics Express*, Vol. 29, Issue 11, 2021, pp. 16164-16174.

[47]. R. Schmogrow, B. Nebendahl, M. Winter, A. Jopstern, D. Hillerkuss, S. Koenig, J. Meyer, M. Dreschmann, H. Huebner, C. Koos, J. Becker, W. Freude, J. Leuthold, Error vector magnitude as a performance measure for advanced modulation formats, *IEEE Photon. Technol. Lett*., Vol. 24, Issue 1, 2012, pp. 61–63.

[48]. ETSI TS 138.101-2 V15.3.0, User equipment (UE) radio transmission and reception, Tech. Rep., Part 2: Range 2 standalone, (3GPP TS 38.101-2 V15.3.0 Release 15), 2018.

Sensors & Transducers, Vol. 255, Issue 1, January 2022, pp. 35-43

Sensors & Transducers

Published by IFSA Publishing, S. L., 2022
http://www.sensorsportal.com

Lock-in Phenomena in a Ring Laser

*** Aleksei ZADVORKIN and Tatiana RADINA**
St. Petersburg State University, Ulyanovskaya 1, 198504, Petergof, St. Petersburg, Russia
* Tel.: +7-911-0314984
E-mail: zlelik2000@gmail.com

Received: 4 December 2021 /Accepted: 7 January 2022 /Published: 31 January 2022

Abstract: The problem of synchronizing counterpropagating waves in ring lasers is an integral part of the fundamental problem of synchronizing nonlinear oscillations. This phenomenon is inherent in all self-oscillating systems. As a continuation of the work [1] and extension of [2], an in-depth analysis of the obtained equations was performed for He Ne ring laser with an inhomogeneously broadened active medium. Alternative to backscattering explanation of the lock-in phenomena [3] was suggested and it is counterpropagating waves phase relationship through their nonlinear polarization. Comparative analysis of the behavior of frequencies and intensities for the single-mode ring laser working on a single isotope of Ne and on the mix of ^{20}Ne ^{22}Ne isotopes was conducted. Dependency of the lock-in threshold on different parameters including active medium pressure, cavity detuning, pumping current value, rotation speed, etc. were theoretically researched. The intensity of counterpropagating waves was analyzed. Theoretical predictions were compared with experimental data. The most important results are presented in this work.

Keywords: Ring laser, Nonlinear coupling, Frequency synchronization, Gyroscope.

1. Introduction

The creation of a ring laser has created a unique possibility for conducting precision research in various fields of fundamental physics. For example, the creation of detectors of gravitational waves [4], the study of relativistic and gravitational effects in the theory of relativity [5, 6] verification of the effects of quantum electrodynamics [4], and other phenomena [7]. One of the important applications of the ring laser is a laser gyroscope sensor. The accuracy of modern gyroscopes makes it possible to measure the unevenness of the Earth's rotation [7].

The principle of operation of this equipment is based on the Sagnac effect. Two counterpropagating waves in the ring laser have different frequencies if the propagation conditions of the waves are different. One of these conditions can be the rotation of the ring laser. Frequency differences can be easily measured by optical heterodyne detection.

Ring lasers are complex nonlinear self-oscillating systems with output characteristics, which (and, hence, the accuracy of measurements) are dependent on many factors. In essence, the problem of finding the frequencies and intensities of the generation of counterpropagating waves of the same mode is the problem of finding normal modes of an optical resonator with a nonlinear active medium. The presence of a nonlinear medium in the resonator dictates the use of the self-consistent method, first used by Lamb [8] for the construction of laser theory.

The obtained results, for the first time, made it possible to explain the behavior of the frequency differences and intensities of laser generation in single-mode gas laser operating on pure isotope, in the entire generation region (including the region of strong coupling). In addition, they made it possible to systematize the experimental data accumulated in the course of many years of research, to establish the regularities of the redistribution of the intensities of the generation of counterpropagating waves depending on the parameters of the resonator and the active medium.

During the rotation of the laser gyroscope at a speed less than a certain critical value (called the lock-in threshold), the frequency difference of counterpropagating waves is insignificant, and reciprocal frequency synchronization is observed [9], which leads to the insensitivity of the laser gyroscope in a certain region of low rotation speeds, where the beat frequency becomes equal to zero. A large number of works [9 - 10] are devoted to the study of the synchronization phenomenon in ring gas lasers. The main, and often the single reason for the reciprocal frequency synchronization is considered to be the coupling of waves through backscattering when part of the field of one wave is scattered by a single inhomogeneity in the direction of the other. This model does not find sufficient physical justification.

In the work [1], another, fundamentally unavoidable, reason for the coupling of counterpropagating waves was proposed. This is a phase relationship through their nonlinear polarization. More precisely, through that component of polarization, the origin of which is caused by the modulation of the population difference between the energy levels with frequency $\omega_r - \omega_l$. Where ω_r is the frequency of the right wave and ω_l is the frequency of the left wave. We note that the modulation of the population difference is the reason for the existence of the strong-coupling region.

This work is an extension of [1]. Here we conducted a comparative analysis of the behavior of frequencies and intensities of single-mode lasers operating on pure isotope Ne and the mixture ^{20}Ne ^{22}Ne isotopes. Note that the transition to a two isotopic medium does not affect the general form of the laser equations. Only the expressions for the polarization coefficients change.

2. Main Equations

The self-consistent problem of an optical ring resonator with a nonlinear active medium was solved. The electric field of counterpropagating waves ($j = r, l$) is defined as:

$$E_j(z,t) = E_{0j} exp\left\{\pm ik\int_0^z n_j(\tilde{z})d\tilde{z} - i\omega t \mp \frac{\varphi(t)}{2}\right\}, \quad (1)$$

where $\frac{\varphi(t)}{2}$ are the phase shifts of each wave caused by rotation.

The complex refractive index $n_j(z) = n'_j(z) + in''_j(z)$ of a nonlinear medium is induced by the interaction of counterpropagating waves in the active medium. $n_j(z)$ was found via polarization by a quantum mechanical method suggest by Lamb [8]. Unlike [8] and other authors, all calculation was performed in complex variables, in the analytical form in the third-order of the perturbation theory with the weak-field limit without additional approximations.

The final system of the equations is obtained from the periodicity conditions which are necessary for the existence of stationary generation in the resonator:

$$\eta_r = \beta''_r I_r + \theta''_l I_l + (\sigma''_r cos\varphi - \sigma'_r sin\varphi)\sqrt{I_r I_l}, \quad (2)$$

$$\eta_l = \beta''_l I_l + \theta''_r I_r + (\sigma''_l cos\varphi + \sigma'_l sin\varphi)\sqrt{I_r I_l}, \quad (3)$$

$$\dot{\varphi} = \Delta\omega - \frac{c}{L}KH\{2 \vartriangle Z' - I_r(\beta'_r - \theta'_r) + I_l(\beta'_l - \theta'_l) - 2(\vartriangle \sigma' cos\varphi - \sigma'' sin\varphi)\sqrt{I_r I_l}\}, \quad (4)$$

where $I_{r,l}$ is the dimensionless intensities, $\eta_j = Z''_j - \frac{\varepsilon_j}{KH}$, $\beta_{r,l}$, $\theta_{r,l}$ are the polarization coefficient of self-saturation and cross-saturation respectively of right and left waves, Z' is the linear dispersion, Z' is the coefficient of linear gain, KH is the gain on the length of the tube H. The phase coupling of counterpropagating waves is caused by the parametric effects (polarization terms proportional to $\sigma''_{r,l}, \sigma'_{r,l}$) in a nonlinear active medium. The interaction of counterpropagating waves is carried out in a nonlinear active medium.

Imaginary and real parts of the $\beta_{r,l}$, $\theta_{r,l}$, Z $\sigma_{r,l}$ are shown in the Fig. 1 and Fig. 2 below.

Polarization coefficient σ, which is the only reason for frequency synchronization is 5 orders of magnitude smaller than other polarization coefficients ($\beta_{r,l}$, $\theta_{r,l}$, Z). This insignificant value is enough to change the behavior of the frequencies of counterpropagating waves and introduce lock-in phenomena.

Solving system (2) - (4) gives classical Adler's equation.

$$\dot{\varphi} = \Delta\widetilde{\omega} - Bsin\varphi \quad (5)$$

It can be used to derive boundaries of the lock-in range and the expressions for intensities:

$$\Delta\omega_d - B < \dot{\varphi} < \Delta\omega_d + B, \quad (6)$$

where

$$B = \frac{c}{L}\frac{2(KHZ'' - \varepsilon)}{\beta'' + \theta''}\left\{\sigma'' - \sigma'\frac{\beta' - \theta'}{\beta'' - \theta''}\right\} \quad (7)$$

$$\Delta\widetilde{\omega} = \Delta\omega + \Delta\omega_d, \Delta\omega_d = 2\Delta\varepsilon\frac{c}{L}\frac{\beta' - \theta'}{\beta'' - \theta''} \quad (8)$$

Here $\Delta\omega_d$ is the laser gyroscope null shift caused by a nonreciprocal element.

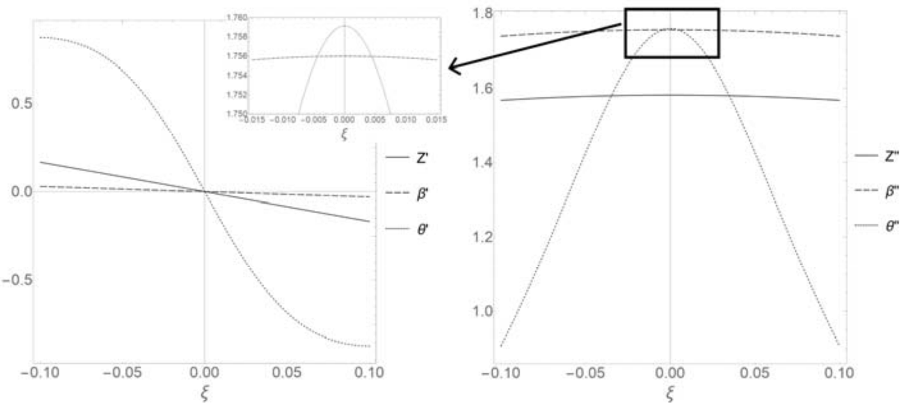

Fig. 1. Real part (on the left) and imaginary part (on the right) of polarization coefficients β, θ and Z depending on the relative detuning for zero frequency difference between counterpropagating waves and single isotope active medium.

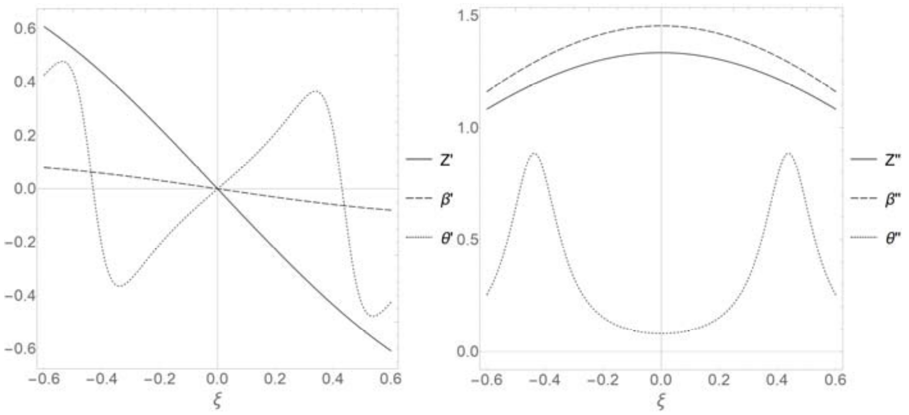

Fig. 2. Real part (on the left) and imaginary part (on the right) of polarization coefficients β, θ and Z depending on the relative detuning for zero frequency difference between counterpropagating waves and 50 % mixture of ^{20}Ne, ^{22}Ne isotopes active medium.

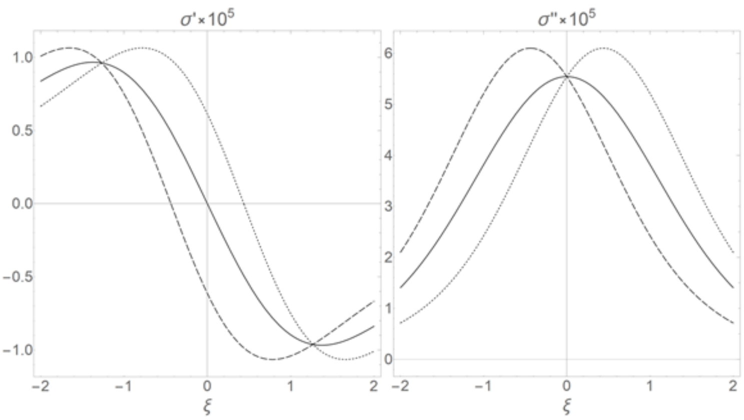

Fig. 3. Real part (on the left) and imaginary part (on the right) of polarization coefficient σ depending on the relative detuning for zero frequency difference between counterpropagating waves. Dashed lines are for single isotope and solid line for 50 % mixture of ^{20}Ne, ^{22}Ne isotopes active medium.

Intensities can be derived in the approximation $\Delta I \ll I$ using the notation $2I = I_r + I_l$, $2\Delta I = I_r - I_l$. In this case, $\Delta I/I$ can be neglected and the expression $\sqrt{I_r I_l}$ can be simplified as $\sqrt{I_r I_l} = I$.

$$I_{r,l} = I \pm \Delta I \tag{9}$$

$$I = \frac{\eta}{\beta'' + \theta''} \tag{10}$$

$$\Delta I = \frac{1}{\beta'' - \theta''}\left\{\Delta\eta + \eta\frac{\sigma' sin\varphi}{\beta'' + \theta''}\right\} \tag{11}$$

3. Discussion of the Numerical Calculation Results

Lock-in boundaries and intensity were researched theoretically based on Eqs. (2) - (4) for the wide range of ring laser configuration such as single isotope and mixture of ^{20}Ne, ^{22}Ne isotopes and by varying a significant number of different parameters including pressure in the active medium, gain value, detuning, resonator rotation speed, same and different losses for counterpropagating waves, etc. Based on Eqs. (9) - (11) calculations of intensities and additional frequencies difference were performed. The results for a single isotope and different losses or frequency difference are presented in Fig. 4, Fig. 5.

In case when frequency difference and different losses for counterpropagating waves are presented at the same time, the function of intensities becomes asymmetric. This special situation is presented in Fig. 6 and was noted in many experimental works.

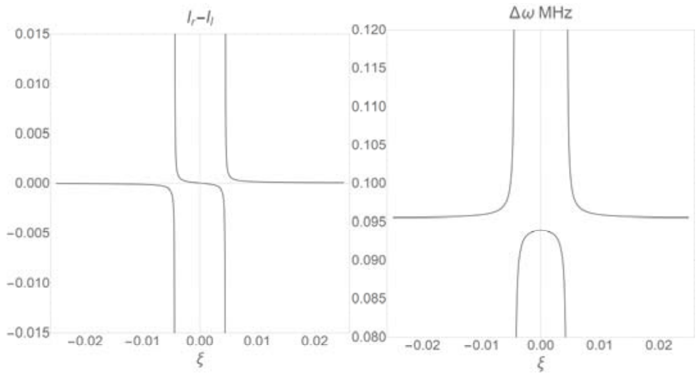

Fig. 4. Intensities difference for counterpropagating waves $I_r - I_l$ on the left and additional frequency difference for counterpropagating waves $\omega_r - \omega_l$ on the right depending on the relative detuning for non-zero frequency difference $\Delta\omega = 0.106\ MHz$, $\varepsilon_r = \varepsilon_l = 0.1$, $KH = 0.12$ and single isotope active medium.

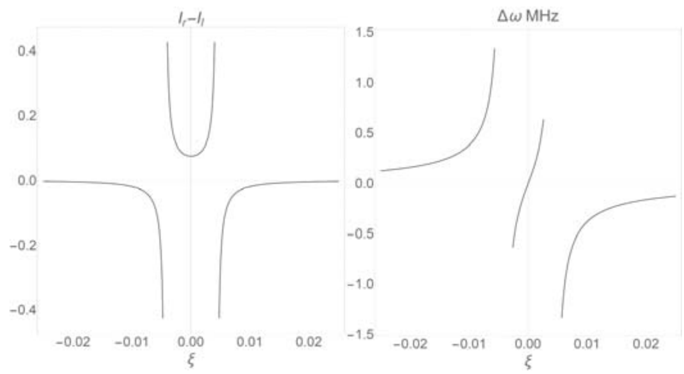

Fig. 5. Intensities difference for counterpropagating waves $I_r - I_l$ on the left and additional frequency difference for counterpropagating waves $\omega_r - \omega_l$ on the right depending on the relative detuning for different losses and zero frequency difference $\Delta\omega = 0\ MHz$, $\varepsilon_r = 0.1$, $\varepsilon_l = 0.1001$, $KH = 0.12$ and single isotope active medium.

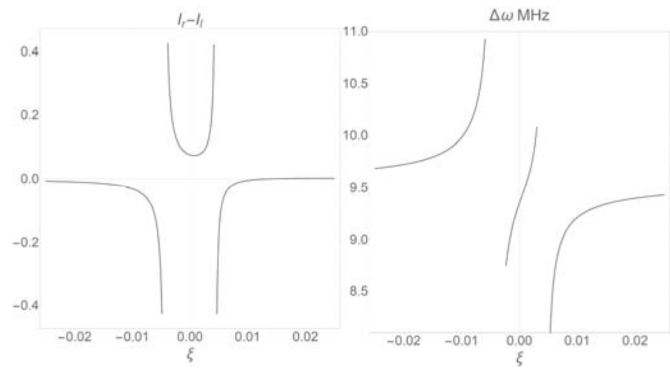

Fig. 6. Intensities difference for counterpropagating waves $I_r - I_l$ on the left and additional frequency difference for counterpropagating waves $\omega_r - \omega_l$ on the right depending on the relative detuning for different losses and none-zero frequency difference $\Delta\omega = 10.6\ MHz$, $\varepsilon_r = 0.1$, $\varepsilon_l = 0.1001$, $KH = 0.12$ and single isotope active medium.

The results for a mixture of ^{20}Ne, ^{22}Ne isotopes can be found in Fig. 7, Fig. 8. Similar to a single isotope active medium, for simultaneous presence of frequency difference and different losses for counterpropagating waves, functions of intensity and frequency difference become asymmetric as shown in Fig. 9.

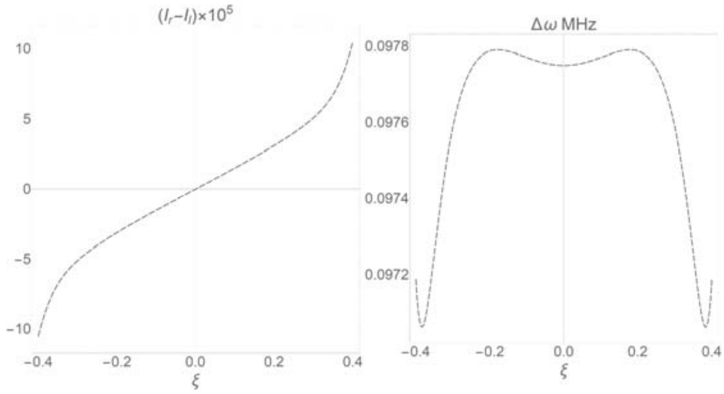

Fig. 7. Intensities difference for counterpropagating waves $I_r - I_l$ on the left and additional frequency difference for counterpropagating waves $\omega_r - \omega_l$ on the right depending on the relative detuning for non-zero frequency difference for $\Delta\omega = 0.106\ MHz$, $\varepsilon_r = \varepsilon_l = 0.1$, $KH = 0.12$ and 50 % mixture of ^{20}Ne, ^{22}Ne isotopes active medium.

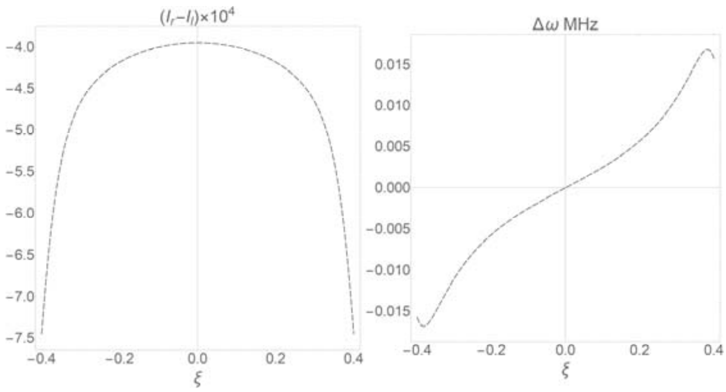

Fig. 8. Intensities difference for counterpropagating waves $I_r - I_l$ on the left and additional frequency difference for counterpropagating waves $\omega_r - \omega_l$ on the right depending on the relative detuning for different losses and zero frequency difference for $\Delta\omega = 0\ MHz$, $\varepsilon_r = 0.1$, $\varepsilon_l = 0.1001$, $KH = 0.12$ and 50 % mixture of ^{20}Ne, ^{22}Ne isotopes active medium.

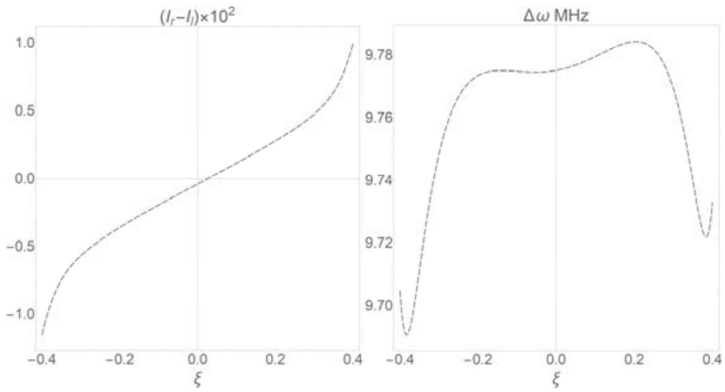

Fig. 9. Intensities difference for counterpropagating waves $I_r - I_l$ on the left and additional frequency difference for counterpropagating waves $\omega_r - \omega_l$ on the right depending on the relative detuning for different losses and non-zero frequency difference for $\Delta\omega = 10.6\ MHz$, $\varepsilon_r = 0.1$, $\varepsilon_l = 0.1001$, $KH = 0.12$ and 50 % mixture of ^{20}Ne, ^{22}Ne isotopes active medium.

As shown in Fig. 4 for a single isotope active medium there is an area of strong coupling of the waves. In this range of relative detuning, energy is redistributed between the weak and the strong waves and intensities for counterpropagating waves have corresponding peaks. However, the total intensity does not have these peaks. In addition, it was noted, that in the middle of the gain curve ΔI is zero.

Analysis of Eq. (11) for intensities difference inside lock-in range ($\Delta\omega = 0$) shows that ΔI is an odd function due to the fact that σ' is an odd function. Outside lock-in range ΔI is the odd function as well. ΔI close to the center of the gain curve has the same behavior inside and outside lock-in range as shown in Fig. 4 and Fig. 10. The detailed research of the behavior of σ' and σ'' was conducted in [1] and in Fig. 3 of that work. The presence of $sin\varphi$ in the Eq. (11) explains the intensity oscillations reported in [11] and other experimental works, which could not be theoretically justified before.

B in Eq. (7) makes the main contribution into synchronization threshold as follows from (5). As shown in Fig. 11, B is an even function because functions $Z'', \beta'', \theta'', \sigma''$ in Eq. (7) are even functions. The evenness of $Z'', \beta'', \theta'', \sigma''$ was discussed in [1] and shown in Fig. 1 and Fig. 2. B has a maximum on the center of the gain curve.

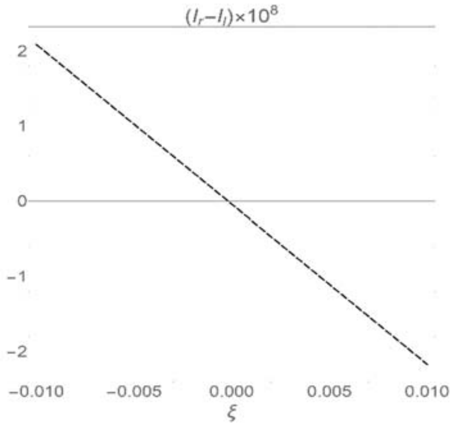

Fig. 10. Intensities difference for counterpropagating waves $I_r - I_l$ on the relative detuning inside lock-in region for $\Delta\omega = 0$, $\varepsilon_r = \varepsilon_l = 0.1$, $KH = 0.12$ and 50 % mixture of ^{20}Ne, ^{22}Ne isotopes active medium.

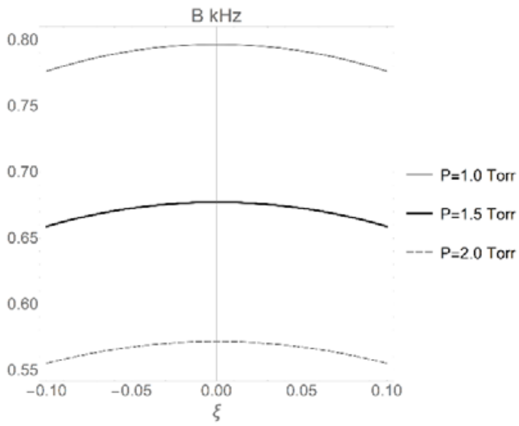

Fig. 11. Dependency of parameter $\boldsymbol{B}$ on the relative detuning for different pressure in the active medium for $\boldsymbol{\varepsilon_r = \varepsilon_l = 0.1}$, $\boldsymbol{KH = 0.12}$ and 50 % mixture of ^{20}Ne, ^{22}Ne isotopes active medium.

Fig. 12 shows the calculations of the intensity depending on resonator rotation speed for different gain. The lines for intensities on Fig. 12 are interrupted at the point of the lock-in threshold, which means the lock-in threshold is increasing with the increase of active medium gain. The explanation can be given from the fact, that frequency synchronization is a non-linear effect and nonlinearity increases with the increase of the active medium gain. On another side, as shown in Fig. 11, the lock-in threshold decreases with increasing of the active medium pressure. This is due to the raise of the relaxation constants with the pressure growths. It can be noted that frequency synchronization effect is complex, nonlinear effect and many different parameters can influence lock-in threshold, such as active medium pressure, gain, pumping current, etc.

Calculations for Fig. 12 were carried out under the condition that the gain K remains unchanged over the cross-section of the tube. However, in the experiments, the transverse distribution of the gain changes significantly with the increasing of the pumping current as shown in Fig. 13. This effect can lead to the reduction of the active medium gain with the increasing of pumping current due to the dependency of relaxation constants on this current. In our opinion, that is the reason for the deviation of Fig. 12 and similar figures in [3].

β_j, θ_j and respectively synchronization threshold depend on the active medium pressure and gain, relative detuning, and other parameters. Fig. 14 is an example of such dependency.

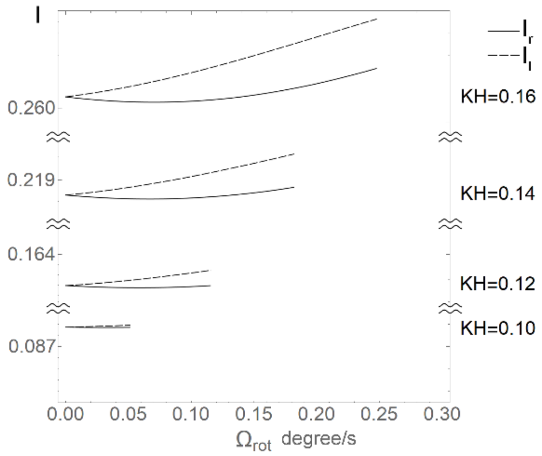

Fig. 12. Dependencies of intensities for counterpropagating waves on the speed of resonator rotation for various values of KH.

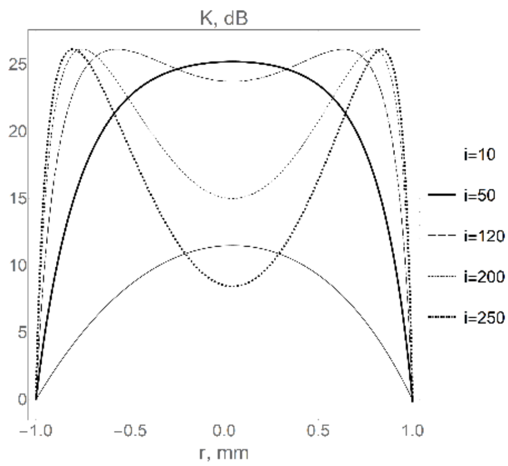

Fig. 13. Transverse distribution of the gain ***K*** for different pumping currents in mA.

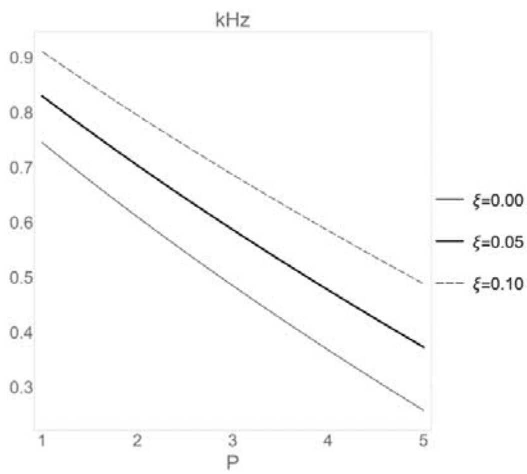

Fig. 14. Dependences of the synchronization threshold on the pressure (Torr) at various relative detuning.

4. Conclusions

Detailed analysis of the results of work [1] was conducted. Synchronization in ring lasers is a multiparametric frequency-dependent effect and depends on the design and geometry of the cavity, as well as on the pumping current, pressure in the active medium, cavity rotation speed, etc. To understand the specifics of the laser work, in every case, it is necessary to have a detailed understanding of the configuration of the laser.

Intensities of counterpropagating waves were researched depending on different laser parameters such as relative detuning, single isotope and isotopes mixture, different losses and frequencies differences of counterpropagating waves. The results for intensities are presented. Qualitative behavior of intensities difference retains the same inside and outside lock-in range boundaries. For the first time, the oscillations in the intensities obtained in [11] were theoretically explained.

It was established theoretically, that lock-in range boundaries are decreasing when pressure is increasing. As a result of the research of Eq. (8), it was confirmed theoretically that the synchronization threshold is higher when the active medium gain is higher and adding a second isotope to the active medium is decreasing the lock-in threshold. In addition, increasing of synchronization threshold while increasing detuning was also predicted based on equations analysis. Comparison with experimental data was conducted. For comparison with the experiment, it is necessary to take into account the change in the spatial distribution of the gain over the cross-section of the tube with the active medium.

5. Annex A. Expressions for Polarization Coefficients

In this Annex full expressions for polarization coefficients $\beta_{r,l}$, $\theta_{r,l}$, Z, $\sigma_{r,l}$ are given.

Polarization calculation from the system of equations for the elements of the density matrix in the third order of the perturbation theory was performed in many works [8], [12] where a small parameter is given by:

$$I_j = \frac{\left|dE_j\right|^2}{\hbar}\frac{1}{\gamma_{ab}}\left(\frac{1}{\gamma_a}+\frac{1}{\gamma_b}\right), \tag{12}$$

where d is the transition dipole moment. The fact that this small parameter is proportional to $\left|E_j\right|^2$, allows to call it dimensionless intensity of the wave.

Unlike other authors Lamb and others we did not separate equations to real and imaginary part. This approach gave a possibility to find analytical equations for polarization coefficients without additional approximations. The detailed description can be found in [13]. Polarization of j -wave is represented in the following form

$$2\pi\kappa_j(z) = (1/k)K\left\{Z_j - \beta_j I_j - \theta_{j'} I_{j'} - \sigma_j\sqrt{I_j I_{j'}}exp\{\mp i\varphi\}\right\} \tag{13}$$

Here it was taken into account the following

$$\begin{aligned} &E_r(z)E_l^*(L-z) \\ &= E_{0r}E_{0l}exp\left\{ik\int_0^z n_j d\tilde{z}\right\} \\ &\times exp\left\{-ik\int_0^{L-z} n_j d\tilde{z}\right\}^* \\ &= E_{0r}E_{0l}exp\left\{i\frac{2\pi}{\lambda}L\right\} \\ &\times exp\left\{-k\int_0^L \left(n_j''\right)d\tilde{z}\right\} \\ &= E_{0r}E_{0l}exp\{\pm i2\pi q\}exp\left\{-kHn_j''\right\} \\ &= E_{0r}E_{0l}exp\left\{-kHn_j''\right\} \end{aligned} \tag{14}$$

$K = 2\pi d^2 N/(\hbar u)$ – gain coefficient per unit length, N – excitation density, u – root mean square velocity of the active medium atoms.

Expression for Z function, which real part describes the linear dispersion (Z') and imaginary part linear amplification (Z'') of the active medium is given by (15).

$$Z(\zeta_j) = 2i\int_0^\infty exp\{-\rho^2 + 2i\rho\zeta_j\}d\rho, \tag{15}$$

where:

$\zeta_j = \frac{(\omega_j - \omega_{ab} + i\gamma_{ab})}{(ku)}$,

ω_{ab} is the frequency of the middle of the gain curve;

ku is the Doppler broadening;

γ_{ab} is the half-widths of the homogeneous line.

Polarization coefficient of self-saturation $\beta_{r,l}$ can be calculated by the following formula:

$$\beta_j = iZ_j'' + 2i\frac{\gamma_{ab}}{ku}\left(1 + \zeta_j Z_j\right) \tag{16}$$

Cross-saturation coefficient $\theta_{r,l}$ can be represented as:

$$\theta_{j'} = \sum_{t=1}^{3}\theta_{j't} \tag{17}$$

$\theta_{r,l}$ is defined by two processes. First is saturation of population difference of the energy states, which leads to existence of the following two terms:

$$\theta_{j'1} = \frac{1+i\Delta}{2(1+\Delta^2)}\left(Z_j + Z_{j'}\right) - \left(\frac{i}{2\Delta}\right)\left(Z_j + Z_{j'}^*\right) \tag{18}$$

Last two terms in (17) appears due to parametric process of modulation of energy state population difference with frequency $\omega_j - \omega_{j'}$. Which leads to increase of the coupling of the counterpropagating waves.

$$\theta_{j'2} = f(\gamma/\gamma_{ab}) \sum_{n=a,b} |\nu_n|^{-2} \left\{ Z\left(\zeta_{jj'}^{(n)}\right) - \left(Z_j - Z_{j'}^*\right)/2 - \alpha_n \theta_{j'2} \right\}, \quad (19)$$

$$\theta_{j'3} = f(\gamma/\gamma_{ab}) \sum_{n=a,b} \nu_n{}^{-2} \left\{ Z_j \left(1 + 2\left(\gamma_{ab}/(ku)\right)^2 \nu_n \nu\right) - Z\left(\zeta_{jj'}^{(n)}\right) + \frac{2\nu_n \gamma_{ab}}{(ku)}, \right\} \quad (20)$$

$$\Delta = \frac{(\omega + \omega_{ab})}{\gamma_{ab}}, \omega = \frac{(\omega_j + \omega_{j'})}{2}, \quad (21)$$

$$\zeta_{jj'}^{(n)} = \left(\omega_j - \omega_{j'} + i\gamma_n\right)/(2ku), \quad (22)$$

$$\nu = \Delta + i, \nu_n = \Delta + i\alpha_n, \alpha_n = 1 - \frac{\gamma_n}{(2\gamma_{ab})}, \quad (23)$$

$$f = \gamma_a \gamma_b/(4\gamma^2), \gamma = (\gamma_a + \gamma_b)/2 \quad (24)$$

Modulation of the population difference of energy state is the main reason for the polarization terms proportional to $\sigma''_{r,l}, \sigma'_{r,l}$. Polarization coefficient σ_j has the form:

$$\sigma_j = \frac{\gamma_a \gamma_b}{8\gamma\gamma_{ab}} \sum_{n=a,b} \left\{ \frac{1}{\nu_{2n}} \left[\frac{3(\Delta - 2i)}{\nu_1 \nu_2} Z\left(\frac{1}{3}\left(\zeta_j + \zeta_{jj'}\right)\right) + \frac{2i\alpha_{1n}}{|\nu_{1n}|^2} Z_{jj'}^{(n)} \right] - \frac{1}{\nu_1 \nu_{1n}} Z_j + \frac{1}{\nu_2 \nu_{1n}^*} Z_{j'}^* \right\}, \quad (25)$$

$$\nu_2 = 2\Delta - i, \nu_{2a,b} = \Delta + i\alpha_{2a,b}, \quad (26)$$

$$\alpha_{2a,b} = 1 - 3\gamma_{a,b}/(2\gamma_{ab}) \quad (27)$$

References

[1]. T. V Radina, Theory of frequency synchronization in a ring laser, *Physics Letters A*, Vol. 379, Issue 36, 2015, pp. 2140–2146.

[2]. A. Zadvorkin, T. Radina, Frequency synchronization in a ring laser, in *Proceedings of the 4th International Conference on Optics, Photonics and Lasers (OPAL'2021)*, 13-15 October 2021, Corfu, Greece, pp. 130–133.

[3]. B. Stieler, D. Loukianov, R. Rodloff, H. Sorg, Optical Gyros and their Application, D. Loukianov and North Atlantic Treaty Organization, *North Atlantic Treaty Organization, Research and Technology Organization*, 1999.

[4]. G. E. Stedman, Z. Li, C. H. Rowe, A. D. McGregor, H. R. Bilger, Harmonic analysis in a large ring laser with backscatter-induced pulling, *Physical Review A*, Vol. 51, Issue 6, 1995, pp. 4944–4958.

[5]. G. E. Stedman, H. R. Bilger, M. T. Johnsson, Z. Li, C. H. Rowe, T violation and microhertz resolution in a ring laser, *Optics Letters*, Vol. 20, Issue 3, 1995, pp. 324-326.

[6]. K. U. Schreiber, J.-P. R. Wells, Invited Review Article: Large ring lasers for rotation sensing, *Review of Scientific Instruments*, Vol. 84, Issue 4, 2013, p. 041101.

[7]. V. A. Alekseev, B. Y. Zel'dovich, I. I. Sobel'man, Parity non-conservation effects in atoms, *Uspekhi Fizicheskih Nauk*, Vol. 118, Issue 3, 1976, pp. 385-408.

[8]. W. E. Lamb, Theory of an Optical Maser, *Physical Review*, Vol. 134, Issue 6A, 1964, pp. A1429–A1450.

[9]. W. M. Macek, D. T. M. Davis, Rotation Rate Sensing with Traveling-Wave Ring Lasers, *Applied Physics Letters*, Vol. 2, Issue 3, 1963, pp. 67–68.

[10]. F. Bretenaker, B. Lépine, A. Le Calvez, O. Adam, J.-P. Taché, A. Le Floch, Resonant diffraction mechanism, nonreciprocity, and lock-in in the ring-laser gyroscope, *Physical Review A*, Vol. 47, Issue 1, 1993, pp. 543–551.

[11]. F. Aronowitz, R. J. Collins, Lock-In and Intensity-Phase Interaction in the Ring Laser, *Journal of Applied Physics*, Vol. 41, Issue 1, 1970, pp. 130–141.

[12]. F. Aronowitz, Theory of a Traveling-Wave Optical Maser, *Physical Review*, Vol. 139, Issue 3A, 1965, pp. A635–A646.

[13]. T. V. Radina, Diffraction phenomena in ring gas lasers, *Quantum Electronics*, Vol. 37, Issue 6, 2007, pp. 503–521.

Sensors & Transducers, Vol. 255, Issue 1, January 2022, pp. 44-52

Sensors & Transducers
Published by IFSA Publishing, S. L., 2022
http://www.sensorsportal.com

Plasmonic Purcell Effect in Single Confined Metallic Layer

Cam Nhung VU and * Julien LAVERDANT
Institut Lumière Matière, Université Claude Bernard Lyon 1, CNRS,
Université de Lyon, F-69622 Villeurbanne, France
E-mail: julien.laverdant@univ-lyon1.fr

Received: 26 November 2021 /Accepted: 29 December 2021 /Published: 31 January 2022

Abstract: In this paper, we present a theoretical and simulation work about the modification of the spontaneous emission of a radiating dipole into a plasmonic device. This problem concerns devices where a nanolight source is directly integrated in nanophotonic devices. The modification of radiation, also called Purcell effect, is calculated using electromagnetism theory of the dissipated power of a point source near or inside a multilayer system. After describing the general effect and the theoretical approach based on the calculation of the Local Density of Optical States (LDOS), we present how this dipole radiates near a metal mirror which supports Surface Plasmon Polariton (SPP) at the metal-dielectric interface. In a second step, we set our attention onto a symmetric system where the metallic layer is confined between 2 insulators. In that late case, the SPP at each interface hybridize to generate two new modes named Long-Range and Short-Range Plasmon. In particular, we analyze the coupling efficiency of the dipole into these new modes and discuss about some potential applications in nanophotonics. The last part of this paper deals with a more realistic device where the insulator layers display finite sizes which lead to the existence of waveguided mode in the structure.

Keywords: Purcell effect, Surface plasmon, Waveguide, Strong coupling, Mode hybridization, Coupling efficiency, Nanophotonic.

1. Introduction

Among the numerous developments in integrated photonic devices, there is still challenges to engineer more efficient nanosources of light [1]. The recent advances in nanofabrication have made possible the realization of optical telecommunication devices with many integrated specificities [2]. Nowadays, there is a strong demand on the development of integrated photonic quantum devices [3]. The light-matter interaction can be engineered to create: new lasers based on polariton condensates [4], polariton fluids [5], single photon sources [6], reconfigurable photonic elements that can be switched [7], low loss waveguides [8], quantum logical gates [9], generation of non-classical state of light [10], wavelength conversion and non-linearities [11]. All these promising applications rely on the design of integrated devices that are compact, efficient without losses. In general, much materials depend on the wavelength of applications either by their optical dispersion or absorption, bands diagram, direct or indirect gap [12].

For example, vertical devices based on Bragg mirrors with a micro-cavity have been designed to realize semiconductor lasers [13] or ultra-bright single-photon sources [14]. The idea of this 1D photonic crystal has been extended to 2D photonic crystals [15]. Many realizations for quantum optics have been achieved based on these photonic crystals such as waveguided single photon sources [16], strong coupling [17], polarization entanglement [18] and ultrafast lasers [19]. The key point in all these realizations is the optimization of the devices. One criteria, to optimize the light-matter interaction, is based on the Purcell factor [20] that stipulates that the photon emission rate is increased when the emitter is inserted in a device with a confined mode volume and a strong quality mode factor. The mode volume is in general diffraction limited [21]. The quality factor that represent the time of interaction between the photon and the mode depends strongly on the losses inside the device [22]. For example, in the case of a nano-cavity inserted inside a photonic crystal, the cavity-edges are crucial [22, 23]. In this case, losses are induced by the junction between the cavity field and the mirror which lead to evanescent lossy waves.

Otherwise, evanescent waves can present advantages due to a high confinement of the mode volume which is smaller than the diffraction limit [24]. In the case of metals, Surface Plasmon Polaritons (SPPs) are evanescent waves at the interface between a metal and a dielectric interface [25]. SPPs are electromagnetic waves that propagate over a few microns at the metal-dielectric interface. It is an evanescent wave that possess a TM (or p) polarization. It is characterized by an in-plane wavevector given by Eq. (1) as:

$$k_{spp} = \frac{2\pi}{\lambda}\sqrt{\frac{\varepsilon_d \varepsilon_m}{\varepsilon_d + \varepsilon_m}}, \tag{1}$$

where λ is the wavelength and the dielectric constants of the dielectric and metal are respectively ε_d and ε_m. The dielectric constant of the metal is subject to losses so that the imaginary part can be important depending on the wavelength. Metals such as gold and silver are commonly used because they display few losses in the visible range [26]. As the dielectric constant, depends on the wavelength, the real part of the wavevector describe the dispersion relationship and the imaginary part is related to the propagation length L_{spp} [25].

Despite their losses, the high confinement and strong associated electromagnetic field have led to many interesting applications. Stimulated emission in waveguide [27], vertical lasers based on TAMM mode [28] and nano-lasers also called SPASER [29] have been demonstrated. Quantum plasmonic has emerged and demonstrations such as strong coupling [30, 31], single plasmons [32] and coalescence [33, 34] have been realized. Recently collective emission in superradiant state induced by SPP have been achieved [35].

Nevertheless, the major limitations of SPP come from the losses form the optical constant or by leakage. In the case of a thin metallic layer, the SPP mode can be leaky so that the propagation length is reduced. There is a particular case when the metallic layer is very thin and inserted between 2 identical insulators. The plasmon at each interface hybridize into a long-range and a short range plasmon [36, 37]. The long-range mode possesses a propagation length a few times higher than the SPP and is particularly interesting for integrated devices such as waveguides [38] and interferometers [39]. A demonstration of strong coupling for quantum optics has also been achieved [40].

The motivation of the present work is to show how quantum emitters (such as single molecule or quantum dots) can couple to a planar metallic layer that support hybridized SPP and in particular to realistic structures composed of finite size layers. This fundamental case is particularly important for integrated nanosources or quantum plasmonic with surface plasmons.

In a first part, we recall and detail how we calculate the Local Density of Optical States to deduce the Purcell factor. In a second step, we apply the model to the case of a gold mirror to identify and recall the coupling properties to a Surface Plasmon. In the two last part of the paper, we discuss the cases when the metallic layer is thin and inserted between insulators. The case of infinite insulating layers will be discussed to identify the modes and understand the coupling. A second case will be discussed which is more realistic when the insulators possess finite sizes.

2. Theoretical Model for the Calculation of the Purcell Effect and the LDOS

2.1. Link Between the Local Density of Optical States (LDOS) and the Purcell Factor

The spontaneous decay rate of a two level system weakly coupled to an external electromagnetic mode follows the Fermi's golden rule:

$$\Gamma = \frac{\omega\pi}{3\varepsilon_0\hbar}|p|^2\,\rho(r,\omega), \tag{2}$$

where the Local Density of Optical States (LDOS) is ρ, the amplitude and the position of the dipole are respectively $|p|^2$ and r. The ratio of the decay rate of the 2-level system in a local (Γ) and a homogeneous surrounding (Γ_0) has been introduced by Purcell [20]:

$$F_p = \frac{\Gamma}{\Gamma_0} = \frac{\rho}{\rho_0} \tag{3}$$

The Purcell factor represents at the same time the modification of the decay rate and the LDOS. The published work [20] shows that the spontaneous decay rate of a single emitter was modified when placed inside a Fabry-Perot cavity. In such cavity, the emitter will decay in modes described by successive lorentzian functions of the frequency. It has been demonstrated that the modification follows:

$$F_P = \frac{3\lambda^3}{4\pi^2}\frac{Q}{V}, \tag{4}$$

where F_p is the so-called Purcell factor, λ is the emission wavelength of the emitters, Q and V are characteristics of the mode. Q is the resonance quality factor and V is the mode volume defined, in a non-dispersive medium of local optical constant $\varepsilon(r)$, as:

$$V = \frac{\int \varepsilon(r)\left|E(r)\right|^2 dr}{\max[\varepsilon(r)\left|E(r)\right|^2]} \quad (5)$$

In this expression, $|E(r)|^2$ is the intensity of the electric field associated to the mode. The final expression of the Purcell factor in Eq. (4) shows that it is maximum when the quality factor is very high and the mode volume is small. In the case considered in this paper, we use plasmonic structures based on metals so that the quality factor will be generally under 100 but the field confinement possesses a mode volume smaller than λ^3.

2.2. Power Dissipation of a Dipole Near a Planar Structure

The general Purcell factor is defined by Eq. (3) which is the ratio of the decay rates. In principle, the decay rates can only be calculated in quantum mechanics and differ from classical formula. Nevertheless, the relative modifications of the emission rates in presence of a nanostructured compared to free space are identical [41].

$$F_P = \left(\frac{\Gamma}{\Gamma_0}\right)_{quantum} = \left(\frac{\Gamma}{\Gamma_0}\right)_{classic} \quad (6)$$

Using this analogy, we are able to use classic electromagnetism calculations to simulate the Purcell factor. For that model, we consider the power P dissipated by a dipole of energy E_{dipole}:

$$P = -\Gamma E_{dipole} \quad (7)$$

In the present work, we consider surface modes which are defined by their in-plane wavevector $k_{//}$. In the following, we will use the normalized wavevector u such as:

$$u = n_0 \frac{k_{//}}{2\pi/\lambda}, \quad (8)$$

where n_0 is the optical index where the dipole is located, u is very interesting parameters that delimits propagating waves in free space ($u<n_0$) and evanescent waves ($u>n_0$). Furthermore, by this definition, u will also represent the effective index of the modes. The Purcell factor can be therefore decomposed on these wavevectors by [42]:

$$F_p = \int \alpha(u) du \quad (9)$$

The quantity α represents the derivative of the power dissipated by wavevector and will allow us to identify surface modes. The expression of α depends on the position of the dipole and its orientation. In Fig. 1, we present the two main cases that are considered. The dipole is placed in the medium 0. The emitted electromagnetic waves will depend on the orientation of the dipole. If the dipole is parallel to the surface, TM (p) and TE (s) waves will excite the surface. In the case of a vertical dipole, only TM (p) waves will be generated [41]. As this paper deals with the excitation of SPP which are TM (p) modes, we set the dipole vertical to the all interfaces.

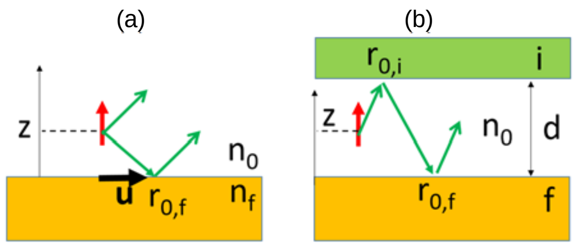

Fig. 1. Schematic of the calculated system. The dipole (red arrow) is set at a distance z from the bottom interface. (a) Dipole placed inside a semi-infinite medium, and (b) inside a layer of thickness d. 0, i and f denotes the dipole medium, upper and bottom layer respectively. Note that the medium i or f can be composed of multilayers.

The general expression of α for a vertical dipole (orientation perpendicular to the layer) is:

$$\alpha_{\perp}(u) = \frac{3}{2}\mathrm{Re}\left[1 + g(u)\frac{u^3}{\sqrt{n_0^2 - u^2}}\right] \quad (10)$$

In this expression, we observe two terms which comes from the direct light in a direction u and a second one that depend on the function *g(u)*.

2.3. Analytic Expression of the Dissipated Power in a Multilayer Structure

As we see on the general expression of the dissipated power, we need the expressions of the function *g(u)*. Its formula is given by $g_1(u)$ or $g_2(u)$ if the dipole is placed in a semi-infinite layer (Fig. 1(a)) or inside a finite layer (Fig. 1(b)). For a single interface (Fig. 1(a)), the expression is given by [42]:

$$g_1(u) = r_{0,f}^p \exp(2ik_{z,0}z) \quad (11)$$

The projection of the wavevector is $k_{z,0} = \frac{2\pi}{\lambda}\sqrt{n_0^2 - u^2}$. We see that in the case of a semi-infinite layer, $g_1(u)$ is only given by the propagation distance to the interface and the Fresnel reflection coefficient $r^p_{0,f}$. If the dipole is placed inside a finite layer, we have:

$$g_2(u) = \frac{1}{1-2r^p_{0,f}r^p_{0,f}\exp(2ik_{z,0}d)} \{2r^p_{0,i}r^p_{0,f}\exp[2ik_{z,0}d] + r^p_{0,i}\exp[2ik_{z,0}(d-z)] + r^p_{0,f}\exp(2ik_{z,0}z)\} \quad (12)$$

The main difference with one interface is that the reflection coefficient of both upper ($r^p_{0,i}$) and lower ($r^p_{0,f}$) layer must be taken into account. For clarity of the different expressions, we removed the angular dependence of the Fresnel coefficient with the in-plane wavevector u. Finally, the Fresnel reflection coefficients are calculated by analytical Matrix formalism [43] and depends on the considered structure through their indices and thicknesses.

2.4. Coupling Efficiency (β-factor)

So far, we have presented the Purcell factor that represents the modification of the total power of the emitter. It is also very useful to quantify the coupling efficiency in each available mode or channel. This parameter is a key point in the optimization of devices for integrated photonics as for example waveguides or cavities [16]. The coupling efficiency in a specific mode is called the β-factor and is defined as:

$$\beta = \frac{\Gamma_{mode}}{\Gamma_{total}} = \frac{\int_{u\in\{mode\}} \alpha(u)du}{\int_0^{+\infty} \alpha(u)du} \quad (13)$$

The β-factor will then be calculated using the value of the power α from the previous expression.

2.5. Reconstruction of the Mode Profile

It is also very useful to dispose of the shape of the mode profile in order to identify the modes and locate where the electromagnetic field is more intense. The last quantity, we can compute with the dissipated power α is the power in each mode:

$$\frac{\Gamma_{mode}}{\Gamma_0} = \int_{u\in\{mode\}} \alpha(u)du \quad (14)$$

This quantity is normalized and will represent the normalized power of the mode. For each position of the dipole, the dissipated power α is calculated and integrated. The profile of the mode will then be deduced. This procedure is a way to reconstruct the mode volume which is fundamental to understand the Purcell factor.

3. Spontaneous Emission of a Radiating Dipole near a Thick Gold Mirror

In the previous part, we described the model and defined the different physical quantities that we will calculate. We first consider the simple case of a dipole coupled to a gold mirror [48]. For the calculation, we set the dipole emission wavelength λ=650nm so that the gold optical index is [26]: n_{gold}=0.15+3.32i. The results are presented in Fig. 2.

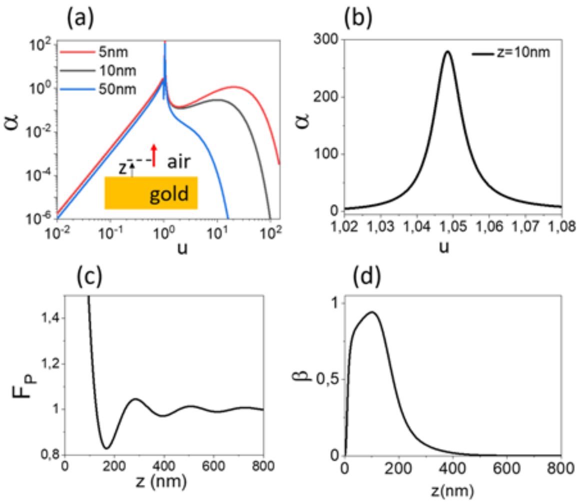

Fig. 2. Simulations of the power dissipated by a vertical dipole in the air located near a gold mirror. (a) Dissipated power as function of u for several gold-dipole distance; (b) Zoom of the dissipated power (for z=10 nm) around the plasmonic resonance u_{SPP}=1.048. (c) Evolution of the Purcell factor with the vertical distance z. (d) Coupling efficiency to the SPP mode as function of the distance.

When the dipole is near the gold mirror, we observe that the dissipated power is absorbed into 3 regions in Fig. 2 (a). When u<1, the power is radiated in free space whereas when u>1, the power is absorbed into the evanescent waves. It is known, that in the evanescent part, two modes arise which are the Surface Plasmon Polaritons with a wavevector defined by Eq. (1) and a broad range of wavevectors above the SPP which are called Lossy Surface Waves (LSW).

If we make a zoom to identify the shape of SPP in Fig. 2 (a), we clearly observe in Fig. 2 (b) a Lorentzian-type shape curve centered at u=1.048 which perfectly matches the value from Eq. (1). More information can be deduced from this curve. As it is well known [44], the SPP is a purely coherent mode so that it is only limited by Fourier Transform. Therefore, the width in wavevector (Δu) is related to the intensity decay length of the SPP (L_{SPP}). The relationship in the case of a Lorentzian-type shape is given by:

$$L_{SPP} = \frac{\lambda}{\pi\Delta u} \quad (15)$$

With the value deduced in Fig. 2 (b), we extract a propagation length of 20 µm. The Purcell factor presented in Fig. 2 (c) is decreasing with the distance z and then make a few oscillations around 1. As the distance z is increasing, the number of optical modes are decreasing. Oscillations appear from interferences of the light emitted by the dipole and its reflection. From the power, we extract the β-factor to the SPP as previously explained. In Fig. 2(d), the maximum efficiency that is found is around 90 % for a distance of 100 nm. This very high absorption into SPP comes from the vertical orientation of the dipole [45].

4. Purcell Effect near a Confined Gold Film: the Long-range Surface Plasmon

In the previous part, we discussed about the coupling of the dipole near a gold mirror. A gold mirror is a good approximation when the gold thickness is more than 5 times the skin depth of the metal [45]. In this part, we analyze the case of a gold film which size is similar to the skin depth. If we position the radiating dipole above the thin gold layer, a new plasmonic channel is opened. Indeed, the surface will now support one SPP on each interfaces [25]. This case becomes more interesting when the insulators surrounding the gold layer possess the same optical index as we will show in the following. In Fig. 3, we simulate the dissipated power of the dipole located in the glass above a thin gold layer (20 nm thick).

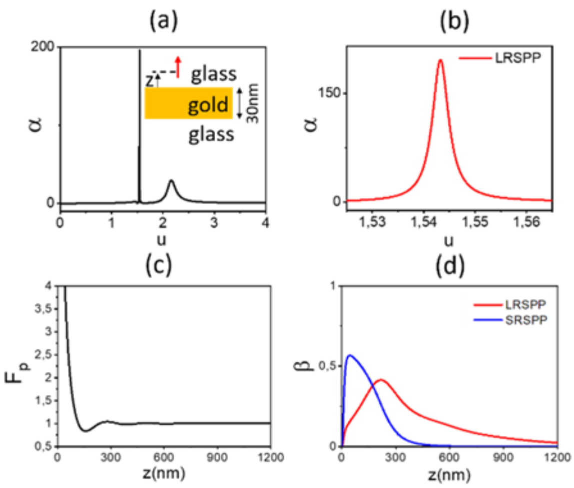

Fig. 3. Simulations of the power dissipated by a vertical dipole in the glass near a very thin gold layer. (a) Dissipated power as function of u for z=10 nm. (b) Zoom of the dissipated power around the LRSPP mode around u_{LRSPP}=1.544. (c) Evolution of the Purcell factor with the vertical distance z. (d) Coupling efficiency to the LRSPP and SRSPP modes as function of the distance.

When the optical indices around the thin gold layer are the same, the SPP on each side possesses the same momentum so that SPP hybridization occurs [36]. This phenomenon is similar to the case of bonding and antibonding of the wave functions in a molecular system or in strong coupling in quantum physics. As a consequence, two new SPPs arise: the long-range (LRSPP) and short-range (SRSPP) surface plasmons. In Fig. 3, we clearly observe that the dipole located at 10 nm from this surface excite these two modes with different width Δu. From Fig. 3(a), we identify the mode with smaller width (located at u=1.544) to the long-range plasmon whereas the other mode (at u=2.16) is called the short range plasmon. It is important to highlight that a strong width reduction occurs for the case of long-range as presented in Fig. 3(b). From the width in u, we deduce that the propagation length of the long-range and short range plasmon are respectively 100 µm and 1 µm. The evolution of the Purcell factor in Fig. 3(c) is very similar to the one in the case of the gold mirror in Fig. 2(c). Indeed, the device does not create new modes but split the initial mode in 2 but with different amplitudes. This last observation is also valid for the coupling efficiencies presented in Fig. 3(d). The short range plasmon is located at very small distance to the interface (42 nm) with a maximum efficiency of 56 % whereas the long-range plasmon maximum efficiency is around 42 % for a distance farther to the interface (225 nm).

For many applications which need a longer propagation constant such as integrated interferometers for example, the long-range mode is particularly interesting. This mode has the same properties of the SPP (same Purcell factor) and propagates 5 times farther. Nevertheless, the maximum coupling efficiency is only 42 % at maximum.

5. Coupling a Dipole to a Finite Gold Film Deposited Onto a Glass Substrate

In this last part, we focus on a realistic device with finite size layers surrounding the thin gold film. We will describe how to optimize the structure depending on the purpose of the desired applications. The whole structure is deposited on a prism of higher index to allow the extraction of the plasmon mode. This experimental scheme is also called the Otto configuration [25, 46].

5.1. Schematic of a Realistic Device

In order to clarify the design of the multilayer structure, we display, in Fig. 4, a scheme of the modeled structure. We set a prism of high optical index (n=1.8) which can be made with LaSF glass with low absorbance for the visible wavelength [40]. The gold layer has a thickness of 30 nm and is sandwiched between two glass layers (n=1.5) of thickness 750 nm. The glass layer above the prism is denoted the coupling layer as it sticks the gold and the prism. The top glass layer will be called the cladding layer. The whole device is set in the air.

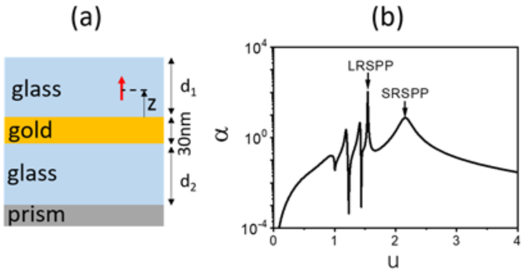

Fig. 4. (a) Schematic of the device under consideration. The dipole (red arrow) is placed in the upper glass at a distance z from the gold. The gold layer thickness is 20 nm and the glass thicknesses are respectively d_1=750 nm and d_2=750 nm for the top and bottom. The prism is semi-infinite. (b) Dissipated power α of the dipole at z=10 nm.

We also present in Fig. 4(b), a first calculation of the power dissipated by the dipole placed at 10 nm above the gold inside the top layer. The situation is the same as in Fig. 3 except that the glass possesses finite size. The result shows that complimentary to the 2 previously identified plasmonic modes (long-range and short-range), new modes appear at smaller wavevectors u. The wavevector of these modes lies between the air (u=1) and the glass (u=1.5). This particular case is very similar to the presence of waveguided modes in which the effective index of these modes lies in the interval between the optical index of the outside and the optical index of the internal part of the guide [47].

In order to validate the hypothesis of the appearance of waveguided modes and to highlight the dependence of these modes onto the parameters of the device, we present some calculation to optimize the modal structure.

5.2. Structure Optimization

The number of variable parameters become more important in the device's scheme of Fig. 4(a). We present in Fig. 5, a complimentary simulation. As explained in the description of our model, we need to calculate the Fresnel reflection coefficients. In the case under investigation in Fig. 4(a), we calculate the reflection coefficient R_p (in power) as function of the cladding layer (d_1) for different incident wavevector u. In this prism configuration, the incident angle θ is defined as: u=n sin(θ). The light is sent through the prism of index n=1.8. This light is propagative so that the maximum in-plane wavevector u is 1.8. The coupling layer (d_2) is fixed with a value d_2=750 nm.

In Fig. 5, we clearly identify the LRSPP which is located above u=1.5 and the WGM which are located for u in the interval [1-1.5]. This result shows that depending on the chosen thickness d_1, the number of guided modes change. One particularly interesting point is that the wavevector of the WGMs change with the thickness. As u also represents the effective index of the mode, we see that when d_1 is increasing, the effective index of the WGMs tends 1.5 which is the optical index of the glass.

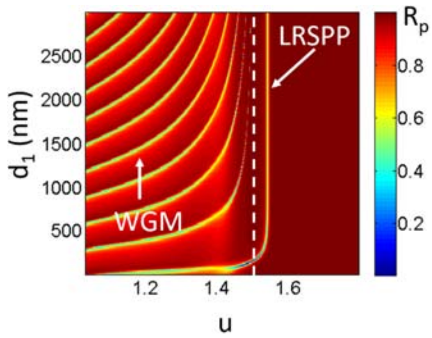

Fig. 5. (a) Evolution of the reflected intensity R_p as function of d_1 and u in an Otto-prism configuration. WGM: WaveGuided Modes. LRSPP: LongRange Surface Plasmon Polariton. The vertical white dashed line represents u=1.5.

As this map is useful to design devices with controlled number of modes for future applications, we give an example. If we take a cladding thickness of d_1=750 nm, we cross 2 WGMs and the LRSPP. This case corresponds to the result obtained in Fig. 4 when the dipole, inserted inside the device, has excited 2 WGMs, the long-range and short-range plasmons. The profiles of the different modes of this device are also reconstructed as explained by Eq. (14) and displayed in Fig. 6 as function of the vertical distance z within the device.

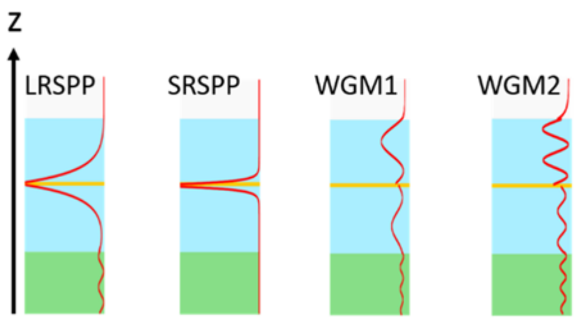

Fig. 6. Mode profiles (continuous red line) of the 4 modes available. The green, blue and yellow layers represent respectively the prism, the glass and the gold.

The profile of each mode is in good agreement with the previous analysis. The plasmonic modes (LRSPP and SRSPP) display exponential decays from the gold layer whereas the WGM present oscillations according to their order. Due to the symmetry of the device, the fundamental modes WGM1 is not exactly centered in the middle of the dielectric. Oscillations are also observed in the lower dielectric (coupling layer).

5.3. Influence of the Waveguided Modes on the Purcell Factor and Coupling Efficiencies

In the previous sub-part, we have presented how to optimize the number of waveguided modes in the final device by analyzing the evolution of the Fresnel reflection coefficient with the device parameters. We keep the same conditions $d_1=d_2=750$ nm in order to excite 2 waveguided modes (WGMs), the short-range (SRSPP) and long-range plasmon (LRSPP). Fig. 7 presents the Purcell factor and β-factors for this optimized structure as function of z for a vertical dipole located inside the cladding layer. Each mode's wavevector u has been identified in the dissipated power α(u), in Fig. 4 (b), and the coupling efficiency is then calculated with Eq. (13).

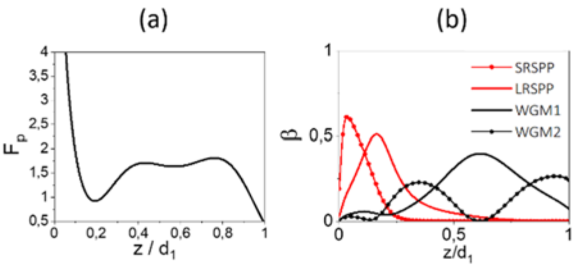

Fig. 7. (a) Purcell factor and (b) β-factors as a function of dipole-gold distance z normalized to the cladding thickness d_1=750 nm. The acronyms SRSPP, LRSPP and WGM are defined in the text.

The curve of the evolution of the Purcell factor in Fig. 7(a) is different than the previous one of Fig. 3(c). For small distances ($z<0.2d_1$), we observe the same evolution if the layers are infinite. Indeed, at small distances, the evanescent waves are not perturbed by the finite thickness (d_1=750 nm) so that the LDOS in this region is the same. An increase is observed for higher distances to the gold. Indeed, in this device, waveguided modes appear due to the presence of finite glass layers. These modes are propagative and are more located in the center of the dielectric as presented in Fig. 6. Therefore, we observe an increase of the LDOS around the middle of glass layer.

The coupling efficiencies to the long-range and short range plasmon in Fig. 7(b) are not modified. These are evanescent waves linked to the gold layer and are not perturbed by the presence of the waveguided modes. As previously explained, we have optimized this device to possess 2 WGMs. The optimal coupling distance to each mode depends on its order as seen in Fig. 7(b). For example, the fundamental guided mode (WGM1) is nearly centered inside the glass layer. Note that the asymmetry of WGM comes from geometry of the device. Finally, in this particular example, the coupling efficiency to WGM1 is around 40 % which is similar to the β of the LRSPP.

6. Conclusion

In this paper, we have presented the model to calculate the modification of the spontaneous emission of a dipole near multi-layer structures. The radiated emission is characterized by the Purcell factor and the coupling efficiency to the desired optical modes. In the case of plasmonic structures, the Purcell factor can be important at very short distance due to an important density of optical states. Nevertheless, all the emission will be dissipated in lossy modes. A compromise can be found with the coupling distance where the Purcell factor is still important and the emission is efficiently coupled to the desired mode without too important losses.

In particular, we focused our work onto the Surface Plasmon Polaritons excited on a gold mirror or a thin gold layer between insulators. In the late case, new plasmons arise from the coupling between each interface. A specific mode called the long-range plasmon can be excited with nearly 50 % of efficiency which possess a propagation length of 100 µm for visible wavelengths. At the end, we presented a realistic structure composed of finite size layers deposited on a substrate. In this case, new optical modes appear from the insulators. We have shown that these new modes are waveguided waves. We presented an optimization of the structure in order to control the number of waveguided modes available for the dipole. This particular case is very promising for integrated nanophotonic devices as it possesses many modes linked to the metal or the insulator with propagation length of a few 100 µm.

Acknowledgements

The authors acknowledge the French region Auvergne-Rhône-Alpes (PAI n° 21PACK-LAV).

References

[1]. V. P. Veiko, V. I. Konov, Fundamentals of Laser-Assisted Micro- and Nanotechnologies, *Springer Series in Material Sciences*, Springer, Vol. 195, 2014.

[2]. H. Zhang, M. Gu, X. D. Jiang, J. Thompson, H. Cai, S. Paesani, R. Santagati, A. Laing, Y. Zhang, M. H. Yung, Y. Z. Shi, F. K. Muhammad, G. Q. Lo, X. S. Lo, B. Dong, D. L. Kwong, L. C. Kwek, A. Q. Liu, An optical neural chip for implementing complex-valued neural network, *Nature Communication*, Vol. 12, 2021, 457.

[3]. A. W. Elshaari, W. Pernice, K. Srinivasan, O. Benson and V. Zwiller, Hybrid integrated quantum photonic circuits, *Nature Photonics*, Vol. 14, Issue 5, 2020, pp. 285-298.

[4]. E. Wertz, L. Ferrier, D. D. Solnyshkov, R. Johne, D. Sanvitto, A. Lemaître, I. Sagnes, R. Grousson, A. V. Kavokin, P. Senellart, G. Malpuech, J. Bloch, Spontaneous formation and manipulation of extended polariton condensates, *Nature Physics*, Vol. 6, Issue 11, 2010, pp. 860-864.

[5]. A. Amo, S. Pigeon, D. Sanvitto, G. G. Sala, R. Hivet, I. Carusotto, F. Pisanello, G. Leménager, R. Houdré, E. Giacobino, C. Ciuti, A. Bramati, Polariton Superfluids Reveal Quantum Hydrodynamic Solitons, *Science*, Vol. 332, Issue 6034, 2011, pp. 1167-1170.

[6]. E. Meyer-Scott, C. Silberhorn, A. Migdall, Single-photon sources: Approaching the ideal through multiplexing, *Review of Scientific Instruments*, Vol. 91, Issue 4, 2020, 041101.

[7]. B. J. Metcalf, J. B. Spring, P. C. Humphreys, N. Thomas-Barbieri, W. S. Kolthammer, X.-M. Jin, N. K. Langford, D. Kundys, J. C. Gates, B. J. Smith, P. G. R. Smith, I. A. Walmsley, Quantum teleportation on a photonic chip, *Nature Photonics*, Vol. 8, 2014, pp. 770-774.

[8]. A. Politi, J. C. F. Matthews, M. G. Thompson, J. L. O'Brien, Integrated Quantum Photonics, *IEEE Journal of Selected Topics in Quantum Electronics,* Vol. 15, Issue 6, 2009, pp. 1673-1684.

[9]. Y. Zhou, D-Y. Lü, W-Y. Zeng, Chiral single photon switch-assisted quantum logic gate with a nitrogen-vacancy center in a hybrid system, *Photonic Research*, Vol. 9, Issue 3, 2021, 405.

[10]. S. Azzini, D. Grassani, M. J. Strain, M. Sorel, L. G. Helt, J. E. Sipe, M. Liscidini, M. Galli, D. Bajoni, Ultra-low power generation of twin photons in a compact silicon ring resonator, *Optics Express*, Vol. 20, Issue 21, 2012, pp. 23100-23107.

[11]. X. Guo, C-l. Zou, C. Schuck, H. Jung, R. Cheng, H. X. Tang, Parametric down-conversion photon-pair source on a nanophotonic chip, *Light: Science & Applications*, Vol. 6, Issue 5, 2017, e16249.

[12]. M. Fox, Optical Properties of Solids, Oxford Master Series in Condensed Matter Physics, *Oxford University Press*, 2010.

[13]. R. Michalzik, VCSELs: Fundamentals, technology and Applications of Vertical-Cavity Surface-Emitting lasers, *Springer Series in Optical Sciences, Springer*, 2013.

[14]. A. Dousse, L. Lanco, J. Suffczynski, E. Semenova, A. Miard, A. Lemaître, I. Sagnes, C. Robin, J. Bloch, P. Senellart, Controlled Light-Matter Coupling for a Single Quantum Dot Embedded in a Pillar Microcavity Using Far-Field Optical Lithography, *Physical Review Letters*, Vol. 101, Issue 26, 2008, 267404.

[15]. J. D. Joannopoulos, S. G. Johnson J. N. Winn, R. D. Meade, Photonic Crystals Molding the flow of Light, *Princeton University*, 2008.

[16]. H. Thyrrestrup, L. Sapienza, P. Lodahl, Extraction of the β-factor for single quantum dots coupled to a photonic crystal waveguide, *Applied Physics Letters*, Vol. 96, 2010, 231106.

[17]. M. A. Dundar, J. A. M. Voorbraak, R. Nötzel, A. Fiore, R. W. Van der Heijden, Multimodal strong coupling of photonic crystal cavities of dis-similar size, *Applied Physics Letters*, Vol. 100, 2012, 081107.

[18]. G. He, C. Zhu, Y. Jiang, J. Ren, Y. Guo, J. Jing, Generation of path-polarization hyper entanglement using quasi-phase-matching in quasi-periodic non-linear photonic crystal, *Scientific Reports*, Vol. 7, 2017, 4954.

[19]. H. Altug, D. Englund, J. Vuckovic, Ultrafast photonic crystal nanocavity laser, *Nature Physics*, Vol. 2, 2006, pp. 484-488.

[20]. E. M. Purcell, Spontaneous Emission Probabilities at Radio Frequencies, *Physical Review*, Vol. 69, 1946, 681.

[21]. G. Grynberg, A. Aspect, C. Fabre, Introduction to quantum optics, *Cambridge University Press*, 2010.

[22]. P. Lalanne, C. Sauvan, J. P. Hugonin, Photon confinement in photonic crystal nanocavities, *Laser & Photonics Reviews*, Vol. 2, Issue 6, 2008, pp. 514-526.

[23]. Y. Akahane, T. Asano, B-S. Song, S. Noda, High-Q photonic nanocavity in a two-dimensional photonic crystal, *Nature*, Vol. 425, 2003, pp. 944-947.

[24]. A. F. Koenderink, On the use of Purcell factors for plasmon antennas, Optics Letters, Vol. 35, Issue 24, 2010, pp. 4208-4210.

[25]. S. A. Maier, Plasmonics: Fundamentals and Applications, *Springer*, 2007.

[26]. P. B. Johnson, R. W. Christy, Optical Constants of the Noble Metals, *Physical Review B*, Vol. 6, Issue 12, 1972, pp. 4370-4379.

[27]. J. Grandidier, G. Colas des Francs, S. Massenot, A. Bouhelier, L. Markey, J.-C. Weeber, C. Finot, A. Dereux, Gain-Assisted Propagation in a Plasmonic Waveguide at Telecom Wavelength, *Nanoletters*, Vol. 9, Issue 8, 2009, pp. 2935-2939.

[28]. C. Symonds, G. Lheureux, J. P. Hugonin, J. J. Greffet, J. Laverdant, G. Brucoli, A. Lemaître, P. Senellart, J. Bellessa, Confined Tamm Plasmon Lasers, *Nano Letters*, Vol. 13, Issue 7, 2013, pp. 3179-3184.

[29]. R.-M. Ma, R. F. Oulton, Applications of nanolasers, *Nature Nanotechnology*, 14, Issue 1, 2019, pp. 12-22.

[30]. P. Törma, W. L. Barnes, Strong coupling between surface plasmon polaritons and emitters: a review, *Reports on Progress in Physics*, Vol. 78, Issue 1, 2015, 013901.

[31]. R. Chikkaraddy, B. de Nijs, F. Benz, S. J. Barrow, O. A. Scherman, E. Rosta, A. Demetriadou, P. Fox, O. Hess, J. J. Baumberg, Single-molecule strong coupling at room temperature in plasmonic nanocavities, *Nature*, 535, Issue 7610, 2016, pp. 127-130.

[32]. A. V. Akimov, A. Mukherjee, C. L. Yu, D. E. Chang, A. S. Zibrov, P. R. Hemmer, H. Park, M. D. Lukin, Generation of single optical plasmons in metallic nanowires coupled to quantum dots, *Nature*, Vol. 450, Issue 7168, 2007, pp. 402-406.

[33]. B. Vest, M.-C. Dheur, E. Devaux, A. Baron, E. Rousseau, J. P. Hugonin, J. J. Greffet, G. Messin, F. Marquier, Anti-coalescence of bosons on a lossy beam splitter, *Science*, Vol. 356, Issue 6345, 2017, pp. 1373-1376.

[34]. G. Fujii, T. Segawa, S. Mori, N. Namekata, D. Fukuda, S. Inoue, Preservation of photon indistinguishability after transmission through surface-plasmon-polariton waveguide, *Optics Letters*, Vol. 37, Issue 9, 2012, pp. 1535-1537.

[35]. Y. Luo, G. Chen, Y. Zhang, L. Zhang, Y. Yu, F. Kong, X. Tian, Y. Zhang, C. Shan, Y. Luo, J. Yang, V. Sandoghdar, Z. Dong, J. G. Hou, Electrically Driven Single-Photon Superradiance from Molecular Chains in a Plasmonic Nanocavity, *Physical Review Letters*, Vol. 122, Issue 23, 2019, 233901.

[36]. P. Berini, Long-range surface plasmon polariton, *Advanced Optics and Photonics*, Vol. 1, 2009, pp. 484-588.

[37]. J. Laverdant, C-N. Vu, Purcell factors of hybrid surface plasmons and waveguided modes, in *Proceeding of the 4th International Conference on Optics, Photonics and Lasers (OPAL'2021)*, Corfu, Greece, 13-15 October 2021, pp. 39-40.

[38]. A. Degiron, S.-Y. Cho, C. Harrison, N. M. Jokerst, C. Dellagiacoma, O. J. F. Marin, D. R. Smith, Experimental comparison between conventional and

hybrid long-range surface plasmon waveguide bends, *Physical Review A*, Vol. 77, Issue 2, 2008, 021804(R).
[39]. H. Fan, R. Charbonneau, P. Berini, Long-range surface plasmon triple-output Mach-Zehnder interferometers, *Optics Express*, Vol. 22, Issue 4, 2014, pp. 4006-4020.
[40]. K. Chevrier, J.-M. Benoit, C. Symonds, J. Paparone, J. Laverdant, J. Bellessa, Organic Excitons in strong coupling with long-range surface plasmons and waveguided modes, *ACS Photonics*, Vol. 5, Issue 1, 2018, pp. 80-84.
[41]. L. Novotny, B. Hecht, Principles of Nano-Optics, *Cambridge University Press*, 2006.
[42]. W. Lukosz, Theory of optical-environment-dependent spontaneous-emission rates for emitters in thin layers, *Physical Review B*, Vol. 22, 1980, pp. 3030-3038.
[43]. A. Shalabney, I. Abdulhalim, Electromagnetic fields distribution in multilayer thin film structures and the origin of sensitivity enhancement in surface plasmon resonance sensors, *Sensors and Actuators A: Physical*, Vol. 159, Issue 1, 2010, pp. 24-32.
[44]. S. Aberra Guebrou, J. Laverdant, C. Symonds, S. Vignoli, J. Bellessa, Spatial coherence properties of surface plasmon investigated by Young's slit experiment, *Optics Letters*, Vol. 37, Issue 11, 2012, pp. 2139-2141.
[45]. C. Vion, P. Spinicelli, L. Coolen, C. Schwob, J.-M. Frigerio, J.-P. Hermier, A. Maître, Controlled modi-fication of single colloidal CdSe/ZnS nanocrystal fluorescence through interactions with a gold surface, *Optics Express*, Vol. 18, Issue 7, 2010, pp. 7440-7455.
[46]. A. Otto, Excitation of nonradiative surface plasma waves in silver by the method of frustrated total reflection, *Zeitschrift Für Physik A: Hadrons Nuclei*, Vol. 216, Issue 4, 1968, pp. 398-410.
[47]. M. Born, E. Wolf, Principles of Optics, Electromagnetic Theory of Propagation Interference and Diffraction of Light, *Cambridge University Press*, 2005.
[48]. G. Colas des Francs, J. Barthes, A. Bouhelier, J. C. Weber, A. Dereux, A. Cuche, C. Girard, Plasmonic Purcell factor and coupling efficiency to surface plasmons. Implications for addressing and controlling optical nanosources, *Journal of Optics*, Vol. 18, Issue 9, 2016, 094005.

5th International Conference on Optics, Photonics and Lasers (OPAL' 2022)

2022 OPAL

Deadlines:

Submission (2-page abstract):	5 March 2022
Notification of acceptance:	20 March 2022
Registration:	5 April 2022
Camera ready (4-6 pages paper):	15 April 2022

One event - three publications !

1) All registered abstracts will be published in the conference proceedings (USB flash drive edition of published Proceedings with the ISBN), distributed during the conference and submitted for indexing to the Web of Science. The previous OPAL' 2018 - 2021 Conference proceedings were indexed by the Conference Proceedings Citation Index.

THOMSON REUTERS CONFERENCE PROCEEDINGS CITATION INDEX INDEXED

2) Authors will be invited to submit full-page extended papers to the special issue of Sensors & Transducers open access journal (ISSN 2306-8515, e-ISSN 1726-5479) for free of charge.

3) The limited number of full-page papers published in the journal will be selected by the Editorial Board to extend for book chapters for the open access Book Series on 'Advances in Optics: Reviews', Vol. 6.

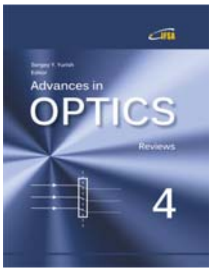

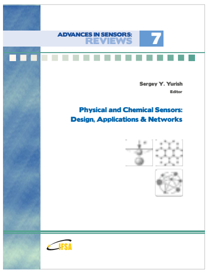

Social Programme

Welcome Cocktail: The Welcome Cocktail will take place on the 16th floor (Sky Lounge Bar) situate on the Hard Rock Hotel's Nirvana Tower building's roof with the best, magnificent, panoramic views to Teide volcano, the Atlantic coast, La Gomera Island and sunset. Actually, it is known as the highest leisure location in Tenerife. Do not miss this opportunity to say the first "hello" to attendees and committee members.

Gala Dinner: The Gala Dinner (BBQ) will take place in the Hard Rock Hotel at the sea beach in front of the Lagoon area.

Contribution Types:

- Keynote presentations
- Invited talks
- Special sessions
- Regular sessions
- Poster session
- Industrial presentations
- Exhibition
- Round tables

Special Sessions:

Participants are welcome to organize and manage special sessions during the conference. Each session will contain 4-6 papers in a related field as specified above.

Session organizers will get:

- Certificate of Appreciation
- Free Registration for the Event
- Special Publishing Theme within Conference Proceedings
- Free article and book chapter post conference publications in appropriate open access journals and 'Advances in Optics: Reviews', Book Series, Vol. 6

Organising Committee

Chairman:
Prof., Dr. Sergey Y. Yurish (IFSA, Spain)

Advisory Chairmen:
Dr. Qiang Wu
(Northumbria University, Newcastle Upon Tyne, UK)
Prof., Dr. Claude Phipps (Photonic Associates, USA)
Prof., Dr. George Semouchkin
(Michigan Technological University, USA)
Prof., Dr. Sandeep Singh Sengar
(University of Copenhagen, Denmark)
Prof., Dr. Boris Mizaikoff (Ulm University, Germany)
Prof., Dr. Mahmoud Daoudi
(National Center for Nuclear Sciences and Technologies, Tunisia)

Conference Manager:
Mrs. Tetyana Zakharchenko
(IFSA Publishing, S.L., Spain)

IFSA Publishing IOP Institute of Physics physicsworld

Call for Chapters

IFSA Publishing

Your Chapter may be in the next Volume of the popular Book Series

ADVANCES IN SENSORS: REVIEWS 8

Open Access Book Series

Sinse 2012

- Physical, chemical and biosensors
- Sensor uncertainty, accuracy, calibration
- Smart sensors and systems
- Intelligent sensors and systems
- Artificial Intelligence enabled sensors
- Virtual and soft sensors
- Sensor instrumentation
- Sensor buses and networks
- Signal processing, sensor fusion
- Nanosensors
- Photonic sensors
- Sensor interfacing and signal conditioning
- Materials for sensors
- MEMS, BioMEMS and NEMS
- Remote Sensors and Telemetry
- Sensor packages and reliability

https://www.sensorsportal.com/HTML/IFSA_Publishing.htm

IFSA

International Frequency Sensor Association Publishing

www.sensorsportal.com

ISSN 1726- 5479

9 771726 547001